

Lehrstuhl für Computerunterstützte Klinische Medizin
der Medizinischen Fakultät Mannheim, Universität Heidelberg
(Direktor: Prof. Dr. rer. nat. Lothar R. Schad)

Tissue quantification based on Magnetic Resonance Fingerprinting

Inauguraldissertation
zur Erlangung des Doctor scientiarum humanarum (Dr. sc. hum.)
der
Medizinischen Fakultät Mannheim
der Ruprecht-Karls-Universität
zu
Heidelberg

vorgelegt von
Benedikt Rieger

aus
Heppenheim

2018

Dean: Prof. Dr. med. Sergij Goerd
Supervisor: Prof. Dr. Lothar R. Schad

Tissue quantification based on Magnetic Resonance Fingerprinting

Quantification of tissue properties including the relaxation parameters has long been a goal of magnetic resonance imaging (MRI), to provide a basis for inter-patient comparability. However, extended acquisition times have hindered the usage of quantification for clinical applications. Magnetic Resonance Fingerprinting (MRF) was introduced as a promising method for simultaneous and fast quantification of multiple tissue parameters. Most MRF methods rely on spiral k-space trajectories, though they are well known to suffer from detrimental effects on the image quality, caused by gradient inaccuracies. The aim of this work was to develop an implementation of the MRF paradigm for quantitative imaging based on Cartesian k-space readout, potentially increasing its usability and robustness. In a first step, a single slice MRF method based on echo-planar imaging (MRF-EPI) was developed, acquiring 160 gradient-spoiled EPI images with Cartesian readout. By varying the flip angle, echo times and including an inversion pulse, fluctuating signal paths were created. T_1 and T_2^* were quantified through matching the fingerprints with a precomputed dictionary. The quantification accuracy was validated in phantom scans showing good agreement of MRF-EPI with reference measurements, with average deviations of $-2 \pm 3\%$ and $2 \pm 3\%$ for T_1 and T_2^* , respectively. *In vivo* maps were of high visual quality and comparable to *in vivo* reference measurements, despite the substantially shortened scan times of 10 s per slice. In a second step, MRF-EPI was modified for improved volumetric coverage by using a slice-interleaved acquisition scheme. In addition to the T_1 and T_2^* maps, proton density (PD) maps could be created without the need of additional measurements. *In vivo* whole-brain coverage of T_1 , T_2^* and PD with 32 slices were acquired within 3:36 minutes, resulting in parameter maps of high visual quality and comparable performance with single-slice MRF-EPI at 4-fold scan-time reduction. In a final step the motion sensitivity of MRF methods was studied. Simulations demonstrated that MRF sequences based on spiral and Cartesian readout exert sensitivity to motion. To correct for motion, the individual measurements of MRF-EPI were corrected by co-registering them with an intensity-based co-registration method. Phantom and *in vivo* measurements demonstrated that motion artefacts were successfully mitigated with intensity-based co-registration, leading to motion-robust artefact-free T_1 and T_2^* maps. Combining the developments of this work resulted in a fast and robust method for multi-parametric whole brain quantification in clinically acceptable scan time.

Gewebequantifizierung mittels Magnetic Resonance Fingerprinting

Die Quantifizierung der Gewebeeigenschaften einschließlich der Relaxationsparameter ist seit langem ein Ziel der MRT und bildet eine Grundlage für die Klassifikation von Krankheitsstadien. Lange Messzeiten haben jedoch den Einsatz der Quantifizierung im klinischen Alltag verhindert. Als vielversprechende Methode zur simultanen und schnellen Quantifizierung mehrerer Gewebeparameter wurde vor einigen Jahren die Idee von Magnetic Resonance Fingerprinting (MRF) publiziert. Die meisten MRF-Methoden beruhen auf spiraler k-Raum Auslese, obwohl sie bekanntermaßen unter nachteiligen Auswirkungen auf die Bildqualität leiden, die durch Gradientenungenauigkeiten verursacht werden. Das Ziel dieser Arbeit war die Entwicklung einer Implementierung des MRF-Paradigmas für quantitative Bildgebung auf der Basis kartesischer k-Raum Auslese, um potenziell klinische Anwendbarkeit und Robustheit zu erhöhen. In einem ersten Schritt wurde ein MRF-Verfahren auf Basis von Echo-Planar Imaging (MRF-EPI) entwickelt, welches 160 EPI-Bilder mit kartesischer Auslese erfasst. Durch Variation des Anregungswinkels, der Echozeiten und eines Inversionspulses wurden die Signale so variiert, dass T_1 und T_2^* durch abgleichen der Signale mit einer Datenbank quantifiziert werden konnten. Die Quantifizierungsgenauigkeit wurde in Phantommessungen validiert, die eine gute Übereinstimmung des MRF-EPI mit Referenzmessungen zeigten (durchschnittliche Abweichungen von $-2 \pm 3\%$ und $2 \pm 3\%$ für T_1 bzw. T_2^*). *In vivo* Parameterkarten waren von hoher visueller Qualität und vergleichbar mit den Referenzmessungen, trotz der deutlich verkürzten Messdauer von 10 s pro Schicht. In einem zweiten Schritt wurde das MRF-EPI für eine verbesserte Abdeckung modifiziert. Zusätzlich zu den T_1 und T_2^* Karten konnten Protonendichtekarten (PD) ohne zusätzliche Messungen erstellt werden. Die Messung von 32 Schichten mit jeweils resultierenden T_1 , T_2^* und PD Parameterkarten wurde innerhalb von 3:36 Minuten erreicht. Die Parameterkarten waren von hoher visueller Qualität. In einem letzten Schritt wurde die Bewegungsempfindlichkeit von MRF-Methoden untersucht. Simulationen zeigten, dass MRF-Sequenzen auf der Basis von spiraler und kartesischer Auslese bewegungsempfindlich sind. Zur Korrektur der Bewegung wurden die individuellen Messungen des MRF-EPI durch Co-Registrierung mit einer intensitätsbasierten Registrierungsmethode korrigiert. Phantom- und *in vivo* Messungen zeigten, dass Bewegungsartefakte durch eine intensitätsbasierte Co-Registrierung erfolgreich korrigiert wurden, was zu bewegungsrobusten artefaktfreien T_1 und T_2^* -Karten führte. Die Sequenzen dieser Arbeit führten zu einer schnellen und robusten Methode zur multiparametrischen Ganzhirnquantifizierung in klinisch akzeptabler Scanzeit.

Contents

1	Introduction and Outline	1
1.1	Introduction	1
1.2	Outline	2
1.3	Citation of previous publications	3
2	Background	5
2.1	MRI Physics	5
2.2	MR Pulse Sequences	13
2.3	Magnetic Resonance Fingerprinting	18
3	“Magnetic Resonance Fingerprinting using Echo-Planar Imaging: Joint Quantification of T_1 and T_2^* Relaxation Times” <i>Magn Reson Med, doi: 10.1002/mrm.26561</i>	25
3.1	Introduction	25
3.2	Methods	26
3.3	Results	31
3.4	Discussion	35
3.5	Conclusion	39
4	“Time efficient whole-brain coverage with MR Fingerprinting us- ing slice-interleaved echo-planar-imaging” <i>Sci. Rep., doi: 10.1038/s41598- 018-24920-z</i>	41
4.1	Introduction	41
4.2	Methods	42
4.3	Results	47
4.4	Discussion	49
4.5	Conclusion	55
4.6	Supplementary Information	55
5	“Improved motion robustness for EPI-based MR Fingerprinting using intensity based image registration” <i>Sci. Rep., submitted</i>	59
5.1	Introduction	59
5.2	Methods	60
5.3	Results	63
5.4	Discussion	66
5.5	Conclusion	68
6	Summary	69

7 Outlook	73
Bibliography	77
Curriculum Vitae	89
Acknowledgements	91

1.1 Introduction

Following the introduction of Magnetic Resonance Imaging (MRI), which was paved by the noble laureate winning work of Lauterbur and Mansfield in 1973, MRI has been gaining significance in the clinical imaging practice, growing to be one of the major imaging modalities. As MRI provides *in vivo* medical images without the need for ionizing radiation in contrast to e.g. computer tomography or positron emission tomography. It is used for a wide range of clinical applications, including neurological diseases, stroke and cancer. However, clinical MRI traditionally uses qualitative or 'weighted' measurements and the quantification of underlying physical parameters is rarely performed. As such, the same subject measured with a qualitative sequence with various coils or on different MRI scanners can lead to intensity variations, depending on the scanner setup, which limits the comparability between different scans.

Quantification of tissue properties including the relaxation parameters such as T_1 , T_2 , and T_2^* has been a long standing goal in MRI research, to facilitate improved tissue characterization and providing a basis for inter-patient comparability. Further, quantitative measurements have the potential for the detection of diseases and staging in multiple clinical scenarios, such as differentiating cirrhotic from noncirrhotic liver (Kim et al., 2012), providing surrogate markers of function in native and transplanted kidneys (Huang et al., 2011) or investigating the iron content in the brain of patients suffering from Huntington's, Parkinson's and Alzheimer's disease (Ordidge et al., 1994; Vymazal et al., 1999). Several measurement methods have been proposed to quantify a variety of physical parameters e.g. the Look-Locker sequence for T_1 mapping which acquires data at multiple time points along the signal recovery curve after either an inversion or a saturation pulse. Equally for T_2 and T_2^* , the gold standard sequences are the Carr-Purcell-Meiboom-Gill spin echo sequence for T_2 (Carr and Purcell, 1954) and a gradient echo method for T_2^* , sampling the T_2 and T_2^* decay curve at different echo times (TE). Due to measurement times that are beyond what is clinically acceptable, several accelerated acquisition techniques have been proposed, such as variable flip angle methods for fast T_1 quantification (Cheng and Wright, 2006; Zhu and Penn, 2005) and fast low angle shot based methods for T_2 quantification (Deichmann et al., 1995). However, the accuracy and precision of the estimated parameters of these accelerated sequences are prone to signal variations caused by motion and undersampling artefacts (Jiang et al., 2015). Other approaches

for decreasing measurement time include simultaneous quantification of multiple parameters (Wartjes et al., 2007a), though long scan times and high sensitivity to the measurement set-up limit their practical implementation (Ma et al., 2013). While the quantification of tissue characteristics parameters has achieved clinical impact in a few select fields of MRI, such as myocardial T_1 mapping, the clear majority of MRI measurements are based on qualitative imaging, particularly in clinical MRI.

Recently, a novel imaging technique termed Magnetic Resonance Fingerprinting (MRF) has enforced the interest in parameter mapping due to its potential for fast quantification of multiple physical parameters (Ma et al., 2013). Unlike typical quantification sequences which sample the exponential decay at multiple time points, the general concept of MRF is to excite the magnetization in a pseudo-random fashion, thereby generating unique signal paths, called 'fingerprints', based on their underlying MRI properties. The fingerprints are generated by the rapid acquisition of numerous highly undersampled images. Signal variations are induced by varying the sequence parameters such as flip angle, TE, repetition time (TR) and including an inversion pulse in the sequence. Matching these fingerprints to a precomputed dictionary allows the acquisition of parameter maps for a variety of physical parameters. The original MRF method was based on a balanced steady state free precession sequence design, allowing for joint T_1 and T_2 mapping. Subsequently, an unbalanced fast imaging with steady state precession (FISP) sequence was introduced to overcome sensitivity to inhomogeneities of the main magnetic field at the expense of measurement SNR and has been used as a template for a number of MRF sequences (Assländer et al., 2017; Buonincontri and Sawiak, 2015; Jiang et al., 2017b, 2015). However, most previously proposed methods base their readout on highly undersampled spiral k-space trajectory, to facilitate rapid image readout as required in an MRF sequence. Recently, initial data indicated a high sensitivity of MRF sequences to gradient deviations, due to the inherent properties of the non-Cartesian image readout (Hong et al., 2016). Especially spiral trajectories, as used in most MRF sequences, are well known to suffer from detrimental effects on the image quality, caused by gradient inaccuracies. This greatly limits its availability at present and still prevents the wide-spread use of spiral imaging in clinical protocols.

The aim of work is to develop a novel MRF method based on Cartesian readout for T_1 and T_2^* quantification for clinical practice, facilitating improved robustness and increased usability within clinically acceptable scan times.

1.2 Outline

This work is written cumulatively. Chapters 3 to 5 present self-contained scientific studies with an introduction to the topic, description of the methods and the presentation of the results and a discussion.

Chapter 2 aims to provide a brief overview of the physical background as a basis for understanding the presented methods. This further includes corresponding technical developments and relevant imaging techniques in the field of quantitative imaging and provides an introduction to MRF.

In chapter 3, a novel MRF method for quantitative imaging is introduced using echo-planar imaging (EPI) for simultaneous assessment of T_1 and T_2^* relaxation

times. The proposed MRF method (MRF-EPI) combines an inversion recovery pulse with varying flip-angles, TEs and TRs and accelerated EPI readouts to generate unique signal traces. Matching these traces to a precomputed dictionary with integrated B_1^+ correction enable T_1 and T_2^* quantification.

Chapter 4 presents a slice-interleaved extension of the MRF method proposed in chapter 3 to improve volumetric coverage while reducing scan time. The original sequence is modified to acquire several slices in a randomized interleaved manner. The number of interleaved slices is optimized in numerical simulations and validated in phantom measurements and feasibility is demonstrated *in vivo*.

In chapter 5 the motion sensitivity of MRF methods based on spiral and Cartesian k-space trajectories are studied in simulations with regard to the severity of translational and rotational motion. The results are validated in phantom and *in vivo* scans with the MRF method presented in chapter 3. Furthermore, a correction scheme is developed for the MRF-EPI to mitigate motion artefacts, increasing its clinical usability of the sequence. The quality of the correction scheme and the resulting T_1 and T_2^* maps are qualitatively compared to the results of motion free reference scans.

Chapter 6 provides an overview of the relevant results from the scientific studies presented in chapters 3 through 5.

Chapter 7 contains an outlook on future research perspectives and clinical relevance of the methods that are proposed in this thesis.

1.3 Citation of previous publications

Most of the thesis has been published elsewhere or is currently submitted for publication. The following chapters have been published:

Chapter 3: Rieger, B., Zimmer, F., Zapp, J., Weingärtner, S. and Schad, L. R. (2017). Magnetic resonance fingerprinting using echo-planar imaging: Joint quantification of T_1 and T_2^* relaxation times. *Magn Reson Med* 78, 1724–1733

Chapter 4: Rieger, B., Akçakaya, M., Pariente, J. C., Llufriu, S., Martinez-Heras, E., Weingärtner, S. and Schad, L. R. (2018). Time efficient whole-brain coverage with MR Fingerprinting using slice-interleaved echo-planar-imaging. *Sci. Rep.* 8, 6667.

Chapter 5: Rieger, B., Wenning, M., Weingärtner, S. and Schad, L. R. (2018). Improved motion robustness for EPI-based MR Fingerprinting using intensity based image registration. *Sci. Rep. submitted, Date of submission: 01.06.2018*

Background **2**

This chapter provides an introduction and overview of the principles of nuclear magnetic resonance (NMR), the fundamentals of magnetic resonance imaging (MRI) and magnetic resonance fingerprinting (MRF) techniques.

2.1 MRI Physics

Nuclear magnetic resonance was independently investigated and published by Felix Bloch (Bloch, 1946) and Edward Mills Purcell (Purcell et al., 1946) in 1946, describing the specific magnetic resonance property of nuclei in a magnetic field, for which they were honoured with the Nobel Prize in Physics in 1952. MRI was developed in 1973 by Lauterbur (Lauterbur, 1973) and Mansfield (Mansfield and Grannell, 1975), when they proposed to spatially encode the NMR signal with magnetic field gradients and developed the methods for fast conversion of the NMR signals into imaging data, for which they shared the Nobel Prize in Physiology or Medicine in 2003.

This chapter aims to provide a short overview of the principles of NMR and the basics of MRI. A more comprehensive description of the topic can be found in (Haacke, 1999; Levitt, 2008).

2.1.1 Microscopic and Macroscopic Magnetization

The single nucleons composing an atomic nucleus have an intrinsic spin and combine to a spin quantum number S . If the number of protons and neutrons are both even, there is no overall spin, therefore $S = 0$. However, otherwise the angular momentum \vec{S} of the spin is associated with a magnetic moment $\vec{\mu}$ through the gyromagnetic ratio γ

$$\vec{\mu} = \gamma \vec{S}. \quad (2.1)$$

When placing a nucleus with a magnetic moment $\vec{\mu}$ in an external static magnetic field \vec{B} , it will be subject to a torque $\vec{\tau}$ causing a change in the expectation value of the magnetic moment

$$\vec{\tau} = \vec{\mu} \times \vec{B} = \frac{1}{\gamma} \frac{d\vec{\mu}}{dt} \quad (2.2)$$

resulting in

$$\frac{d\vec{\mu}}{dt} = \gamma \vec{\mu} \times \vec{B} \quad (2.3)$$

Assuming a constant external magnetic field $\vec{B} = (0, 0, B_0)^T$ along the z-axis, quantum mechanics states that the magnetic field splits the energy ground states into $(2S + 1)$ energy levels E_m given by

$$E_m = -\gamma\hbar m B_0 \quad (2.4)$$

proportional to the magnetic quantum number m and the reduced Planck constant \hbar . When dealing with nuclei which have a spin of $S = 1/2$, such as ^1H , two energy levels are valid, $E_{+1/2}$ with $m = +1/2$ and $E_{-1/2}$ with $m = -1/2$. For nuclei in an external magnetic field in z-direction, whose magnetic moment align either parallel or anti-parallel to the magnetic field, the energy difference between the two energy states equals to

$$\Delta E = E_{-1/2} - E_{+1/2} = \gamma\hbar B_0 = \hbar\omega_0 \quad (2.5)$$

Transitions between the two energy levels may be induced by photons carrying the energy ΔE . The difference in energy between the two states is proportional to the Larmor frequency

$$\omega_0 = \gamma B_0. \quad (2.6)$$

In the state of thermal equilibrium, the distribution ratio of the nuclei in the different energy states is given by the Boltzmann distribution

$$\frac{N_{upper}}{N_{lower}} = e^{-\Delta E/kT} \quad (2.7)$$

with k being the Boltzmann constant, T the absolute temperature in Kelvin and N_{upper} and N_{lower} corresponding to the population of nuclei in the higher and lower energy states. For protons in a 3T magnetic field at room temperature, the ratio will be about 0.999998, meaning that only very few excess nuclei are in the lower energy state than in the upper state. Most physical samples consist of many atoms, in one cubic millimeter there are in the order of $\approx 10^{20}$ nuclei. Therefore, the notion of macroscopic magnetization \vec{M} is introduced as the sum of all individual moments $\vec{\mu}_i$ per Volume V within the external magnetic field along the z-axis

$$\vec{M} = \frac{1}{V} \sum_i \vec{\mu}_i. \quad (2.8)$$

For protons at body temperature ($T \approx 310\text{K}$), the net magnetization based on the Boltzmann statistics is given by

$$M_0 \approx \frac{N}{V} \frac{\gamma^2 \hbar^2 S(S+1) B_0}{3kT} \quad (2.9)$$

N being the number of individual magnetic moments in the volume V . The NMR signal is therefore proportional to the magnetic field B_0 and the spin density N/V . As hydrogen has a high gyromagnetic ratio compared to other stable nuclei and as the human body has abundant water, NMR based on protons is especially well suited.

2.1.2 Radiofrequency Excitation

The behavior of a macroscopic magnetization (Eq. 2.8), which is the sum of the nuclei in a static external magnetic field (Eq. 2.3) and assuming that the spins are not interacting with their environment, can be described by

$$\frac{d}{dt}\vec{M}(t) = \gamma\vec{M}(t) \times \vec{B}_0 \quad (2.10)$$

expressing the precession of the magnetization about the magnetic field with the Larmor frequency $\omega_0 = \gamma B_0$. If an external circularly polarized radio frequency (RF) field $\vec{B}_1(t)$ with the amplitude B_1 and the frequency ω_1 is applied perpendicular to the B_0 field, which is aligned with the z-axis, a transverse magnetization can be created

$$\vec{B}_1(t) = B_1 \begin{pmatrix} \cos(\omega_1 t) \\ \sin(\omega_1 t) \\ 0 \end{pmatrix}. \quad (2.11)$$

Assuming a frame of reference rotating around the z-axis with the frequency ω_1 and combining the magnetic fields \vec{B}_0 and \vec{B}_1 to an effective magnetic field \vec{B}_{eff} , the motion of the macroscopic magnetization can be described by equation

$$\frac{d}{dt}\vec{M}'(t) = \gamma\vec{M}'(t) \times \begin{pmatrix} B_1 \\ 0 \\ B_0 - \frac{\omega_1}{\gamma} \end{pmatrix} = \gamma\vec{M}'(t) \times \vec{B}_{eff}. \quad (2.12)$$

If the frequency of the excitation pulse is chosen such, that it corresponds to the frequency of the main magnetic field $\omega_1 = \gamma B_0$, the resulting effective field $\vec{B}_{eff} = (B_1, 0, 0)$ causes a rotation of the macroscopic magnetization away from the z-direction. Applying the magnetic field B_1 only for a duration of τ causes the rotation of the magnetization by a flip angle of α

$$\alpha = \gamma \int_0^\tau B_1(t) dt \quad (2.13)$$

Applying the B_1 for a short moment of time is referred to as RF pulse, as the frequency is in the same order of magnitude as commonly used radio signals. The magnetic field of the precessing magnetization in the xy plane (transversal plane), caused by the RF pulse, can be measured with a coil, in which a voltage $V(t) = V_0(\omega_0 t)$ is induced. The amplitude V_0 of the voltage is dependent on the dimensions of the coil and the properties of the electric circuit.

2.1.3 Relaxation and Bloch Equations

In the year 1946, Felix Bloch proposed the Bloch equations, which describe the interaction of the magnetization with the surrounding spins and environment within the external magnetic field (Bloch, 1946). After applying an excitation field \vec{B}_1 , the magnetization converges back to the equilibrium state. This process is called relaxation. In the case of a constant magnetic field, the Bloch equations are given as

$$\frac{d}{dt}M_x = \gamma(\vec{M}(t) \times \vec{B}(t))_x - \frac{M_x(t)}{T_2} \quad (2.14)$$

$$\frac{d}{dt}M_y = \gamma(\vec{M}(t) \times \vec{B}(t))_y - \frac{M_y(t)}{T_2} \quad (2.15)$$

$$\frac{d}{dt}M_z = \gamma(\vec{M}(t) \times \vec{B}(t))_z - \frac{M_z(t) - M_0}{T_1} \quad (2.16)$$

where T_1 denotes the longitudinal and T_2 the transversal relaxation time.

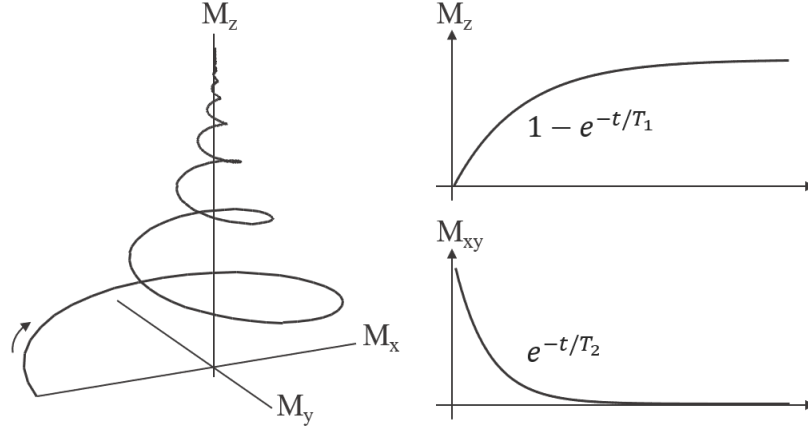


Figure 2.1: Relaxation after excitation with a 90° pulse. The images depict the temporal evolution of the magnetization vector with its longitudinal T_1 relaxation and the transversal T_2 relaxation. The magnetization vector precesses around the static magnetic field \vec{B}_0 with the frequency ω

T_1 Relaxation

Equation 2.16 describes the spin-lattice relaxation mechanism, often referred to as longitudinal or T_1 relaxation. This mechanism describes the rate by which the component of the magnetization vector parallel to the main magnetic field B_0 reaches the thermodynamic equilibrium. The rate of regrowth is characterized by the time constant T_1 , which arises from the interaction between the spins and their atomic neighborhood, the lattice. The nuclei can transfer the energy they obtained from the RF pulse to the surrounding lattice. The solution of the differential Equation 2.16 for an initial equilibrium magnetization $M_{z,0}$ can be expressed as

$$M_z(t) = M_{z,0} - (M_{z,0} - M_z(0))e^{-t/T_1} \quad (2.17)$$

Figure 2.1 shows the T_1 and T_2 relaxation after a 90° pulse, flipping the magnetization into the transversal xy plane and then relaxing to the equilibrium state.

T_2 Relaxation

The decay of the transversal component, perpendicular to the main magnetic field, is described by Equation 2.14 and 2.15. This mechanism is referred to as spin-spin or T_2 relaxation. This relaxation type, which is often a lot faster than the T_1 relaxation ($T_2 \leq T_1$), is caused by the interaction with local magnetic field inhomogeneities on the micro- and nanoscales, dispersing the phases due

to varying precessional frequencies. This dephasing results in a decay of the macroscopic magnetization in the transversal plane. The explicit solution of the differential Equations 2.14 and 2.15 with the initial value $M_{x,y}(0)$ is

$$M_{x,y}(t) = M_{x,y}(0)e^{-t/T_2}. \quad (2.18)$$

T_2^* Relaxation

All nuclei would precess with the same frequency in an idealized system. However, due to additional static inhomogeneities in the main magnetic field B_0 e.g. due to minor differences in the chemical environment, the MR signal decays faster than the T_2 -Relaxation. The locally varying field ΔB_0 leads to a dispersion of the magnetic spin vectors, inducing a phase and with that the T_2' relaxation. As the locally varying field ΔB_0 is static, it is not a true relaxation process, only a phase shift between the spin vectors is induced and the signal can be recovered. The complete dephasing of the transversal magnetization is described by the T_2^* relaxation

$$\frac{1}{T_2^*} = \frac{1}{T_2} + \frac{1}{T_2'}. \quad (2.19)$$

2.1.4 Spatial Encoding

Spatial encoding relies on successively applying magnetic field gradients to achieve spatially resolved signal maps. This spatial encoding is accomplished by overlaying the main magnetic field $\vec{B}_0 = (0, 0, B_0)^T$ with a linear magnetic field gradient \vec{G}

$$\vec{G}(t) = \begin{pmatrix} G_x(t) \\ G_y(t) \\ G_z(t) \end{pmatrix} \quad (2.20)$$

which results in a modified magnetic field

$$\vec{B}(\vec{r}, t) = \vec{B}_0 + \vec{B}'(\vec{r}, t) = \vec{B}_0 + \begin{pmatrix} 0 \\ 0 \\ \vec{G}(t)\vec{r} \end{pmatrix} \quad (2.21)$$

As a result, the Larmor frequency becomes spatially dependent by the superposition of both magnetic fields

$$\omega(\vec{r}, t) = \gamma(B_0 + \vec{G}(t)\vec{r}) = \omega_0 + \omega_G(\vec{r}, t) \quad (2.22)$$

An additional phase ϕ is accumulated during the application of the gradients for a given time t at the position \vec{r}

$$\phi(\vec{r}, t) = - \int_0^t \omega_G(\vec{r}, t') dt' = -\gamma\vec{r} \int_0^t \vec{G}(t') dt' = -\vec{k}(t)\vec{r} \quad (2.23)$$

The spatial wave vector \vec{k} is located in k-space and is given by

$$\vec{k}(t) = \gamma \int_0^t \vec{G}(t') dt' \quad (2.24)$$

The signal S that is detected by the coil is proportional to a magnetic field $B_{receive,xy}$ from the transversal magnetization and is related to its transversal component with its initial phase angle Φ_B and the additional phase $\phi(\vec{r})$ from the gradients

$$S(\vec{k}(t), t) \propto \omega_0 \int e^{-t/T_2(\vec{r})} M_{xy}(\vec{r}, 0) B_{receive,xy}(\vec{r}) e^{-i(\omega_0 t + \vec{k}(t)\vec{r} + \Phi_B(\vec{r}) + \phi(\vec{r}))} d\vec{r} \quad (2.25)$$

Without the effects of the transversal magnetization decay and assuming a homogeneous $B_{receive}$ field, the overall signal contribution $S(\vec{k}, t)$ of a sample can be described by

$$S(\vec{k}(t), t) \propto \int M_{xy}(\vec{r}) e^{-i(\vec{k}(t)\vec{r})} d\vec{r} \quad (2.26)$$

The overall signal is therefore proportional to the Fourier transform of M_{xy} of the spatial distribution of the transversal magnetization. In order to obtain spatially resolved images in the transversal plane, the signal needs to be acquired for multiple k-space values, which is performed by varying the gradients \vec{G} . A spatially distributed image can be calculated by an inverse Fourier transform

$$M_{xy}(\vec{r}) \propto \int S(\vec{k}(t), t) e^{i\vec{k}(t)\vec{r}} d\vec{r} \quad (2.27)$$

For the generation of a 2D image, three encoding techniques are needed called slice selection, phase encoding and frequency encoding.

Slice Encoding

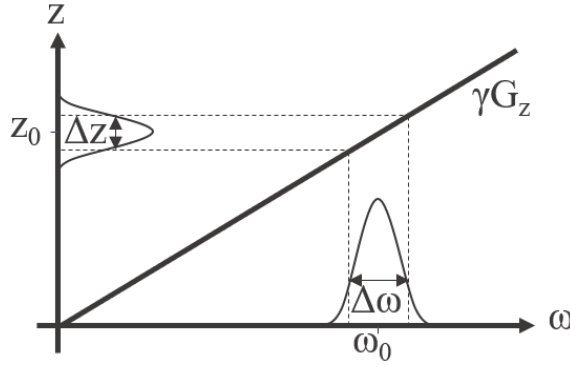


Figure 2.2: Principle of slice selection: By applying a gradient G_z , each location along the z -axis has a defined resonance frequency. If an excitation pulse is applied with the bandwidth $\Delta\omega$ around the central frequency ω_0 , a slice with the specific position Δz is excited

To acquire an image, a single thin slice is excited by combining gradient fields and spatially selective RF pulses. Without the application of a field gradient, the RF pulse would excite the complete imaging volume, prohibiting the acquisition of a 2D slice. Therefore, a slice selection gradient is applied perpendicular to the slice while transmitting the RF pulse. The slice selection gradient causes the resonance frequency to be a linear function corresponding to the selected

axis (compare Figure 2.2). For a slice excitation in the transversal xy plane, a gradient is applied along the z-axis, modifying the local resonance frequency by $\omega(z) = \gamma(B_0 + G_z z)$. The slice thickness Δz is a function of the bandwidth Δf of the RF pulse and the applied gradient

$$\Delta z = \frac{\Delta f}{\gamma G_z} \quad (2.28)$$

The base frequency ω_0 determines the location of the slice within the imaging volume in z-direction. To obtain a uniform flip angle across the slice, the frequency profile must be proportional to the boxcar function $\text{rect}(f/\Delta f)$ with the bandwidth Δf . As the inverse Fourier transform of the frequency profile is a sinc function, the RF pulse $B_1(t)$ in the time domain is given by

$$B_1(t) \propto \text{sinc}(\pi \Delta f t) \quad (2.29)$$

Phase and Frequency Encoding

After the excitation of a specific slice, both directions of the 2D image need to be encoded, called the phase and frequency encoding. In the case of a slice selection in the transversal xy plane, a gradient is applied along the y-axis, such that the magnetization acquires an additional phase depending on its location. The phase of the magnetization is dependent on the location, the amplitude and the time of the applied phase encoding gradient. Figure 2.3 illustrates the principle of phase-encoding

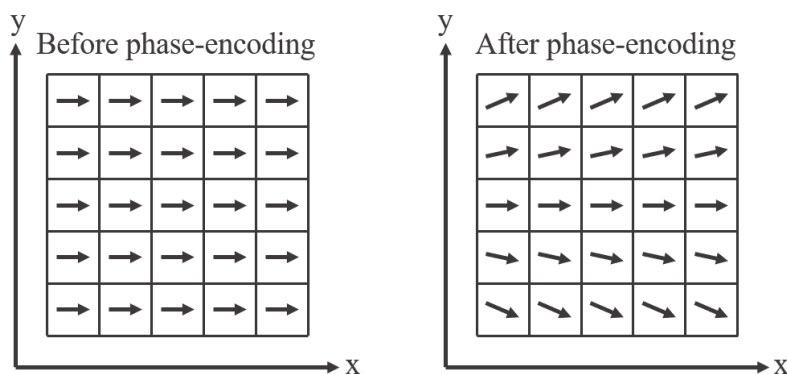


Figure 2.3: Following RF excitation, the phase encoding gradient G_y is applied along the y-axis, introducing a phase depending on the location of the magnetization in y-direction. Adapted from (Glover, 2005)

The third linear gradient is called frequency or readout encoding and is applied along the x-axis during the time the signal is acquired. The frequency encoding linearly modifies the frequency along the x-direction, assigning each point along the x-axis a unique frequency. The signal acquired during one frequency encoding step is commonly referred to as a k-space line, due to the nature of filling the k-space, therefore gaining the name readout encoding.

2.1.5 k-Space Characteristics and Image Resolution

It is not possible to cover the whole k-space in a continuous manner due to technical and temporal limitations; therefore, it needs to be sampled in a discrete manner. To sample a k-space line using a constant gradient G in the time interval Δt , the distance of the k-space points is given by

$$\Delta k = \gamma G \Delta t. \quad (2.30)$$

Discrete sampling $u(\vec{k})$ of the k-space can be described by an infinite set of equally spaced Dirac delta functions δ . Therefore, the sampled signal $S_{sampled}(\vec{k})$ is a multiplication of the continuous signal $S(k)$ with the sampling function

$$S_{sampled}(\vec{k}) = S(k) \cdot u(\vec{k}) = S(\vec{k}) \Delta k \sum_{n=-\infty}^{+\infty} \delta(k - n\Delta k). \quad (2.31)$$

Combining the Equation 2.26 with the convolution theorem, which states that the Fourier transform of a pointwise product is the convolution of the inverse Fourier transform, the reconstructed image $M_{sample}(r)$ can be expressed by:

$$M_{sampled}(\vec{r}) = \mathcal{F}^{-1}[S_{sampled}(\vec{k})] = M(\vec{r}) \otimes \mathcal{F}^{-1}[u(\vec{k})] \quad (2.32)$$

The inverse Fourier transform of the Dirac comb function with a period of Δk is once again a Dirac comb function, using the Fourier series identity results in

$$M_{sampled}(\vec{r}) = M_{xy}(\vec{r}) \otimes \sum_{n=-\infty}^{+\infty} \delta(x - \frac{n}{\Delta k}). \quad (2.33)$$

As the Dirac comb function has a periodicity of $1/\Delta k$, the images are periodically repeated and equally spaced at the positions $1/\Delta k$. As the images should not overlap, as this would cause artefacts called aliasing (compare Figure 2.4), the field of view (FOV) = $1/\Delta k$ has to be chosen larger than the object size L , therefore the Nyquist criterion has to be fulfilled:

$$\Delta k = \frac{1}{FOV} \leq \frac{1}{L} \quad (2.34)$$

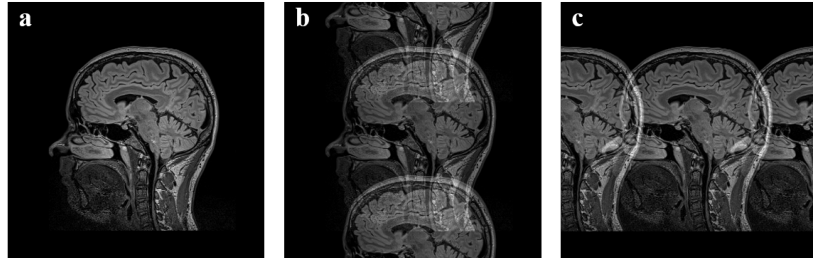


Figure 2.4: *If the sampling rate is chosen too low, such that the Nyquist criterion has not been fulfilled, the images overlap, causing aliasing. a) Fully sampled image fulfilling the Nyquist criterion, b) k-space was subsampled by factor of two in phase encoding and c) frequency encoding direction*

2.2 MR Pulse Sequences

In MRI, a pulse sequence consists of a specific series of events comprising of RF excitations, gradient waveforms and data acquisitions, manipulating the magnetization to retrieve the desired signal and with that image contrast weighting. While pulse sequences consist only of few basic building blocks, they can be combined to many different pulse sequences, each with their own advantages and disadvantages, suitable for the desired medical or research purpose. Here, the most relevant pulse sequences for the following chapters of this work are presented.

2.2.1 Spin Echo

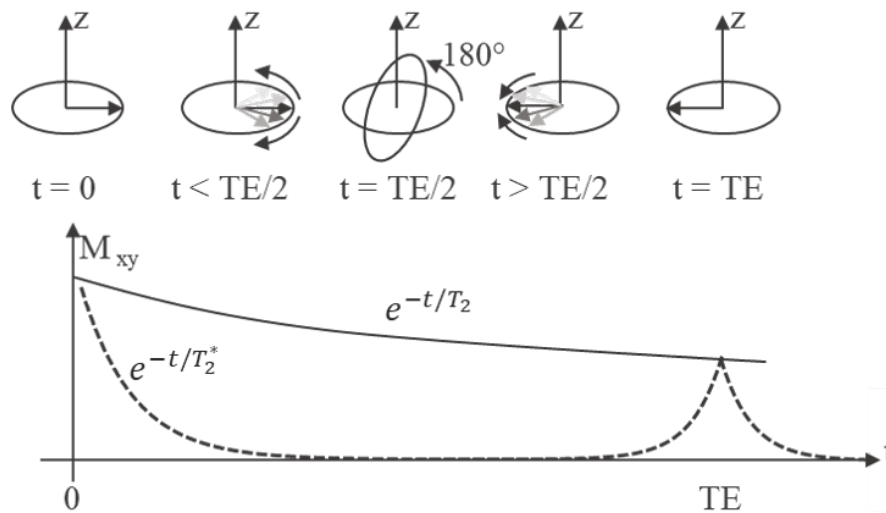


Figure 2.5: Principle of creating a spin echo (upper plot) and corresponding time course (lower plot): At $t = 0$, a 90° pulse is applied along the x-axis, rotating the longitudinal magnetization into the transversal plane. Due to T_2^* relaxation, the spins start to dephase. At the time $t = TE/2$ a 180° pulse is applied, rotating the magnetization around the x-axis. The dephasing process is now inverted, therefore the spins rephase, creating an echo at the time $t = TE$. The signal strength is limited by the T_2 envelope. Therefore the signal acquired at $t = TE$ is T_2 weighted.

Figure 2.5 illustrates the principle of a spin echo (SE). After flipping the longitudinal magnetization into the transversal xy plane with a 90° pulse, the magnetization starts to dephase due to the microscopic field inhomogeneities causing the T_2^* relaxation. Applying a 180° refocusing pulse at the time $t = TE/2$, the magnetization is flipped around the x-axis, causing the magnetization to rephase as the precession is inverted. The refocused transversal magnetization is however still subject to the T_2 relaxation.

The sequence diagram of a 2D SE acquisition is shown in Figure 2.6. First, a slice is excited by applying the slice selective gradient G_z and a 90° excitation pulse. Following the excitation, the moment of the slice selective gradient is compensated and the phase and frequency encoding gradients are applied. At the time $t = TE/2$, a 180° refocusing pulse in combination with the slice selection

gradient flips the magnetization within the selected slice. The crusher gradients surrounding the slice selective gradient minimize image artefacts arising from the refocusing pulse. During readout, the frequency encoding gradient is applied, sampling one k-space line. This sequence is repeated for each k-space line until the desired k-space coverage is reached.

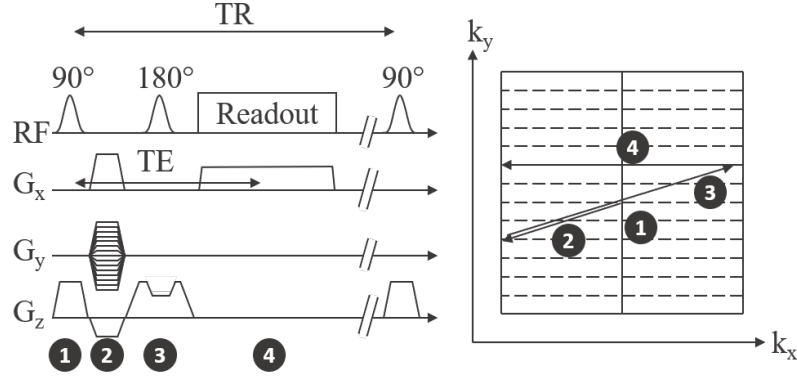


Figure 2.6: Sequence diagram (left) and k-space trajectory (right). Following a 90° RF pulse (1), the spins are dephased due to T_2^* relaxation. Next, the moment of the slice selection gradient during the excitation is compensated (z-direction), simultaneously the phase and frequency encoding gradients are applied (2). At $t = TE/2$, a 180° refocusing pulse is applied, inverting the magnetization, in k-space corresponding to point reflection with respect to the k-space centre (3). During the time of the readout, a constant frequency encoding is used, such that the signal rephases at TE in the k_x -space centre, creating an echo (4)

2.2.2 Inversion Recovery

Inversion recovery (IR) is used to either create T_1 weighted images or to quantify the underlying relaxation time T_1 . From an equilibrium state, a 180° pulse inverts the longitudinal magnetization, such that no transversal magnetization is created, though the longitudinal magnetization shows in opposite z-direction along the main magnetic field. After waiting for $t = TI$ (inversion time), the longitudinal magnetization is rotated into the transversal plane with a 90° pulse and acquired with an imaging sequence. Here, a number of imaging sequences can be used to acquire the T_1 weighted images, e.g. an inversion recovery spin echo (IR-SE). This sequence inverts the magnetization with a 180° pulse, waits the time TI and then uses the spin echo sequence described in section 2.2.1 to acquire each k-space line, resulting in T_1 weighted images. The T_1 contrast weighting of an image is heavily dependent on the relaxation time T_1 and TI, given by

$$M_z(TI) = M_0 \left(1 - 2e^{-TI/T_1} \right) \quad (2.35)$$

Figure 2.7 shows the recovery of the longitudinal magnetization of two exemplary T_1 -times.

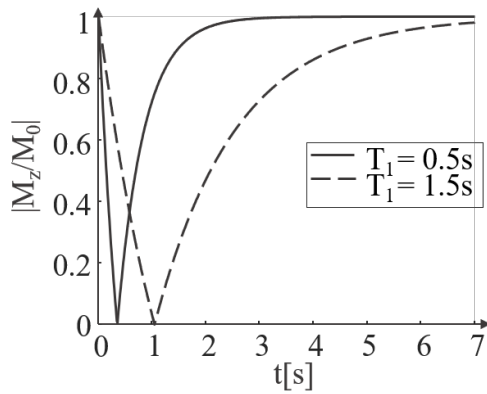


Figure 2.7: The magnitude signal of the longitudinal magnetization during an inversion recovery sequence with two different T_1 times.

2.2.3 Gradient Echo

Gradient echo (GRE) pulse sequences are commonly used due to their short acquisition times. Unlike the spin echo sequences, which use a 180° RF refocusing pulse to generate the echo, GRE sequences only change the polarity of their gradient on the frequency encoding axis to generate the same effect. As depicted in Figure 2.8, following an excitation pulse, the readout gradient dephases the spins, which are then rephased by changing the polarity of the gradient. Typically, the moment of the dephasing is chosen such that it is half as large as the readout moment, as in that case the echo is formed in the middle of the data acquisition.

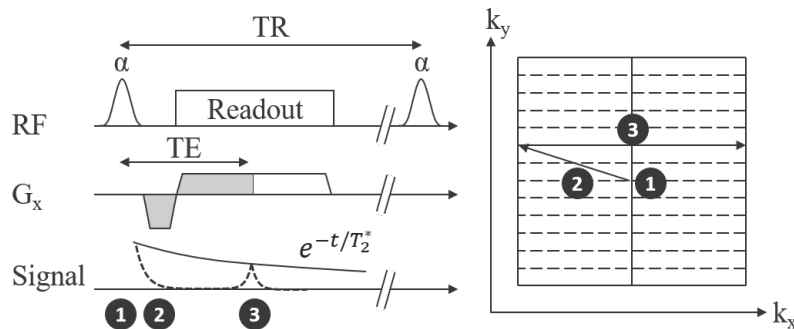


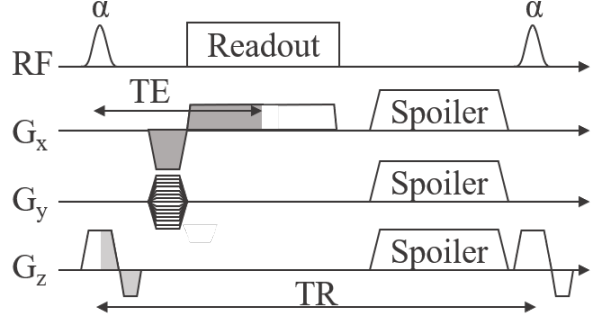
Figure 2.8: Sequence diagram (left) and k -space trajectory (right). Following an RF pulse with the flip angle α (1), the spins are dephased caused through the negative gradient prior to readout (2). During the time of the readout, a constant frequency encoding is used, such that the signal rephases at TE in the k_x -space center (3)

As the GRE acquisition doesn't use any refocusing pulses, the magnetization is never inverted, leading to undisturbed T_1 recovery. Further, as the excitation pulse typically uses small flip angles, the longitudinal magnetization is hardly affected, offering the possibility of using short TR times. As the GRE cannot compensate for magnetic field inhomogeneities, the signal is T_2^* weighted during the acquisition.

2.2.4 Fast Low-Angle Shot

Fast Low-Angle Shot (FLASH) is a GRE sequence with low flip-angles, spoiling the transverse magnetization after each acquisition. Spoiling refers to the disruption of the transverse phase coherence, eliminating the transverse magnetization

Figure 2.9: Pulse sequence diagram of the spoiled FLASH sequence. After a typical GRE readout, spoilers are applied on all three-gradient axes, causing the transversal magnetization to dephase, such that only longitudinal magnetization is left over prior to the next RF excitation.



M_{xy} while keeping the longitudinal magnetization M_z . Spoiling can be achieved in multiple ways, including choosing $TR \geq 4 \cdot T_2$, therefore waiting for the transverse magnetization to naturally decay to nearly zero, due to T_2 relaxation. As this method prohibits short acquisition times due to the need for long TRs, FLASH sequences use gradient spoiling, dephasing the transversal magnetization after the readout of each gradient echo. The gradients used to dephase the transversal magnetization are called spoilers.

Figure 2.9 shows the sequence diagram of the FLASH sequence for the acquisition of one k-space line. The RF pulse converts some of the longitudinal magnetization into transversal magnetization, which is de- and rephased through the frequency encoding gradient and after readout, the transversal magnetization is spoiled. Repeating the acquisition scheme in short succession, the longitudinal magnetization reaches a steady state. Here, the reduction of the longitudinal magnetization due to the RF pulse equals the T_1 recovery during TR. Given the flip angle α , the repetition time TR and the echo time TE , the magnetization signal in steady state M_{SS} can be described by

$$S_{FLASH} \propto M_{SS} = M_0 \frac{\sin(\alpha)(1 - e^{-TR/T_1})}{(1 - \cos(\alpha)e^{-TR/T_1})} e^{-TE/T_2^*} \quad (2.36)$$

The signal S_{FLASH} can be maximized by choosing the Ernst angle, setting the first derivative to zero:

$$\alpha_E = \arccos(e^{-TR/T_1}) \quad (2.37)$$

2.2.5 Balanced Steady State Free Precession

The balanced steady state free precession (bSSFP) technique, also called True-FISP or FIESTA, is a GRE measurement sequence keeping both the transversal and longitudinal magnetization in steady state. In contrast, the FLASH sequence only drives the longitudinal magnetization into steady state, spoiling the transversal component prior to each excitation.

The sequence diagram is shown in Figure 2.10 left. The RF excitation rotates part of the longitudinal magnetization into the transversal plane. Following the dephasing of the transversal magnetization through the frequency encoding gradient, the magnetization is rephased through the positive gradient lobe. The magnetization will rephase at TE. After readout, the magnetization will be out of phase, which is compensated once again by the gradients through switching their polarity. Therefore, all gradient fields are compensated prior to the application

of the next RF pulse. Each consecutive RF pulse is applied with the opposite polarity, flipping the transversal magnetization within the transversal plane, acting as a kind of refocusing pulse.

As the transversal magnetization is not spoiled but refocused before the application of another RF pulse, the bSSFP exhibits a relative complicated contrast including contributions of T_1 and T_2 . The resulting steady state signal function is further determined by the repetition time TR and flip angle α

$$M_{SS} = M_0 \frac{\sqrt{e^{-TR/T_2}(1 - e^{-TR/T_1})\sin(\alpha)}}{1 - (e^{-TR/T_1} - e^{-TR/T_2})\cos(\alpha) - e^{-TR/T_2}e^{-TR/T_1}}. \quad (2.38)$$

As the transversal magnetization is not spoiled, the signal of the bSSFP is generally stronger than that of the FLASH. However, bSSFP is sensitive to off-resonance effects, potentially causing banding artefacts in the images.

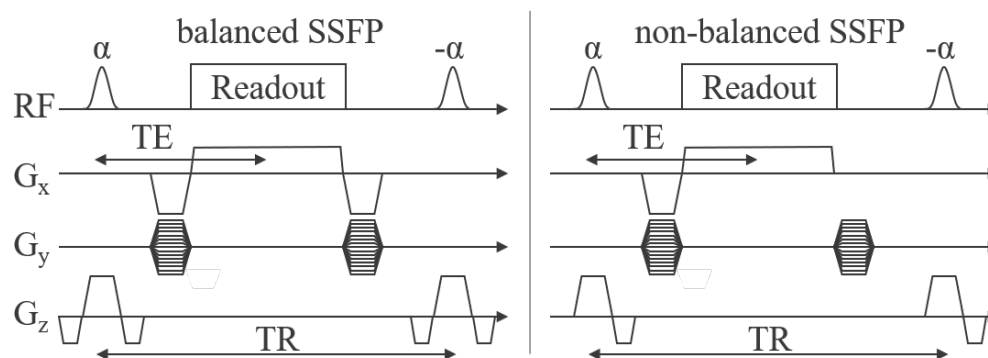


Figure 2.10: Sequence diagram within one TR period for a balanced SSFP (left) and a non-balanced SSFP (right). The sum of all gradient moments of the bSSFP on each axis are compensated, leading to a single magnetization vector at the end of TR . For the unbalanced SSFP, the magnetization after each period is dephased

2.2.6 Steady State Free Precession

The (non-balanced) steady state free precession goes by a variety of commercial names, including FISP and GRASS. The sequence is similar to the bSSFP, only that the gradients are not balanced prior to the RF pulse (Figure 2.10 right). To avoid spoiling the steady state, the accumulated phase of the transversal magnetization needs to be equal in each TR . Further, TR needs to be smaller than T_2 . If these conditions are met, a steady state is reached, producing two types of signals. The first signal is a T_2^* -like signal decay, just after the RF pulse and the second is a time-reversed T_2^* -like signal decay before each RF pulse. Depending if the pre- or post-excitation signal is acquired, the signal has different contrast weightings. The post-excitation contrast weighting, which have the commercial names FISP and GRASS, can be derived by a recursive process. The contrast weighting includes contributions of T_1 and T_2 , depending further on TR and the

flip angle α

$$M_{SS} = M_0 \tan\left(\frac{\alpha}{2}\right) \left(1 - \sqrt{\frac{(e^{-TR/T_1} - \cos(\alpha))^2 (1 - e^{-2TR/T_2})}{(1 - e^{-TR/T_1})^2 - e^{-2TR/T_2} (e^{-TR/T_1} - \cos(\alpha))^2}}\right) e^{-TE/T_2^*} \quad (2.39)$$

The resulting signal comprises of a complicated overlap of the gradient echo and stimulated echoes. The contrast is highly dependent on the flip angle, especially for short TR times. Compared to the FLASH, the advantage of the steady state sequence includes higher signal-to-noise and contrast-to-noise ratio, improving acquisition speed.

2.2.7 Echo Planar Imaging

The Echo Planar Imaging (EPI) sequence collects all necessary data to reconstruct a complete image with one single RF excitation and one readout train. Figure 2.11 shows the sequence diagram and the corresponding k-space coverage. Following the excitation pulse, all k-space lines are acquired subsequently with short phase encoding gradient pulses, called blips. As the images are collected with just one RF excitation and without any spin echoes, the contrast is determined by spin density and T_2^* weighting. EPI sequences have short acquisition times T_{acq} , as the k-space is fully sampled within one readout

$$T_{acq} = T_{rf}/2 + t_0 + N_y(T_{blip} + N_y T_{line}). \quad (2.40)$$

The times T_{rf} , T_{blip} and T_{line} are the duration of the excitation pulse and the application of the phase encoding and readout gradients. N_y represents the number of k-space lines to be acquired. t_0 is the time required for gradient dephasing or rephasing along slice, phase and frequency encoding direction.

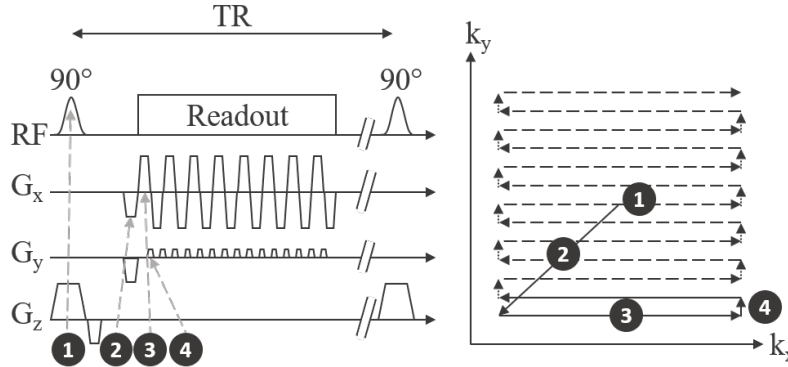


Figure 2.11: Echo planar imaging sequence diagram (left) and k-space trajectory (right). After a single excitation with the application of the slice selection gradient G_z (1), the complete k-space is sampled on a Cartesian grid, using the phase and frequency encoding gradients (2-4)

2.3 Magnetic Resonance Fingerprinting

Magnetic Resonance Fingerprinting (MRF) is a new approach for quantitative MRI, allowing the simultaneous measurement of multiple tissue properties within

a single measurement. The process of creating quantitative maps with MRF can be split into three steps: data acquisition, dictionary simulation and pattern matching. The data acquisition sequences used in MRF are designed to deliberately vary the MR system parameters, e.g. by choosing pseudo random flip angles and repetition times, to generate unique signal paths, termed ‘fingerprints’, depending on the underlying tissue. The acquired fingerprint of each voxel is compared to a large dictionary of simulated fingerprints generated specifically for the respective measurement sequence. The best match between each measured fingerprint of the voxel and the simulated dictionary fingerprints is determined with a pattern matching process. The combination of tissue properties, such as T_1 and T_2 , used to simulate the fingerprint that matched best with the fingerprint of the voxel is identified as the underlying tissue properties of that specific voxel, creating quantified maps.

The following subsections offer an introduction to quantitative MRI and give an overview of the state of the art MRF methods.

2.3.1 Quantitative MRI

Clinical MRI commonly uses qualitative imaging, acquiring the transversal magnetization of one single excitation, which is influenced by a number of parameters. These include the coil sensitivities, proton density and other parameters determined through the measurement setup or acquisition method. This complicates and even prohibits inter-patient comparability, as the measurements don’t necessarily reflect the underlying absolute physical properties.

However, it is possible to quantitatively collect physiological information with MRI by quantifying the physical parameters such as the longitudinal (T_1) or transversal relaxation times (T_2 , T_2^*), proton density, diffusion or perfusion. One idea to quantify the underlying physical properties is to acquire multiple images in such a way, that the contrast weighting in each voxel changes with each subsequent measurement. In the case of quantifying the relaxation parameters, the same voxel will need to be acquired at multiple time points over the range of the T_1 and T_2 values. As the SNR of the images is a function of the relaxation parameters, each tissue will have its own SNR response curve. Therefore, the data points need to be appropriately spaced such that the curve is adequately sampled. The sampled data points are included into an appropriate physical model, such as $a(1 - 2e^{-t/T_1})$ for T_1 . Using a least squares fit or other fitting algorithms, the relaxation parameters can be extracted. For T_1 estimation, typically multiple inversion recovery spin echo measurements are used with varying inversion times TI. To quantify T_2 or T_2^* , a spin echo sequence or FLASH sequence is used, acquiring the same slice at multiple echo times. Full magnetization relaxation needs to be ensured prior to the acquisition of the next slice with a varying TI or TE, leading to long acquisition times for the quantification of a single slice, far beyond what is clinically acceptable.

2.3.2 MRF data acquisition

In comparison to traditional quantitative MRI, where all acquisition parameters are kept constant except for one such as the timing or the flip angle that is varied to induce contrast weighting, MRF varies simultaneously several acquisition

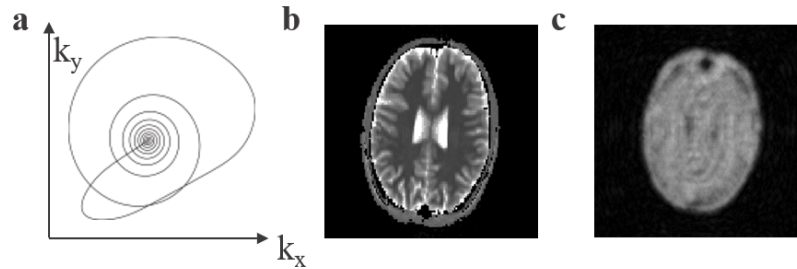


Figure 2.12: (a) Variable density spiral k-space trajectory commonly used for MRF sequences, including bSSFP and SSFP. If the full resolution image (b) gets undersampled in k-space with the spiral trajectory (a), the result is a baseline image with strong artefacts (c).

parameters throughout the measurement. This includes the RF excitation flip angle, the timing of the sequence including TR and TE and the sampling of the k-space trajectory. The aim of the variation is to generate a unique signal for each tissue. Therefore the requirement for the sequence design is to generate these unique fingerprints in a time efficient manner.

MRF acquires many measurements per slice with different contrast weighting. The single measurements will be referred to as 'baseline images'. The time signal of one voxel throughout the measurement with multiple baseline images is the desired fingerprint. MRF needs multiple baseline images per slice to generate a unique fingerprint. In most MRF sequence designs between 500 and 1500 baseline images are acquired per slice. As the reduction of acquisition time is important for volumetric coverage, the repetition time is minimized. For most sequences, the data acquisition of the k-space is the most time-consuming element. Therefore, in MRF the k-space is undersampled, acquiring only parts of the k-space. In many MRF implementations a spiral readout is chosen (Figure 2.12 a), sampling only 1/48th of a full image data set. Further k-space sampling schemes used in MRF sequences include partial Fourier imaging with Cartesian readout or radial trajectories. The undersampling of the k-space can lead to severe artefacts in the baseline images, as depicted in Figure 2.12 c. While the artefacts add a level of noise to the fingerprints, it is of no concern if the undersampling artefacts don't comprise the matching process with the dictionary. The sequences are designed in such a way, that the undersampling artefacts are not stationary in each baseline image, but change their position throughout the measurement, therefore minimizing their effect on the matching process.

The concept of MRF provides a framework for acquiring data and retrieving the quantified values through dictionary matching. Theoretically, any MRI sequence type can be adopted to generate unique signals for specific tissue properties. The original MRF implementation was based on a balanced steady state free precession (bSSFP) method, as this sequence design is sensitive to both T_1 and T_2 . Figure 2.13 shows the sequence diagram of the bSSFP MRF acquisition method. Following an initial inversion pulse to increase T_1 sensitivity of the parameter estimation, multiple bSSFP measurements are acquired in rapid succession. TR and the flip angles are varied throughout the measurement (Figure 2.13 b-c) to induce changes in contrast weightings, generating unique fingerprints. As the original MRF sequence proved to be sensitive to B_0 inhomogeneities, causing

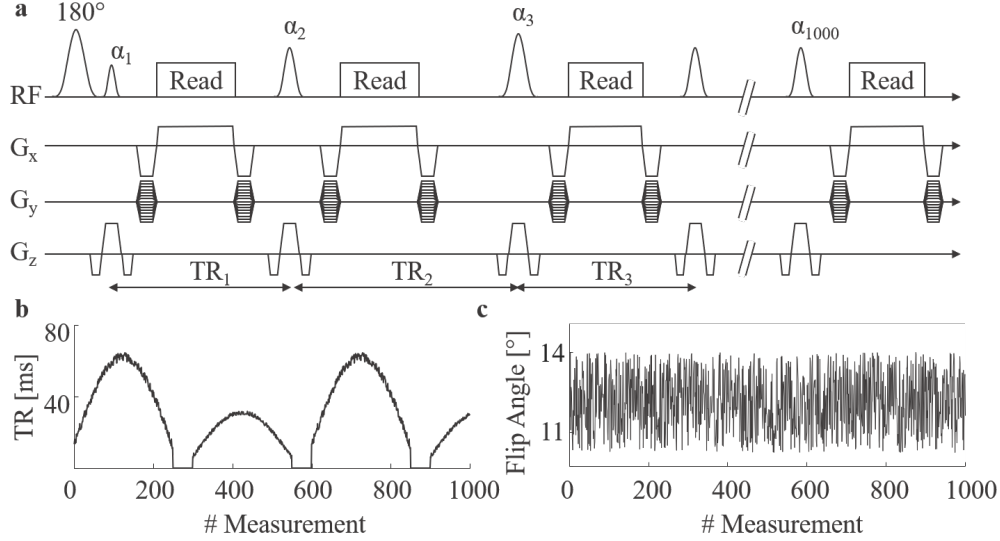


Figure 2.13: (a) Sequence diagram of a bSSFP MRF implementation. Following an initial 180° inversion pulse for increased T_1 sensitivity, bSSFP measurements are acquired in rapid succession, each measurement with a different flip angle α and repetition time TR . By varying the flip angle and repetition time, the baseline images have varying contrast weightings, leading to unique fingerprints for each tissue. Exemplary values for TR and α are shown in (b) and (c), respectively. The basic sequence designs of all MRF methods are similar as shown in (a), always acquiring multiple measurements within a short time span, varying the flip angles and times TR and TE . The differences between the MRF methods are mainly the base sequence type, such as replacing the bSSFP by a SSFP or other readout method.

banding artefacts in the parameter maps, subsequent MRF methods have been proposed to overcome certain limitations, such as a non-balanced steady state free precision MRF (Jiang et al., 2015) or MRF based on pseudo steady-state free precision (Assländer et al., 2017).

2.3.3 MRF Dictionary

To determine the underlying physical parameters of the acquired fingerprint, it is compared with many simulated signals. As all the relevant MRF sequence parameters are known, such as the flip angles α , echo times TE and repetition times TR , the time course signals corresponding to the fingerprints can be simulated. For example, in the case of the original MRF bSSFP sequence, the signals can be simulated with the Bloch Equation to predict the magnetization behavior. The magnetization $m_i = (m_x, m_y, m_z)^T$ at the end of the i -th measurement can be iteratively simulated with the following equation:

$$m_i = E_i R_x(\alpha_i) m_{i-1} + (I - E_i)[0, 0, 1]^T \quad (2.41)$$

with the rotation matrix $R_x(\alpha_i)$ around the x-axis,

$$R_x(\alpha_i) = \begin{bmatrix} 1 & 0 & 0 \\ 0 & \cos(\alpha_i) & -\sin(\alpha_i) \\ 0 & \sin(\alpha_i) & \cos(\alpha_i) \end{bmatrix} \quad (2.42)$$

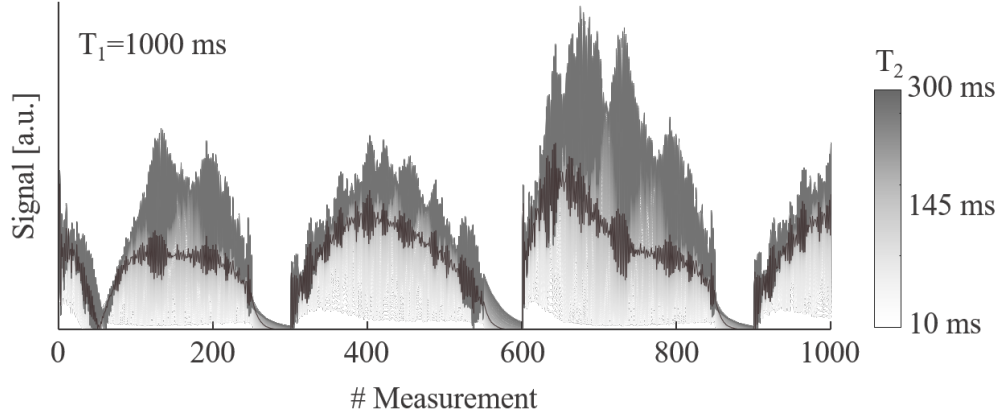


Figure 2.14: Simulated fingerprints of the bSSFP sequence from Figure 2.13. The fingerprints were simulated with the Bloch equations for a range of $T_1=1000$ ms and $T_2=10-300$ ms in steps of 20 ms. Fingerprints strongly differentiate from each other only due to varying T_2 times, offering the benefit that each tissue has a unique fingerprint. One exemplary fingerprint with $T_1=1000$ ms and $T_2 = 96$ is highlighted (dark gray), showing the time course of a single fingerprint

the diagonal relaxation matrix

$$E_i = \begin{bmatrix} e^{-TR_i/T_2} & & \\ & e^{-TR_i/T_2} & \\ & & e^{-TR_i/T_1} \end{bmatrix} \quad (2.43)$$

and the identity matrix I . The only unknown parameters in the Equation 2.41 are T_1 and T_2 , which should be determined. A range of T_1 and T_2 is chosen, covering the expected parameter range of the acquired tissue (e.g. T_1 values from 100 ms to 5000 ms, in steps of 10 ms, as this covers the range of *in vivo* T_1 times). For each T_1 and T_2 combination a fingerprint is simulated and added to the dictionary. As each combination is simulated, the dictionary dimensions can become quite large, e.g. if 100 T_1 and T_2 values are chosen, the dictionary consists of 10,000 fingerprints. Figure 2.14 shows a few exemplary simulated fingerprints of the original bSSFP sequence with the flip angles and repetition times shown in Figure 2.13 b-c.

For some sequence types the Bloch equations cannot be used, as the single isochromat method doesn't represent the magnetization correctly. For SSFP sequences, the extended phase graph formalism is used to generate the dictionary. With ASL-MRF (Wright et al., 2018) and MR vascular fingerprinting, more complex models are used to create dictionaries of fingerprints.

2.3.4 MRF Pattern matching

The parameter maps are determined via pattern matching. The measured fingerprint of each voxel is compared to each simulated fingerprint in the dictionary and the dictionary element with the highest correlation is chosen as the best fit (Figure 2.15). All the parameters that were used to simulate the fingerprint in the dictionary are retrieved and assigned to the corresponding voxel.

The most common template matching method between the fingerprint and each simulated signal of the dictionary is the vector-dot product. The dictionary

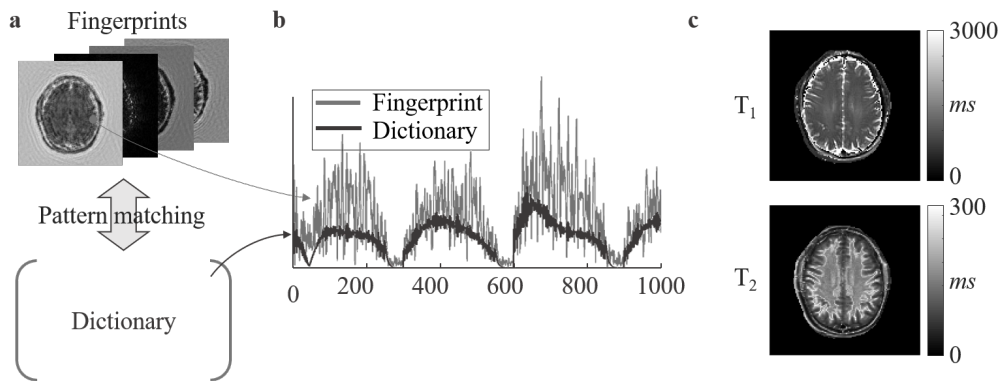


Figure 2.15: MRF pattern matching: (a) The fingerprint of each pixel is matched with all the dictionary elements by calculating the inner product. (b) shows the pattern matching of the fingerprint with the dictionary element with the highest correlation. (c) The parameters, in this case T_1 and T_2 , of the dictionary element with the highest correlation are determined on a pixel-by-pixel basis and converted into quantitative maps

entry with the highest dot product is considered the best match and the corresponding simulation parameters, e.g. T_1 or T_2 , are assigned as the quantitative parameter to that voxel. As the maximum dot product is defined as the decision criterion, each dictionary element D_k of the dictionary $D = \{D_k\}$ needs to be normalized prior to matching, preventing a bias towards dictionary elements with a higher average signal power. The dictionary element which best matches the fingerprint f of a voxel is determined by

$$k = \arg \max_k \frac{\langle D_k, f \rangle}{\|D_k\|_2} \quad (2.44)$$

As the MRF dictionary can be very large, in some cases up to $\approx 500,000$ fingerprints with each 1,000 data points (Ma et al., 2013), the computational complexity of matching each voxel with the dictionary can be time consuming. Since the method needs to be fast, robust and accurate for possible clinical impact, a number of suggestions have been put forth to speed up the matching process. These methods include compressing the time dimension by means of singular value decomposition (McGivney et al., 2014) or using group matching algorithms (Cauley et al., 2015), such that only parts of the dictionary need to be matched, reducing complexity. These methods have yielded time-reduction factors of up to 5.

The resulting quantitative maps of the matching process have high precision and accuracy, which has been shown in repeatability studies on phantoms, resulting in T_1 and T_2 variations of less than 2%.

“Magnetic Resonance Fingerprinting
using Echo-Planar Imaging: Joint
Quantification of T_1 and T_2^* Relaxation
Times” *Magn Reson Med*, doi:
10.1002/mrm.26561

3

3.1 Introduction

Quantification of tissue properties including the relaxation parameters such as T_1 , T_2 and T_2^* using magnetic resonance imaging has long been a major research goal in order to facilitate inter-patient comparability and quantitative diagnosis (Deoni, 2010; Warntjes et al., 2007b). The detection and staging of several diseases have been improved by the possibility to quantify relaxation parameters. Examples include T_1 and T_2^* mapping to investigate the iron content in the brain of patients suffering from Huntington’s, Parkinson’s and Alzheimer’s disease (Ordidge et al., 1994; Vymazal et al., 1999). Further, T_2^* is used for blood oxygenation imaging of the brain and kidneys (Sadowski et al., 2010) and T_1 for multiple system atrophy (Vymazal et al., 1999) and for diffuse ischemic an non-ischemic cardiomyopathy (Bulluck et al., 2015). However, long acquisition times prevent the integration of relaxation parameter mapping into clinical brain scan protocols (Warntjes et al., 2008). Recently, an emerging technique, called magnetic resonance fingerprinting (MRF) (Ma et al., 2013), and various extensions thereof (Assländer et al., 2017; Buonincontri and Sawiak, 2015; Jiang et al., 2017b, 2015; Ye et al., 2015), have been introduced and show exceptional promise for the simultaneous, rapid and robust quantification of multiple tissue characteristics (Chen et al., 2016; Gao et al., 2015). In MRF the acquisition of numerous baseline images with varying imaging parameters such as repetition time (TR) or flip angles (FA) yield spatially resolved, characteristic signal evolutions, which depend on the physical properties of the underlying tissue, such as relaxation times. Matching this ‘fingerprint’ to a precomputed dictionary that contains simulated signal profiles yields quantitative parameter maps.

The original implementation of the MRF paradigm was based on a balanced steady-state free precession (bSSFP) sequence design (Ma et al., 2013). The contrast in a bSSFP sequence allows for joint quantification of T_1 , T_2 , proton density and off-resonance. However, the spin echo character of this sequence induces sensitivity to the choice of flip-angles (Assländer et al., 2017). Also the quantification based on a balanced sequence design has reported to be sensitive

to field inhomogeneities (Assländer et al., 2017). The use of a non-balanced SSFP imaging readout has been introduced to mitigate banding artefacts for the trade-off against decreased signal-to-noise ratio (SNR) (Jiang et al., 2015).

Non-Cartesian imaging is commonly employed to facilitate rapid image readout as required in a MRF sequence. Recently, initial data indicated a high sensitivity of MRF sequences to gradient deviations, due to inherent properties of the non-Cartesian image readout (Hong et al., 2016). Especially spiral trajectories, as used in most MRF sequences, are well known to suffer from detrimental effects on the image quality, caused by gradient inaccuracies. This greatly limits its availability at present and still prevents the wide-spread use of spiral imaging in clinical protocols (Block and Frahm, 2005). A Cartesian realization of the MRF paradigm has recently been proposed with promising image quality in a pre-clinical setting (Buonincontri and Sawiak, 2015), potentially mitigating some of the sensitivities that are inherent to non-Cartesian acquisitions. However, this specific implementation suffered from long scan-times, far beyond, what is clinically acceptable.

Echo-planar imaging (EPI) has been introduced as the first method to allow for single-shot imaging employing the rapid generation of multiple gradient echoes after a single excitation pulse (Mansfield, 1977). Its fast scan-time in the order of ten milliseconds per slice established EPI as clinical gold-standard for almost all functional neuro-imaging applications, such as diffusion (Chilla et al., 2015), perfusion (Logothetis, 2008) and BOLD imaging (Hennig et al., 2003). Simple corrections for gradient delay errors and eddy-current induced deviations, and distortion corrections, are readily available on most MRI systems (Schmithorst et al., 2001). Recently, initial results in phantom measurements at ultra-low fields have demonstrated the potential of multi gradient echo techniques for generating fingerprints (Sarracanie et al., 2015).

In this study we present a sequence for acquiring MRF data based on spoiled EPI readouts for joint T_1 and T_2^* quantification, as an alternative to balanced non-Cartesian imaging, potentially facilitating improved robustness and increased usability. The quantification accuracy of the proposed method was evaluated in phantom scans and *in vivo* validation was performed in healthy volunteers.

3.2 Methods

3.2.1 Pulse sequence design

The proposed MRF strategy (MRF-EPI) is based on the acquisition of a series of GE-EPI images with varying flip angles (FAs) and echo times (TEs) to enable the joint quantification of T_1 and T_2^* . To optimize scan-time, minimal TR was chosen for any given TE. As shown in the sequence diagram in Figure 3.1, a single non-selective adiabatic hyperbolic secant inversion pulse is applied at the beginning of the sequence followed by multiple EPI readouts. To suppress chemical-shift artefacts commonly observed with EPI sequences (Edelman et al., 1994), a fat suppression using spectrally-selective saturation is applied before each excitation (Haase et al., 1985). To eliminate residual transverse magnetization from the non-selective excitation, crusher gradients with equal polarity are performed before and after the saturation pulse. Additionally, RF spoiling was included in

the excitation pulse with a phase increment of 50° (Preibisch and Deichmann, 2009).

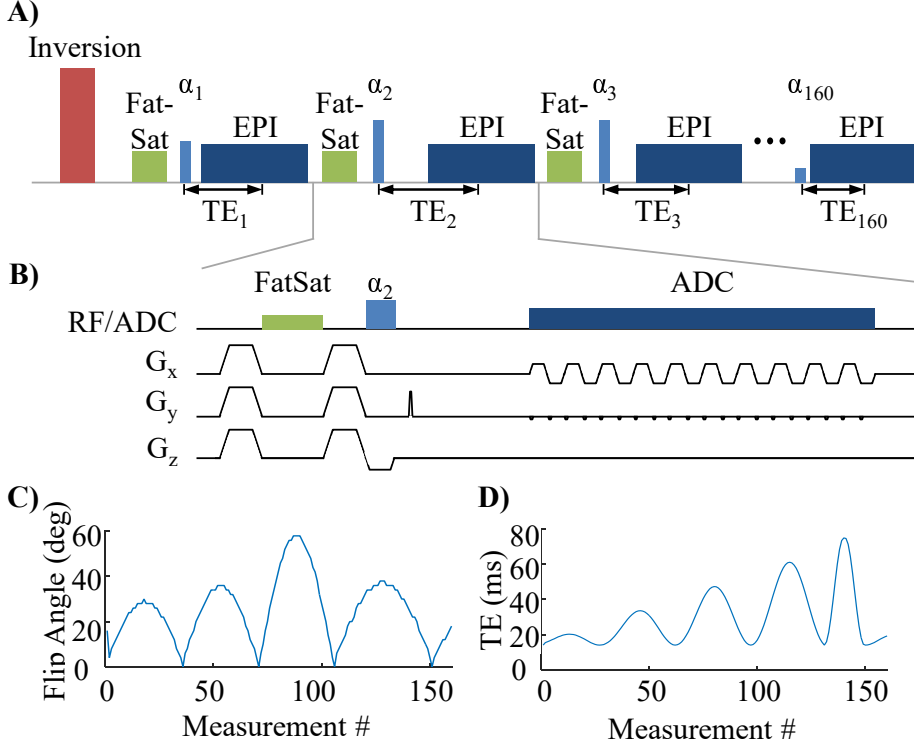


Figure 3.1: (A) Schematic diagram of the MRF-EPI with multiple EPI readouts, each with a different echo time and flip angle. (B) Each EPI excitation and readout is preceded by a fat saturation module including gradient spoiling. (C,D) Profiles of the flip angle and echo time variations used for the MRF measurements.

The flip angles of the baseline images were chosen with a pattern previously proposed by (Jiang et al., 2015). A range of TEs from 14-75 ms was chosen, which results in additional T_1 and T_2^* weighting in the proposed sequence design. The distribution of TEs (see Figure 3.1 d) was empirically selected with 1) a majority of short TEs to result in good SNR and short scan-times 2) a few long TEs to increase sensitivity to tissues with long T_2^* values and 3) an alternating pattern to create large contrast variations.

3.2.2 Dictionary

The dictionary was generated off-line using MATLAB (The MathWorks; Natick, MA) by simulating the evolution of the magnetization \vec{m} based on Bloch-equation simulations. The magnetization vector $(m_l^x, m_l^y, m_l^z)^T \in \mathbb{R}^3$, describes the initial magnetization after the inversion pulse as $\vec{m}_0 = [0, 0, -1]^T$, assuming perfect inversion. The magnetization at the end of the l th measurement can then be described as

$$\vec{m}_l = S \left(E_l R_x(k\alpha_l) m_{l-1} + (Id - E_l) [0, 0, 1]^T \right) \quad (3.1)$$

where $R_x(k\alpha)$ denotes a rotation about the x-axis by the angle α induced by the excitation pulse. To compensate for deviations from the nominal flip angle due

to imperfect excitation slice-profiles and inhomogeneities in the transmit field, a B_1^+ correction was implemented within the dictionary as previously proposed by (Buonincontri and Sawiak, 2015): the dictionary was extended to allow for a B_1^+ amplitude correction using a linear scaling factor k in the range of 0.6-1.4 in steps of 0.1. The step size was set to 0.1 to limit the size of the dictionary, as the dictionary size scales linearly with the number of steps. $Id \in \mathbb{R}^{3 \times 3}$ denotes the identity matrix, $S = [0 \ 0 \ 0; 0 \ 0 \ 0; 0 \ 0 \ 1]$ represents the spoiling of the transverse magnetization at the end of each measurement and E_l is the diagonal relaxation matrix:

$$E_l = \begin{pmatrix} e^{-TR_l/T_2^*} & & \\ & e^{-TR_l/T_2^*} & \\ & & e^{-TR_l/T_1} \end{pmatrix} \quad (3.2)$$

While T_2^* dephasing is generally described by a non-exponential signal decay (Dahnke and Schaeffter, 2005; Yablonskiy and Haacke, 1994), the use of a single exponential decay as approximate signal model is the most used method (Anderson et al., 2001; Ellingson et al., 2013; Mamisch et al., 2011). To allow for comparability to this method, single exponential mapping was used for T_2^* quantification. The MRF dictionary consisted of 157,938 entries with the following parameter range: $T_1 = 20$ -2,000 ms in steps of 10 ms, and 2,000-6,000 ms in steps of 500 ms; $T_2^* = 10$ -100 ms in steps of 2 ms, and 100-300 ms in steps of 5 ms. Unrealistic entries with $T_1 < T_2^*$ were discarded.

3.2.3 Pattern validation

The maximum TE of the TE pattern was chosen by calculating the quantification precision of T_2^* in dependence of various TE patterns. Fingerprints in the range of $T_1 = 1000$ ms and $T_2^* = 50$ -250 ms were simulated by linearly scaling the TE pattern so that TE_{max} was in the range of 14-100 ms and matched to the dictionary in the presence of noise. The SNR was set to 10, each fingerprint was matched 10,000 times with different noise, remaining sequence parameters were simulated as described above. To ensure separability of the dictionary elements in the presence of noise, the stability of the parameter quantification from MRF data was studied, thereby testing the influences of noise on the fingerprints. For this the inverse problem describing the parameter extraction from MRF data f was locally linearized. Two exemplary relaxation constants set in the *in vivo* range and the noise amplification, induced by the inverse problem as a function of the overall number of images in the fingerprint, was analyzed. The MRF system was linearized for variable fingerprint length m

$$f_m(\theta + \Delta\theta) = f_m(\theta) + J_{f_m}(\theta) \Delta\theta + o(|\Delta\theta|) \quad (3.3)$$

Here $f_m : \mathbb{R}^3 \mapsto \mathbb{R}^m$ describes the Bloch-simulation, just as commonly used in MRF to generate the magnitude fingerprints, from simulated parameter values $\theta = [T_1, T_2^*, M_0]$. f_m is a continuous function in θ . $J_{f_m}(\theta)$ denotes the corresponding Jacobian Matrix for the parameters θ . In linear approximation the error amplification in the recovery of parameters $(\theta + e)$ from the noisy fingerprint $(v + n)$ can be described as

$$\begin{aligned} v + n = f_m(\theta + e) &= f_m(\theta) + J_{f_m}(\theta) e + o(|e|) \\ \xrightarrow{f_m(\theta)=v} & e = J_{f_m}(\theta)^\dagger n + o(|e|) \end{aligned} \quad (3.4)$$

Where $J_{f_m}(\theta)^\dagger$ denotes the pseudo-inverse of the Jacobian. The noise vector n is assumed to be normally distributed with zero mean and standard-deviation $n \sim N(0, \sigma^2)$. For sufficiently large SNR, $o(|e|)$ can be neglected and is ignored for the rest of the analysis. To represent equal scan time, the noise variance σ^2 is normalized by the number of images ($\sigma^2 = m \sigma_0^2$), i.e. a lower number of images can be acquired with increased SNR. In the linear approximation, it follows that the components of e are normally distributed, as a sum of normal distributions in the noise input. Specifically, $e_{T_1} \sim N(0, \sigma_{T_1}^2)$ and $e_{T_2^*} \sim N(0, \sigma_{T_2^*}^2)$. The variance of the error vector can then be described, as a result from the sum of normal distributions:

$$\sigma_{T_1}^2 = \sigma^2 \sum_{i=1}^m |j_{1i}^\dagger(\theta)|^2 \quad (3.5)$$

with $j_{ik}^\dagger(\theta)$ denoting the elements of the pseudo inverse of the Jacobian matrix, $J_{f_m}(\theta)^\dagger$. Normalized by the variance of the input noise, it follows

$$\frac{\sigma_{T_1}}{\sigma_0} = \sqrt{m \sum_{i=1}^m |j_{1i}^\dagger(\theta)|^2}, \quad \frac{\sigma_{T_2^*}}{\sigma_0} = \sqrt{m \sum_{i=1}^m |j_{2i}^\dagger(\theta)|^2} \quad (3.6)$$

and $\frac{\sigma_{T_2^*}}{\sigma_0}$ were used to describe the noise amplification in the parameter recovery from MRF data, at various number of images. To study the noise amplification, two linearization points θ_G, θ_W , were chosen to correspond to gray- and white-matter ($T_1, T_2, M_0 = 1800$ ms, 50 ms, 1/1000 ms, 40 ms, 1) and the noise amplification $\frac{\sigma_{T_1}}{\sigma_0}$ and $\frac{\sigma_{T_2^*}}{\sigma_0}$ was calculated for fingerprint length of $3 \leq m \leq 3000$.

3.2.4 Pattern matching

Dictionary matching was performed by calculating the inner product between the magnitude of the dictionary entries and the magnitude of the measured signal. Dictionary matching based on correlation corresponds to a grid search minimization of the least squares error. This represents a maximum likelihood estimator for Gaussian noise. Hence, the Rician noise distribution, commonly observed in MRI magnitude data (Gudbjartsson and Patz, 1995), potentially induces inaccuracy in the parameter estimation. To study the effect of Rician noise on the accuracy of the magnitude based dictionary matching, numerical simulations have been performed. Rician noise was added to a simulated signal with relaxation times the *in vivo* range ($T_1/T_2^* = 1000$ -2000 ms/30-130 ms) to generate SNR values between 2 and 10. For each SNR value, 5,000 signals with added noise were matched to the dictionary and the average difference between the matched and original relaxation parameters was calculated.

3.2.5 Sequence Parameters

Imaging was performed on a 3 T whole-body scanner (Magnetom Trio; Siemens Healthcare, Erlangen, Germany) using the whole body coil for transmission. A 32-channel head receiver array was used for *in vivo* measurements and a flex coil in combination with the spine coil for phantom scans. This study was approved by the local institutional review board (IRB) and all subjects provided

written informed consent, prior to examination. The following image parameters were used for all MRF-EPI phantom and *in vivo* measurements: bipolar k-Space trajectory, TE/TR = 14-75 ms/48-109 ms, flip angle = 0-58°, matrix/FOV = 128 × 128/220 × 220 mm², BW = 1395 Hz/pixel, slice thickness = 5 mm, total gradient moment per spoiler = 69.6 mT/m*ms, partial-Fourier = 6/8, parallel imaging factor = 3 with GRAPPA reconstruction (Griswold et al., 2002), reference lines = 60 acquired in-place for each baseline image, gradient delay correction based on three navigator echoes, acquired prior to each readout, static geometric distortion correction (Wang et al., 2004), adaptive reconstruction of phased array (Walsh et al., 2000), frames = 160, acquisition time per slice = 10 s.

Reference values for T_1 were obtained using an inversion recovery turbo spin echo (IR-TSE) sequence with the following sequence parameters: 5 images, TI = 50-1600 ms, TE/TR = 6 ms/15 s, turbo factor = 16, matrix/FOV = 128 × 128/220 × 220 mm², BW = 399 Hz/pixel, scan time = 10 min 0 sec. To estimate T_2^* times in phantoms, a spoiled gradient echo sequence (GRE) was employed and six images were acquired using the following parameters: TE = 5-80 ms, TR = 1000 ms, alpha = 15°, matrix/FOV = 128 × 128/220 × 220 mm², BW = 391 Hz/pixel, scan time = 12 min 48 sec. For *in vivo* measurements, a multi-gradient echo (GRE) sequence was employed due to shorter scan time, twelve images were acquired using the following parameters: TE = 5-80 ms, TR = 300 ms, alpha = 25°, matrix/FOV = 128 × 128/220 × 220 mm², BW = 391 Hz/pixel, echo spacing: 7 ms, scan time = 39 sec. Reference values for T_1 and T_2^* were determined voxel-wise, fitting a three-parameter model for T_2^* ($ae^{-t/T_2^*} + c$) and two-parameter model for T_1 ($a(1 - e^{-t/T_1})$) to the image magnitudes using a nonlinear least-squares fitting algorithm.

In each MRF-EPI acquisition one slice was acquired as proof of concept. *In vivo* measurements consisted of three consecutive single MRF-EPI acquisitions.

3.2.6 Phantom Experiments

The effectiveness of gradient and RF spoiling of the MRF-EPI was tested in phantoms. The spoiling gradients were played with equal polarity both before and after the fat saturation pulse. In order to validate the thorough suppression of fat and water frequency components, 10 MRF-EPI measurements of a two compartment phantom containing fat and water were obtained. SNR for phantom and *in vivo* measurements was calculated as following: $SNR = S_{mean} / \left(\sqrt{\frac{2}{4-\pi}} \sigma_{stdv} \right)$, where S_{mean} is the average signal in the magnitude image, σ_{stdv} is the standard deviation in a noise area of the magnitude images and $\sqrt{\frac{2}{4-\pi}}$ is a correction factor for the Rayleigh distribution of background noise in magnitude images (Dietrich et al., 2007).

To validate the quantification accuracy of MRF-EPI, phantom experiments were performed and compared to gold standard sequences. Separate measurements of nine phantoms were performed, each with a single gadoterate-meglumine (Dotarem; Guerbet, Villepinte, France, concentration: 0.075-0.15 μmol/ml) doped agarose compartment (concentration: 0.5-1.5 w/w %). The accuracy of MRF-EPI was assessed by comparing the mean relaxation times

in manually drawn ROIs delineating each phantom. Average deviations from the reference sequences were evaluated for both MRF data with and without B_1^+ correction.

The difference between complex and magnitude matching was tested by acquiring 10 complex valued EPI-MRF measurements of each phantom. T_1 and T_2^* were quantified using both complex and magnitude matching. The corresponding precision defined as the variation across the 10 repetitions was calculated for each matching method. For complex matching, the dictionary equation was extended for off resonance by including the factor $R_z(\varphi_l)$

$$\vec{m}_l = S \left(E_l R_z(\varphi_l) R_x(k \alpha_l) \vec{m}_{l-1} + (Id - E_l) [0, 0, 1]^T \right) \quad (3.7)$$

which denotes rotation about the z-axis by the angle $\varphi_l = 2\pi f TR_l$ with the off-resonance frequency f in a range of 0-40 Hz in steps of 2 Hz.

3.2.7 *In vivo* experiments

In vivo images of six volunteers (4 females, 2 males 26 ± 2 years old) were acquired in three imaging slices each. *In vivo* parameters maps were obtained with the proposed MRF-EPI and compared with the IR-TSE and the GRE sequence, for T_1 and T_2^* measurements, respectively. To quantitatively compare the accuracy, T_1 and T_2^* values were obtained for white and gray matter by manually placing ROIs in the parietal lobe and in the cortex of the frontal lobe and comparing the mean relaxation times. The images were masked for displaying purpose.

3.3 Results

3.3.1 Pattern Validation

All dictionaries were computed in approximately 10 minutes using a standard desktop computer.

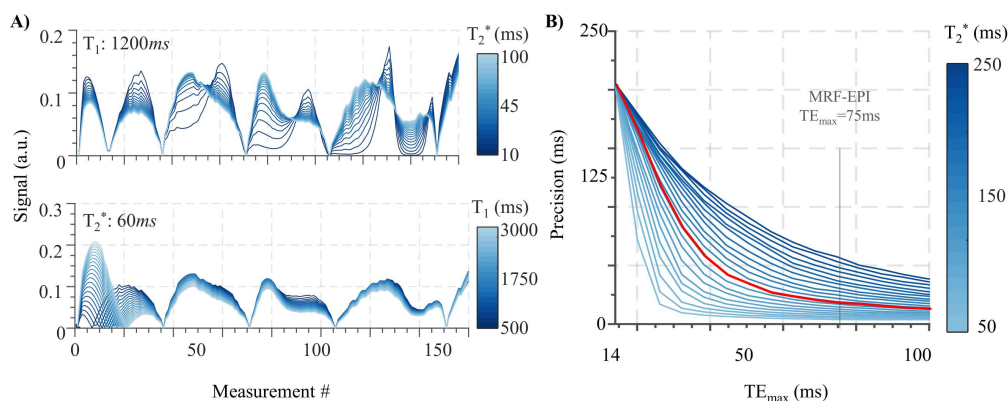


Figure 3.2: (A) Exemplary fingerprints from the simulated dictionary for a range of T_1 and T_2^* values. (B) Quantification precision in dependence of the maximum TE time of the TE pattern for a variety of T_2^* values ($T_1 = 1000$ ms), $T_2^* = 150$ ms in red. For short T_2^* values a TE pattern with small TE_{max} provides sufficient precision, this does not hold for long T_2^* values.

Figure 3.3: Conditioning of the inverse problem involved in parameter recovery from MRF data, analyzed as noise amplification. Low numbers of measurements lead to ill conditioning, convergence of the noise amplification is observed at higher numbers of measurements.

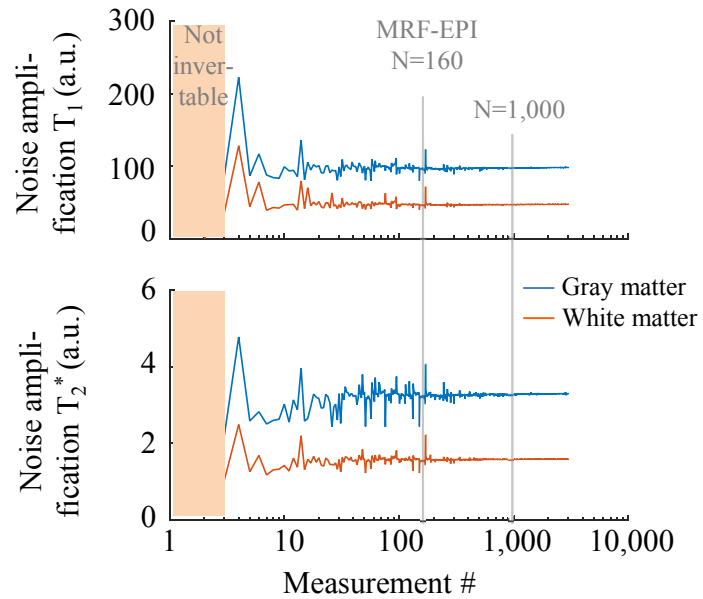


Figure 3.2 a) shows exemplary fingerprints of 40 dictionary elements with varying T_1 (500-3000 ms) and T_2^* (10-100 ms) values. Major contrast variations in the fingerprints are observed at various simulated T_1 and T_2^* . Figure 3.2 b) shows the dependency of the precision from TE_{max} . For short T_2^* values a TE pattern with small TE_{max} provides sufficient precision, for long T_2^* values > 200 ms, the gradient of the precision curve has not saturated at $TE_{max} = 100$ ms. $TE_{max} = 75$ ms was chosen as a compromise between precision and measurement time which gives sufficient precision in the *in vivo* range of T_2^* (< 150 ms). Figure 3.3 shows the estimated noise amplification in the linearized MRF system in dependence of the number of measurements for T_1 and T_2^* parameters. For an insufficient number of measurements (< 3), the system is ill-conditioned. However, at larger number of measurements the conditioning of the system quickly converges, showing minor differences for very high numbers of baseline images.

3.3.2 Pattern Matching

Figure 3.4 shows the inaccuracies to the parameter estimation based on the dictionary matching induced by the Rician noise distribution. The resulting fit accuracy is dependent on the underlying relaxation parameters (Figure 3.4 a)) and the imaging SNR (Figure 3.4 b)). At very low values (SNR = 2), deviations up to 8.9 % are observed, where T_1 measurements tend to be overestimated while T_2^* is underestimated for small values and overestimated for large values. However, at noise levels observed in the *in vivo* experiments (SNR > 30) it induces inaccuracies well below 1 %.

3.3.3 Phantom Experiments

Figure 3.5 shows SNR of water and fat compartment throughout the measurement, after fat suppression, gradient spoiling and RF-pulse. Visually complete spoiling of the transverse magnetization can be observed in frame 106, while fat suppression using spectrally selective saturation can be seen in both frames

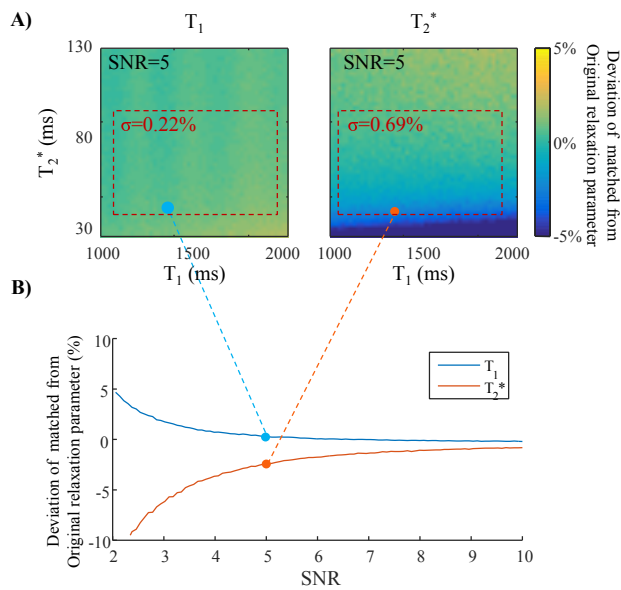


Figure 3.4: (A) Simulation of fit accuracy (relative deviation: $\Delta T_1/T_1$, $\Delta T_2^*/T_2^*$) of the MRF-EPI method with noise (SNR = 5) in dependence of T_1 and T_2^* . T_1 fit error with noise is similar for all T_1 and T_2^* values. For small T_2^* values, the same noise increases the fit error in comparison to larger T_2^* values. (B) Simulation of fit accuracy of the MRF-EPI method in dependence of SNR for a given T_1 and T_2^* (1400 ms, 40 ms). With higher SNR values the deviation of the matched from the original relaxation parameter becomes smaller.

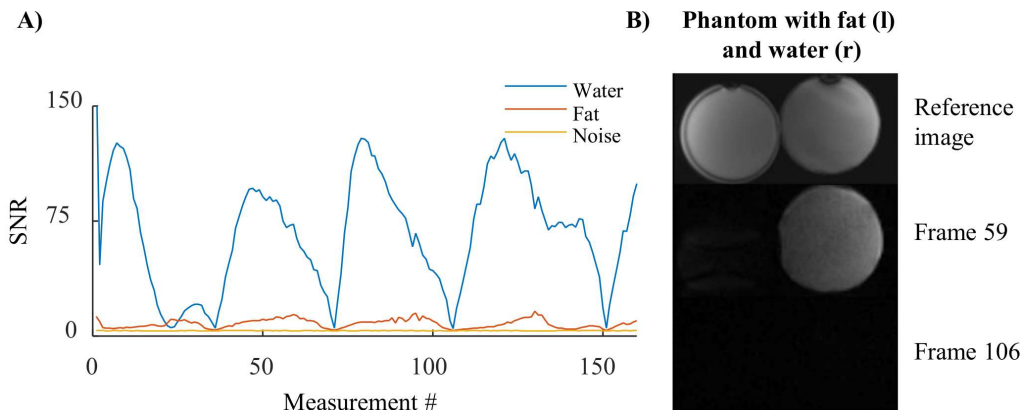


Figure 3.5: (A) Average SNR (of a ROI across 10 measurements) per base line image of water and fat phantom throughout the measurement. (B) Efficient fat suppression using spectrally selective saturation can be seen in both frames (59,106). Effective gradient spoiling can be observed in frame 106, as no residual water signal from previous excitation can be detected after $\alpha = 0^\circ$ pulse.

59 and 106. Figure 3.6 shows the T_1 and T_2^* maps of the phantom experiments using MRF-EPI with B_1^+ correction. The proposed method with B_1^+ correction yields homogenous T_1 estimates within the phantoms. All T_2^* maps show a higher degree of variation than T_1 maps, due to unavoidable susceptibilities and large field inhomogeneities influencing the T_2^* values. Without B_1^+ correction, both T_1 and T_2^* times are substantially underestimated using MRF-EPI (T_1 deviation from IR-TSE in the range from -18 % to -5 %, T_2^* deviations from GRE in the range from -15 % to 13 %). This trend is mitigated by including a B_1^+ correction in the matching of the MRF-EPI sequence, resulting in slight, residual underestimation of T_1 values (deviation: -2 ± 3 % [min: -5 % max 2 %]), and a decreased deviation from the reference T_2^* (deviation: 2 ± 3 % [min: -4 %, max 4 %]), times.

Figure 3.7 a) shows that complex matching results in a 2-fold (2.2 ± 0.7) and 3-fold (3.0 ± 1.0) higher quantification variance than magnitude matching in

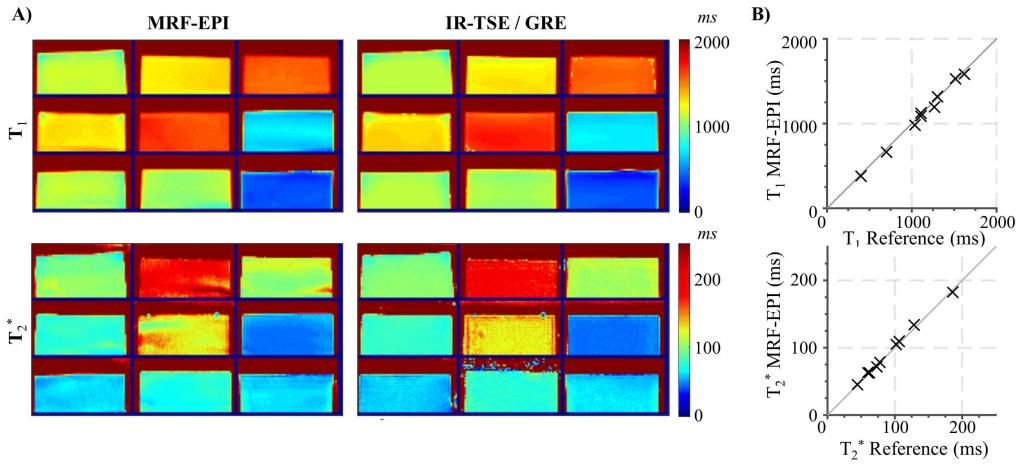
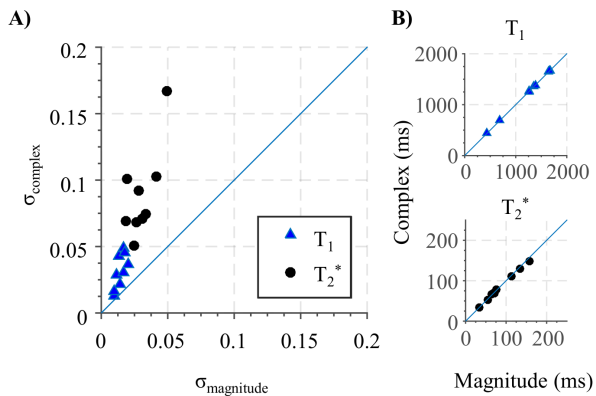


Figure 3.6: (A) T_1 and T_2^* maps obtained in phantom measurements using MRF-EPI and the respective reference method IR-TSE and GRE. Visually comparable image quality is observed between MRF-EPI and the gold standard in the T_1 maps. Slightly decreased homogeneity throughout the phantom compartments is obtained in the T_2^* maps, due to unavoidable field inhomogeneities. (B) Comparison of T_1 and T_2^* values of MRF-EPI with the reference methods, showing good agreement between the average relaxation times in all phantoms.

Figure 3.7: (A) Quantification variance of the phantoms for complex and magnitude matching. Complex dictionary matching leads to a higher quantification variance than magnitude matching. (B) Quantified relaxation times T_1 and T_2^* of the phantoms are nearly identical for complex and magnitude matching.



phantom scans, for T_1 and T_2^* respectively. Figure 3.7 b) shows that the quantified relaxation times of the phantoms are nearly identical for magnitude and complex matching (deviation of complex from magnitude matching T_1/T_2^* : $0 \pm 1\%$ / $-2 \pm 2\%$).

3.3.4 In vivo Experiments

MRF-EPI data was successfully acquired in all volunteers. The achieved image quality allowed for further post-processing of all data sets. Figure 3.8 shows an exemplary fingerprint of a healthy subject. MRF baseline images show high image quality with no visible imaging artefacts. Strongly varying T_1 and T_2^* weighting can be observed over the course of the measurement. The signal intensity periodically increases and decreases due to the sinusoidal choice of the FAs.

Figure 3.9 shows representative T_1 and T_2^* maps of the MRF-EPI and the gold standard measurements from one healthy subject. The mean T_1 and T_2^* values obtained with MRF-EPI and gold standard sequences measured in manually drawn

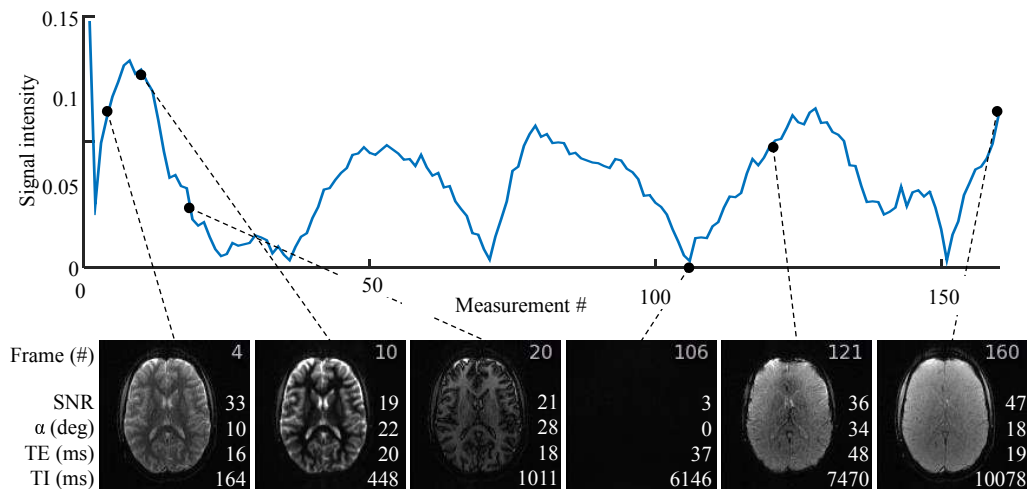


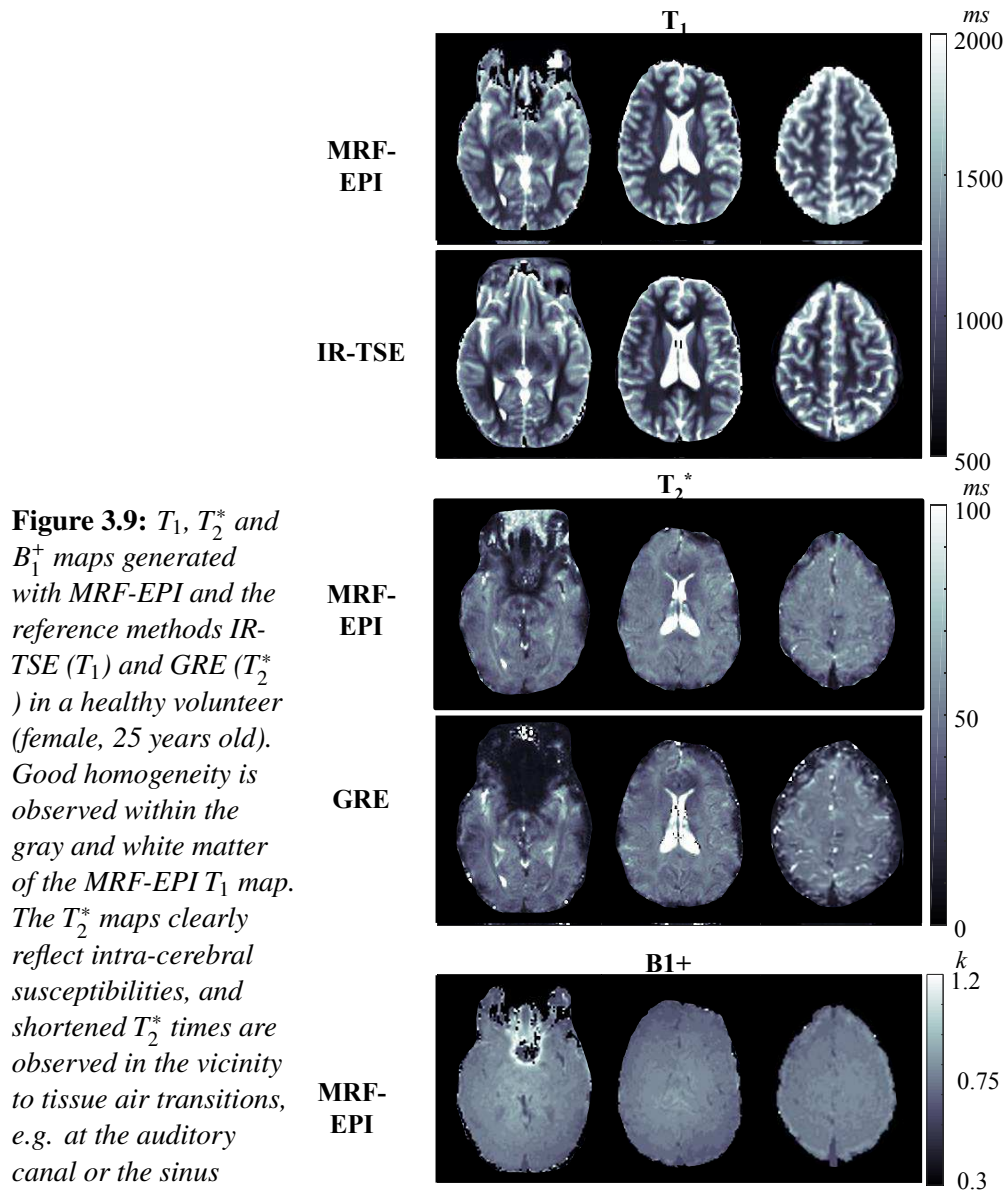
Figure 3.8: Fingerprint from one voxel of a healthy subject (male, 30 years old) and exemplary images with corresponding TE, TI (scan time since inversion pulse) flip angle α and SNR, reconstructed from individual EPI readouts showing highly varying contrast over the course of the measurement. Strongly T_1 weighted contrast is observed in the beginning of the measurement (#4, #10), while increasing T_2^* weighting is observed at the end of the sequence (#121, #160).

ROIs were: white matter 831 ± 62 ms/ 50 ± 1 ms (MRF-EPI), 790 ± 56 ms/ 48 ± 3 ms (gold standard), gray matter: 1818 ± 175 ms/ 50 ± 4 ms (MRF-EPI), 1751 ± 131 ms/ 48 ± 6 ms (gold standard). T_1 maps are homogenous throughout gray and white matter, respectively. T_2^* maps show detailed structures and intracerebral susceptibilities. Strong T_2^* shortening is apparent close to tissue / air interface at the auditory canal or the sinus.

3.4 Discussion

In this study we have proposed an EPI based MRF method, that allows for rapid quantification of T_1 and T_2^* times in 10 seconds per slice. Good quantification accuracy was shown in phantom scans, comparable to previously proposed methods (Jiang et al., 2015). *In vivo* scans yielded robust and artefact free parameter maps, with *in vivo* relaxation parameter values that are in good agreement with the reference scans.

In comparison to the spiral readout of the bSSFP-MRF proposed by (Ma et al., 2013), the EPI-MRF single shot acquisition is considerably slower, as it does not allow for the same level of undersampling. Therefore, only a reduced number of frames can be acquired during a 10 second measurement, despite the use of parallel imaging to accelerate data acquisition. However, the fewer frames benefit from higher SNR. The noise resilience of the parameter maps is a function of the number and the SNR of the baseline images, and the net effect of this trade-off is to be assessed in future studies, in order to allow for optimized acquisition strategies. To ensure robust parameter quantification by the means of dictionary matching despite the greatly reduced number of baseline images compared to (Ma et al., 2013), we analyzed the conditioning of the inverse problem involved in an MRF reconstruction. The minor difference in the noise amplification between MRF systems with 160 and 1000 images indicates robust dictionary matching



with the proposed approach. Further dedicated optimization of the conditioning of the inverse problem combined with the sequence parameters should offer further improvements of the method.

Numerous strategies for increased undersampling and scan-time reduction in EPI have been proposed (Holdsworth et al., 2008; Jeong et al., 2013), with particularly high-undersampling potential for the acquisition of series of EPI (Kellman et al., 2001; Madore et al., 1999). Among these, the introduction of simultaneous multislice imaging (SMS), has recently received widespread attention, as it facilitated acceleration factors up to 16 in EPI acquisitions (Barth et al., 2016; Moeller et al., 2010). This acceleration potential has also been leveraged in quantitative imaging with non-Cartesian MRF (Ye et al., 2015). Further, multi shot acquisition is a way to shorten the acquisition window, however full magnetization relaxation is required between different acquisitions. Therefore, the integration of undersampling strategies in the proposed EPI-MRF, bears great potential to reduce scan-time, or increase the number of imaging frames, and warrants investigation in future studies.

Spiral imaging requires accurate calibration and complex post-processing algorithms to alleviate effects of hardware inaccuracies (Block and Frahm, 2005). Despite excellent readout gradient efficiency and good undersampling properties (Glover, 2012), spiral imaging has rarely found integration into clinical scan-protocols. This highly restricts the availability of the required calibration and necessary post-processing schemes to a limited number of centers world-wide (Block and Frahm, 2005). EPI and accompanying post-processing techniques to reduce distortion and gradient deviation induced image quality deterioration, on the other hand, are readily available for clinical usage and highly accessible at almost all clinical MRI systems.

Recent data indicated sensitivity of MRF parameter quantification to system imperfections, due to inherent properties of the non-Cartesian data acquisition, as shown for radial imaging (Hong et al., 2016). Spiral imaging is well known to also suffer from substantial image quality degradation in the presence, of gradient deviations and trajectory mismatches, for example caused by eddy current effects (Alley et al., 1998). This could potential translate into quantification errors in a MRF acquisition. Bipolar EPI imaging on the other hand, is commonly performed with auto-calibration to compensate for gradient delay errors and eddy current effects, providing a certain degree of robustness to this source of system imperfection (Schmithorst et al., 2001).

In our numerical simulations, we observed compromised quantification accuracy, at very low SNR values, due to non-zero mean noise characteristics in the magnitude data. While, MRF-EPI was shown to provide sufficient baseline SNR, to circumvent this problem, previously reported techniques used high undersampling and showed substantially lower SNR in the baseline images. To ensure optimal quantification accuracy at ultra-low SNR values, it seems essential that zero-mean characteristic is maintained in the noise from all sources, including thermal noise, as well as undersampling induced noise.

Previously proposed realizations of the MRF idea were based on SSFP sequences, which potentially cause additional hardware specific inaccuracies. Firstly, this introduces susceptibility to banding artefacts. Therefore, most recent MRF sequences were based on non-balanced SSFP sequences alleviating off-resonance sensitivity for the trade-off against a drop in SNR (Jiang et al., 2015). Secondly, to obtain uncompromised signal in a SSFP acquisition, the spin echo character of the sequence needs to be maintained, despite varying flip-angles. Assländer et al. formulated a smoothness condition for the flip-angle pattern to ensure uncompromised quantification accuracies in SSFP MRF-acquisitions (Assländer et al., 2017). However, this does not allow for alternating flip-angle patterns, which have previously shown to greatly improve intrinsic B_1^+ correction (Buonincontri and Sawiak, 2015). Thirdly, long trains of SSFP sequences are known to suffer from incomplete gradient refocusing, potentially introducing phase accumulation errors (Barnett et al., 2008). However, especially in the presence of spiral gradients accurate rewinding poses a challenging problem (Kim et al., 2004). The proposed method is based on gradient and RF spoiled imaging, which is resilient to banding-artefacts and incomplete gradient refocusing, and potentially allows for arbitrary flip-angles. Sequences based on EPI readout suffer from their own set of challenges. The most common artefacts are geometric distortions due to mistiming or inaccuracy in the gradient amplitude induced by residual eddy currents (Chen and Wyrwicz, 1999). Field inhomogeneities

can further lead to blurring, Nyquist ghosting (Tsao, 2010) and signal loss, the latter often seen in the temporal and frontal lobes (Ojemann et al., 1997). As these effects have long been target of research, robust algorithms are available for most of the named artefacts, such as acquiring flied maps (Chen and Wyrwicz, 1999) to correct geometric distortions. With the presence of solid correction algorithms, EPI compatible MRI hard- and software is installed worldwide and supported by commercial vendors throughout the world, providing robust EPI sequences used in clinical routine (Poustchi-Amin et al., 2001). Given the distinct profile of artefacts and sensitivity to hardware inaccuracies compared with spiral SSFP MRF sequences, the proposed implementation might offer a complimentary approach to study and utilize the MRF paradigm. The overall performance compared with existing MRF sequences in various clinical or research settings, is to be evaluated in future studies. The proposed method was used to jointly assess T_1 and T_2^* tissue characteristics. Both have been shown to be of clinical interest as highly specific biomarkers for distinct pathologies (Anderson et al., 2001; Dahnke and Schaeffter, 2005; Yablonskiy and Haacke, 1994). The original MRF method proposed the joint quantification of T_1 and T_2 maps. This can also be achieved in MRF-EPI by employing refocused EPI readouts to induce T_2 weighting. Increased SNR can be expected in refocused EPI readouts and the real part of the imaging data, can be readily used in post-processing due to the elimination of off-resonance dependencies. Hence, MRF-EPI bares promise for robust T_1 and T_2 quantification, and should be subject of further research.

This study and the proposed method have several limitations. No direct comparison to the originally proposed MRF method could be performed, due to the lack of robust spiral imaging at our center. Also, only a small number of healthy subjects were scanned to prove the *in vivo* feasibility. Larger cohorts with increased coverage of the complete brain and specific diseases are to be evaluated in order to test the specificity of the parameter quantification provided by MRF-EPI.

The proposed method employed a simplified B_1^+ correction compared to previous studies (Buonincontri and Sawiak, 2015), where the authors proposed to alter the flip-angle scheme in order to increase B_1^+ estimation accuracy. However, to demonstrate feasibility in a comparable fashion to the original MRF method, the original flip-angle scheme was employed, accepting a slight drop in accuracy. Nevertheless, incorporating B_1^+ estimation in the dictionary greatly improved parameter estimation, while the resulting B_1^+ map possibly suffers from systematic errors, as shown by (Buonincontri and Sawiak, 2015). Furthermore, to avoid the susceptibility to off-resonances the magnitude data was used for pattern matching. Complex matching of the data can be employed to derive additional off resonance maps. However, the increased number of fit parameters results in lower quantification precision. Therefore, magnitude matching was chosen for MRF-EPI in this study. As the correlation based pattern matching requires zero mean noise, a violation of this assumption potentially compromises the accuracy. However, due to sufficient base-line SNR, the detrimental effect can be expected to be small. Alternative reconstructions based on a Rician noise maximum likelihood estimation could be used to further mitigate this effect. However, the potential gain in accuracy comes at the cost of greatly increased computational time.

3.5 Conclusion

In the study we have proven the feasibility of a MRF sequence with spoiled EPI readout. Rapid T_1 and T_2^* quantification is performed within 10 seconds per slice and yields *in vivo* relaxation parameter maps of high quality. Using EPI for MRF fosters its usability and offers a complementary approach to existing MRF sequences.

Statement of Contribution

In this study I was responsible for the sequence programming, simulations, all data acquisition and analysis. Further, I did the literature research and wrote the manuscript.

“Time efficient whole-brain coverage with MR Fingerprinting using slice-interleaved echo-planar-imaging ”

Sci. Rep., doi:
10.1038/s41598-018-24920-z

4

4.1 Introduction

Quantification of tissue properties has long been an overarching goal in Magnetic Resonance Imaging (MRI) research, allowing for inter-patient and inter-scan comparability (Tofts, 2005). Recently, signal quantification has achieved major clinical impact in multiple fields of MRI (Baksi and Pennell, 2013; Bulluck et al., 2015; Feng et al., 2018; Radenkovic et al., 2017; Ross et al., 2013). Neurological applications of quantitative MRI have gained interest with the introduction of magnetic resonance fingerprinting (MRF) (Ma et al., 2013), due to the premise of fast simultaneous multi-parameter quantification. MRF is based on generating unique signal signatures, termed 'fingerprints', for different tissue types based on their underlying MRI properties. This is achieved by the rapid acquisition of numerous images with varying contrast weightings induced by the variation of sequence parameters including flip angle and echo time (TE). Matching these fingerprints to a precomputed dictionary allows parameter mapping of relaxation parameters including T_1 , T_2 and T_2^* (Jiang et al., 2015; Rieger et al., 2017b), tissue properties such as perfusion (Christen et al., 2014) and system parameters such as B_1^+ (Buonincontri et al., 2017). MRF has been used in clinical studies to evaluate the range and progression of MRF-derived relaxometry values in the brain as a function of the age of healthy volunteers (Badve et al., 2015). Recently, a study demonstrated that MRF can differentiate common types of adult brain tumors, providing initial evidence for its clinical utility (Badve et al., 2017). The original MRF method was based on a balanced steady state free precession (Ma et al., 2013) sequence design with highly undersampled spiral readout allowing for joint T_1 and T_2 mapping. Unbalanced fast imaging with steady state precession (FISP) (Assländer et al., 2017; Buonincontri and Sawiak, 2015; Jiang et al., 2017b, 2015) was subsequently introduced to overcome sensitivity to B_0 field inhomogeneities at the expense of reduced signal-to-noise ratio (SNR). Recently, we introduced an alternative MRF sequence for simultaneous T_1 and T_2^* mapping based on spoiled gradient echo imaging with Cartesian echo-planar imaging k-space readout (MRF-EPI) (Rieger et al., 2017b), potentially fostering robustness

towards gradient deviations and trajectory inaccuracies compared with unspoiled spiral readouts (Block and Frahm, 2005). While MRF has successfully enabled efficient multi-parameter quantification in a single-slice, its applicability with improved coverage has been limited. Conventionally, full magnetization relaxation needs to be ensured prior to the acquisition of the next slice in order to use the same signal model for each measurement. A recent study has proposed shortened relaxation intervals, maintaining similar quantification accuracy at the cost of compromised precision due to lower SNR in the baseline images (Amthor et al., 2017). Further, simultaneous multi-slice (SMS) imaging (Barth et al., 2016) has been incorporated into MRF (Jiang et al., 2017a; Ye et al., 2017) by creating time-varying phase modulation between the acquired slices, in order to alleviate the problem of confined coverage and to increase scan-time efficiency. While obtaining an acceleration factor up to 3, computationally complex kernel fitting is needed for complete slice separation and additional training data must be acquired prior to the measurement, increasing overall measurement time. Further, quantification precision is compromised due to overlapping coil-geometries in the SMS reconstruction (Ye et al., 2017). Most recently, 3D MRF methods were also proposed for improved spatial coverage (Liao et al., 2017; Ma et al., 2018). In these studies highly regularized image reconstructions (Ma et al., 2018) or repeated acquisition from the steady-state (Liao et al., 2017) were used to enable reconstruct of a continuous imaging volume from a 3D stack-of-spirals k-space. Slice-interleaved acquisition is a complimentary approach for volumetric imaging and clinical standard in numerous applications (Fautz et al., 2004), including diffusion MRI, fMRI and gradient echo sequences. Slice-interleaved schemes achieve similar SNR compared to 3D (Johnson et al., 1999) acquisitions, while allowing arbitrary slice spacing. Compared to single-slice imaging scan-efficiency is substantially improved due to increased effective TR, leading to higher SNR for each slice. However, the need for coherent signal-paths limits the effective TR in balanced sequence designs (Nielsen and Nayak, 2009), so far preventing the use of slice-interleaved acquisitions in MRF. In this study, we sought to increase scan-time efficiency of volumetric coverage in MRF parameter mapping by integrating a slice-interleaved acquisition scheme in MRF-EPI. Spoiled gradient echo readouts enable increased effective TRs, ultimately enabling whole-brain coverage in clinically acceptable scan-times. The number of interleaved slices is numerically optimized to provide a trade-off between scan-time and quantification precision. Phantom experiments are performed to validate quantification accuracy of joint T_1 , T_2^* and proton density (PD) mapping. *In vivo* images in healthy subjects and patients suffering from multiple sclerosis are obtained in order to study feasibility of whole-brain quantification for clinical usage and compare image quality to single-slice acquisitions.

4.2 Methods

4.2.1 Pulse sequence design

MRF-EPI (Rieger et al., 2017b) is modified to allow for slice-interleaved acquisition of multiple slices (Figure 4.1 a). Following a global inversion pulse, numerous single-slice EPI readout modules are acquired in rapid succession. The

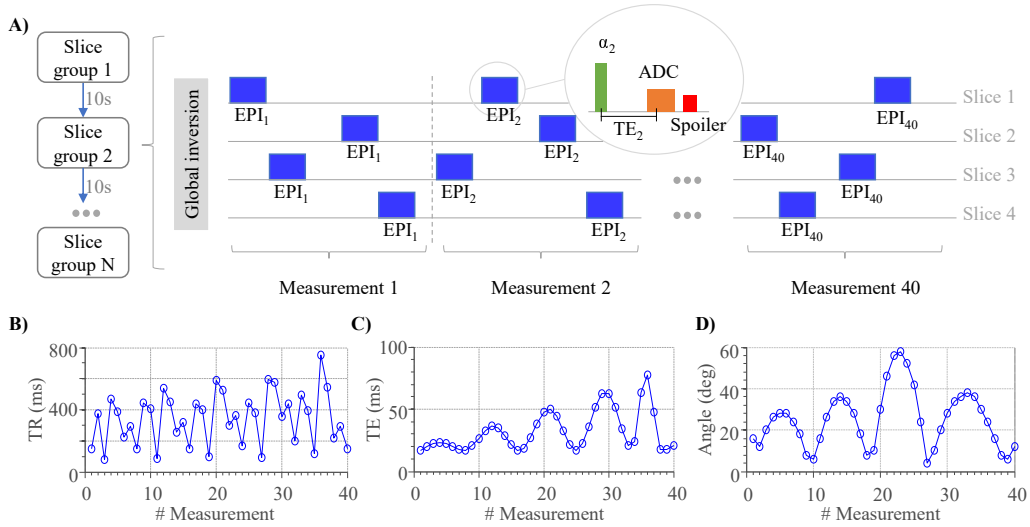


Figure 4.1: (A) Schematic diagram of the slice-interleaved MRF-EPI comprising multiple consecutive slice groups, each acquiring four slices with multiple EPI readouts; slice order is randomized within each measurement. Profiles of the repetition time (B) echo time (C) and flip angle variations (D) used for the proposed MRF measurements.

slice position is varied in a pseudo-random fashion. The randomization is performed block-wise for groups containing the acquisition of each slice once. Slice order within these groups is randomly permuted. This ensures that each slice is sufficiently sampled throughout the measurement, while creating pseudo-random signal traces. Especially in the initial stages of the acquisition this guarantees that the sampling frequency of each slice is similar during the early part of the inversion recovery, ensuring comparable sensitivity. The pseudo-randomization influences the effective slice-TR (Figure 4.1 b), which includes the acquisition time of the other slices, leading to higher signal dissimilarities of the resulting fingerprints. As shown in Figure 4.1 c-d, TE and flip-angles are also varied to obtain sensitive tissue fingerprints as previously proposed (Rieger et al., 2017b). Fat-suppression was included to minimize EPI imaging artefacts; gradient spoiling was incorporated by using crusher gradients of equal polarity performed before and after the fat-suppression pulse. For whole-brain coverage multiple interleaved slice-group acquisitions were performed, each simultaneously measuring four slices (Figure 4.1 a), separated by a 10 second pause to guarantee full magnetization recovery due to the global inversion pulse.

4.2.2 Dictionary

The dictionary was generated off-line using MATLAB (The MathWorks; Natick, MA) by simulating the evolution of the magnetization based on Bloch-equation simulations on a per-slice basis, as detailed by (Rieger et al., 2017b). B_1^+ compensation was integrated by simulating a scaling factor to the flip-angle excitation pulse (Buonincontri and Sawiak, 2015). Dictionary matching was performed by choosing the entry with the highest inner product between the magnitude of the dictionary entry and the magnitude of the measured signal. Due to the varying TR pattern of each slice within a slice group, a separate dictionary was pre-computed for each unique TR pattern. Each per-slice MRF dictionary consisted of

157,938 entries with the following parameter range: B_1^+ amplitude correction (Buonincontri and Sawiak, 2015) using a linear scaling factor in the range of 0.6-1.4 in steps of 0.1, $T_1 = 20$ -2000 ms in steps of 10 ms, and 2000-6000 ms in steps of 500ms; $T_2^* = 10$ -100 ms in steps of 2ms, and 100-300 ms in steps of 5 ms. Unrealistic entries with $T_1 < T_2^*$ were discarded.

4.2.3 Proton Density (PD) Mapping

Numerous factors influence the voxel intensity in an MRI measurement, and need to be accounted for when quantifying the tissue PD (Tofts, 2005). In the present sequence, relaxation induced signal changes are incorporated as T_1 and T_2^* in the dictionary model. Transmit radiofrequency field B_1^+ inhomogeneities are compensated using scaling of the effective flip-angle as described above. Semi-quantitative M_0 maps, can be calculated from the matching dictionary entry f and the measured signal k , using a least-square fit with the closed form solution of

$$M_0 = \frac{|k^T k|}{|k^T f|} \quad (4.1)$$

Here, the semi-quantitative M_0 is characterized as

$$M_0 = C \cdot \rho \cdot S, \quad (4.2)$$

depending on PD ρ , coil sensitivities S and a constant scaling factor C that includes spatial-invariant scaling such as receiver gain and DICOM export window-leveling. The coil sensitivity maps S were obtained with the method described by Volz et al., based on the idea, that the proton density map is a combination of the data set M_0 with full spatial resolution and a bias field comprising of low spatial frequencies (Volz et al., 2012). It was shown that the coil sensitivity S can be calculated with a probabilistic framework including optimised parameters (Ashburner and Friston, 2005), by which *in vivo* images are registered, segmented and bias-corrected. The model incorporates a smoothness intensity variation estimation termed field bias, which is proportional to S (Volz et al., 2012). The field bias map was calculated from the M_0 map using the segmentation toolbox of the SPM12 software package (<http://www.fil.ion.ucl.ac.uk/spm/>), using the default toolbox parameters: Regularization = 0.001, FWHM = 60 mm cutoff. To quantify ρ , C is calculated using cerebrospinal fluid (CSF) as a reference point, such that 100 percentage units (pu) corresponds to the known PD of 110.3 mol/l at 37° (Warntjes et al., 2007a). The scaling factor was determined by manually placing regions of interests (ROIs) in CSF and normalizing these areas to 100 pu.

4.2.4 Numerical Simulations

For a given scan-time the proposed sequence requires a trade-off between number of slices per slice group and number of baseline images per slice. However, an increased number of slices also increases the average effective slice TR, leading to higher baseline SNR. To determine the optimal number of slices for a given measurement time of 17 seconds per slice group, the stability of the parameter quantification from the MRF data was evaluated in dependence of the number

of baseline images by estimating the noise amplification in the linearized MRF system for T_1 and T_2^* parameters as described by (Rieger et al., 2017b). The average normalized noise amplification was calculated for fingerprints generated from 18 pairs of relaxation times in the *in vivo* range (T_1 : 1000-2500 ms T_2^* : 50-70 ms) for 1 to 160 baseline images, each. The TE and flip angle patterns were interpolated according to the number of measurements and TR was maximized to reach a measurement time of 17 seconds.

To verify the analysis based on linearization, Monte-Carlo simulations were performed to determine the quantification accuracy. The same set of fingerprints, TE, TR and flip angles patterns were used as in the noise amplification simulation. Noise was added ($n = 1000$) to the simulated patterns and matched with the dictionary. The mean normalized quantification accuracy was calculated depending on the number of baseline images.

The randomization of the slice order was performed to achieve more homogenous quantification characterization across the slices, as compared with sequential order. Numerical simulations comparing the quantification precision between these slice ordering schemes are provided in Supplementary Information.

4.2.5 Acquisition

To test the performance of the sequence, phantom and *in vivo* data were acquired on a 3 T whole-body scanner (Magnetom Trio; Siemens Healthcare, Erlangen, Germany) using a standard 32-channel head array coil for *in vivo* measurements and 30-channels of a body and spine array for phantom scans. This study was approved by the local institutional review board (Institutional Review Board II, Medical Faculty Mannheim, Germany), all subjects provided written informed consent prior to examination and all methods were performed in accordance with the relevant guidelines and regulations. For the proposed slice-interleaved MRF acquisition, following parameters were used: 4 slices per slice group, TE/TR = 17-78 ms/80-755 ms, flip angle = 4-58°, FOV = 220×220×140 mm³, slice-gap = 0.9 mm, voxel size = 1.0×1.0×3.0 mm³, band-width = 1136 Hz/pixel, partial-Fourier = 5/8, parallel imaging factor 3 with GRAPPA reconstruction, reference lines = 48 acquired in-place for each baseline image, acquisition time per slice group = 17 s, total number of baseline images = 160 (4 slices with 40 images each). The single-slice MRF-EPI used the same parameters, though only acquiring one slice with 160 baseline images and an acquisition time per slice = 17 s.

4.2.6 Phantom Experiments

The accuracy and precision of the sequence were evaluated in phantom experiments and compared to reference measurements, inversion recovery turbo spin echo for T_1 (IR-TSE, 6 images, TI = 50-4000 ms, TE/TR = 6 ms/15 s, turbo factor = 16, matrix/FOV = 64×128/110×220 mm², slice thickness = 3 mm, BW = 399 Hz/pixel, scan-time = 4 min 30 s, two-parameter fit) and spoiled gradient echo for T_2^* (GRE, 6 images, TE = 5-300 ms, TR = 1000 ms, alpha = 15°, matrix/FOV = 64×128/110×220 mm², slice thickness = 3 mm, BW = 390 Hz/pixel, scan-time = 6 min 18 s, three parameter fit). Each phantom was acquired 10 times in separate

measurements with the slice-interleaved MRF-EPI and single-slice MRF-EPI. Reference measurements were acquired once per phantom. The nine phantoms consisted of a single gadoterate-meglumine (Dotarem; Guerbet, Villepinte, France, concentration: 0.075-0.15 $\mu\text{mol/ml}$) doped agarose compartments each (concentration: 0.5-1.5 %). The mean relaxation times were determined by manually drawing ROIs in the phantoms. The accuracy of the slice-interleaved MRF-EPI was determined by comparing the average deviation and the normalized root-mean-square error (NRMSE) between the method and the reference measurements. A two sample Student's t-test was used to conclude if the single-slice and slice-interleaved MRF-EPI have significantly different means. P values less than 0.05 were considered to be significant.

Consistency within a slice group was tested to study quantification differences among the slices caused by different acquisition parameters. For each phantom four separate measurements (A, B, C, D) were performed with the slice-interleaved MRF sequence, each acquiring four slices (A_1, \dots, A_4 , and B_1, \dots, B_4 , ...). The slice group location was shifted among the four measurements in such a way that the center of the phantom was covered by a different one of the four slices in each measurement (i.e. the center of the phantom was covered by A_1 , B_2 , C_3 and D_4). Consistency among the four slices was defined as the difference between the measurement in A_1 , B_2 , C_3 and D_4 , using the same manually drawn ROI.

PD mapping was evaluated in a phantom consisting of gadoterate-meglumine doped water. Reference PD maps were acquired using multiple GRE images with long TR to avoid T_1 weighting, and varying echo-time to compensate for T_2^* decay (GRE, 5 images, TE = 3-60 ms, TR = 1500 ms, alpha = 90° , matrix/FOV = $64 \times 64 / 220 \times 220$ mm², BW = 390 Hz/pixel, scan-time = 7 min 50s, three parameter fit). Imaging was performed with the body coil, which was used both for transmit and receive. B_1^+ maps were acquired using a double-angle method (GRE, 2 images, TE = 10 ms, TR = 1500 ms, alpha = $45^\circ/90^\circ$). Given the reciprocity assumption, as transmit and receive were performed with the same body coil, B_1^+ maps were also used for receive coil profile correction. Accordingly, PD maps were calculated with $\rho = C \cdot I \cdot B_1^+ \cdot S / e^{-TE/T_2^*}$. The reference and slice-interleaved measurements were performed with a slice thickness of 10 mm with varying amounts of water and air within the slice, thus changing the PD depending on the water-air ratio. PD values of the slice-interleaved EPI and the reference measurements were compared by placing ROIs within the PD maps and acquiring average values in each. The constant scaling factor was chosen such that 100 % water is normalized to 100 pu in manually drawn ROIs in a full water compartment. The B_1^+ maps acquired using a double-angle method were also used in the correction of the MRF-EPI PD instead of bias field correction, as the latter probabilistic method is known to be unsuitable for phantom measurements (Volz et al., 2012).

4.2.7 *In vivo* experiments

Whole-brain *in vivo* MRF quantifications were acquired with the proposed method in 6 healthy volunteers (4 men, 31 ± 6 years old) and 4 multiple sclerosis (MS) patients (2 men, 42 ± 5 years old). T_1 , T_2^* and PD values were obtained for white matter and grey matter by segmenting a slice of each healthy volunteer with

the segmentation toolbox of SPM12. To avoid partial voluming effects in small structures, the masks were eroded with MATLAB image erosion algorithm (disk radius = 1 pixel). T_1 , T_2^* and PD for MS patients were determined by manually placing ROIs in the lesions, as identified on separate clinical measurements.

4.3 Results

4.3.1 Numerical Simulations

Figure 4.2 a shows the average noise amplification in the parameter recovery from MRF data as a function of the number of baseline images. The combined average noise amplification of T_1 and T_2^* (thick blue curve) has a similar amplitude for 40 to 160 baseline images. The noise amplification increases rapidly, when reducing the number of images below 40. The separate T_1 and T_2^* curves have different characteristics, while the T_2^* noise amplification is lowest with 29 baseline images, it increases slightly with more images, implying that for T_2^* quantification fewer higher SNR baseline images have higher noise resilience than many low SNR images. T_1 has lowest noise amplification with a high number of baseline images with a slight increase until 20 baseline images. For less than 20 images, the amplification is rapidly rising, as a too low number of baseline images causes the inversion recovery curve to be sampled sparsely, decreasing noise resilience. Figure 4.2 b shows the normalized quantification precision in the Monte-Carlo simulations as a function of the number of baseline images. The results show the same characteristics as the noise amplification using the linearized system (Figure 4.2 a) with similar average precision for 40 to 160 baseline images. Reducing the number of baseline images increases the effective TR, thereby enabling the acquisition of other slices during these pauses. As the average noise amplification has a similar value for the baseline images between 40 and 160, acquiring 4 slices for each slice group in the proposed acquisition results in the highest acceleration factor with only marginal loss of precision.

4.3.2 Phantom Experiments

Figure 4.3 a shows the T_1 and T_2^* maps of the phantom experiments using MRF-EPI and reference measurements. The proposed method yields homogeneous T_1 estimates within the phantoms. T_2^* maps show a higher degree of variation than T_1 maps, due to magnetic susceptibilities and large field inhomogeneities influencing the T_2^* values, both in the reference and MRF measurements. Figure 4.3 b depicts the T_1 , T_2^* and PD quantification using the slice-interleaved MRF-EPI as compared to the reference method. Proposed MRF-EPI shows slight underestimation of T_1 (deviation: -2.4 ± 1.1 % [min: -4.5 %, max -0.8 %], NRMSE: 3.0 %), T_2^* (-0.5 ± 1.5 % [min: -2.7 %, max 1.6 %], NRMSE: 1.5 %) and PD (-0.5 ± 7.2 pu [min: -11.6 pu, max 6.3 pu], NRMSE: 6.5 %) values compared to the reference measurements.

The Bland-Altman plots in Figure 4.3 c compare the quantification accuracy of the single-slice MRF-EPI to the slice-interleaved MRF-EPI for T_1 and T_2^* . As originally introduced (Rieger et al., 2017b) no PD mapping was performed with the single-slice MRF-EPI. No significant difference was found between the single

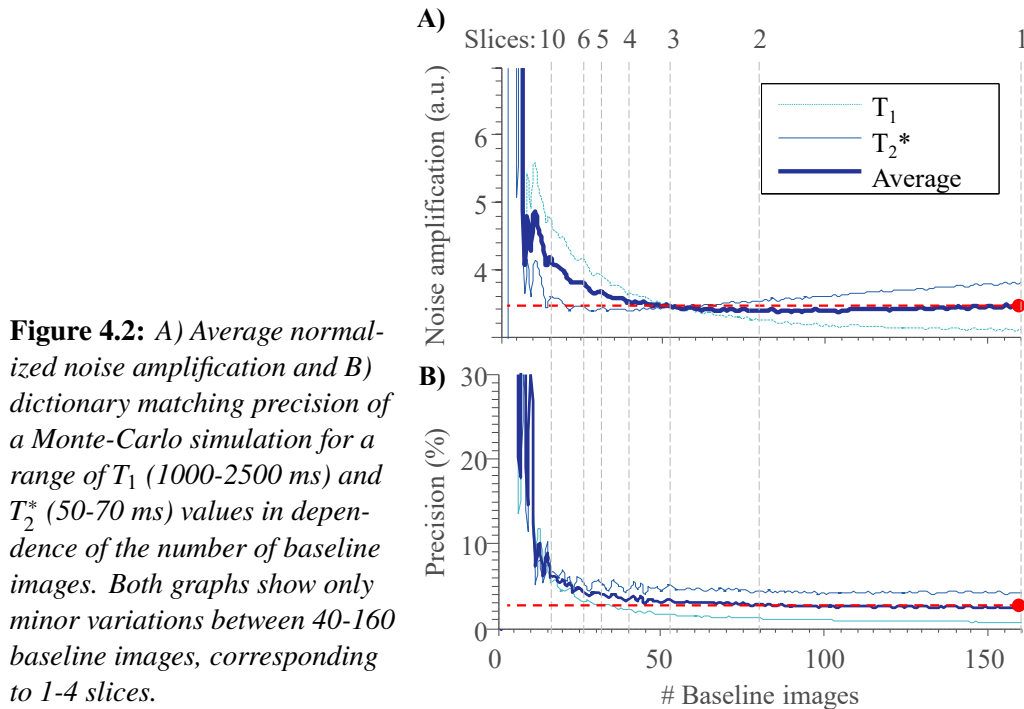


Figure 4.2: A) Average normalized noise amplification and B) dictionary matching precision of a Monte-Carlo simulation for a range of T_1 (1000-2500 ms) and T_2^* (50-70 ms) values in dependence of the number of baseline images. Both graphs show only minor variations between 40-160 baseline images, corresponding to 1-4 slices.

and slice-interleaved MRF ($p \leq 0.05$). The slice-interleaved implementation results on average in slightly higher values for T_1 (24 ± 9 ms [min: 12 ms, max: 38 ms]) and T_2^* (2 ± 1 ms [min: 0 ms, max: 3 ms]) maps.

Precision and accuracy were not affected by different TR patterns among the 4 slices within a slice group, resulting in a deviation of less than 1 % for all parameters when quantifying the exact same slice location in a phantom as a test for inter-slice consistency.

4.3.3 *In vivo* Experiments

Full brain MRF data with 32 slices was successfully acquired in all healthy volunteers and patients. Figure 4.4 shows representative T_1 , T_2^* and PD maps from a healthy volunteer. The mean $T_1/T_2^*/PD$ values of all healthy volunteers of an exemplary slice are: white matter: 746 ± 57 ms/ 57 ± 6 ms/ 72 ± 7 pu, grey matter 1200 ± 100 ms/ 53 ± 6 ms/ 92 ± 18 pu. While T_2 values are generally higher in grey than white matter, similar values for T_2^* in grey and white matter are obtained. This is well in line with previous studies and attributed mostly to magnetic susceptibility (Wansapura et al., 1999).

4.3.4 *In vivo* Experiments

Figure 4.5 shows two example slices of a healthy volunteer acquired with the slice-interleaved and single-slice MRF-EPI. Both methods yield visually comparable T_1 and T_2^* maps. The volunteer has intracranial calcifications in the frontal lobe of the brain (white arrow), leading to signal dropouts in the region in T_1 as well as T_2^* maps, which is visible in both methods. Results from a patient scan are depicted in Figure 4.6 (female, 40 years). The lesion of the MS-patient is clearly visible in T_1 , T_2^* and PD maps (Figure 4.6 a, further images in Supplementary Figure 4.8). Exemplary T_1 , T_2^* and PD values (of lesions from three MS patients

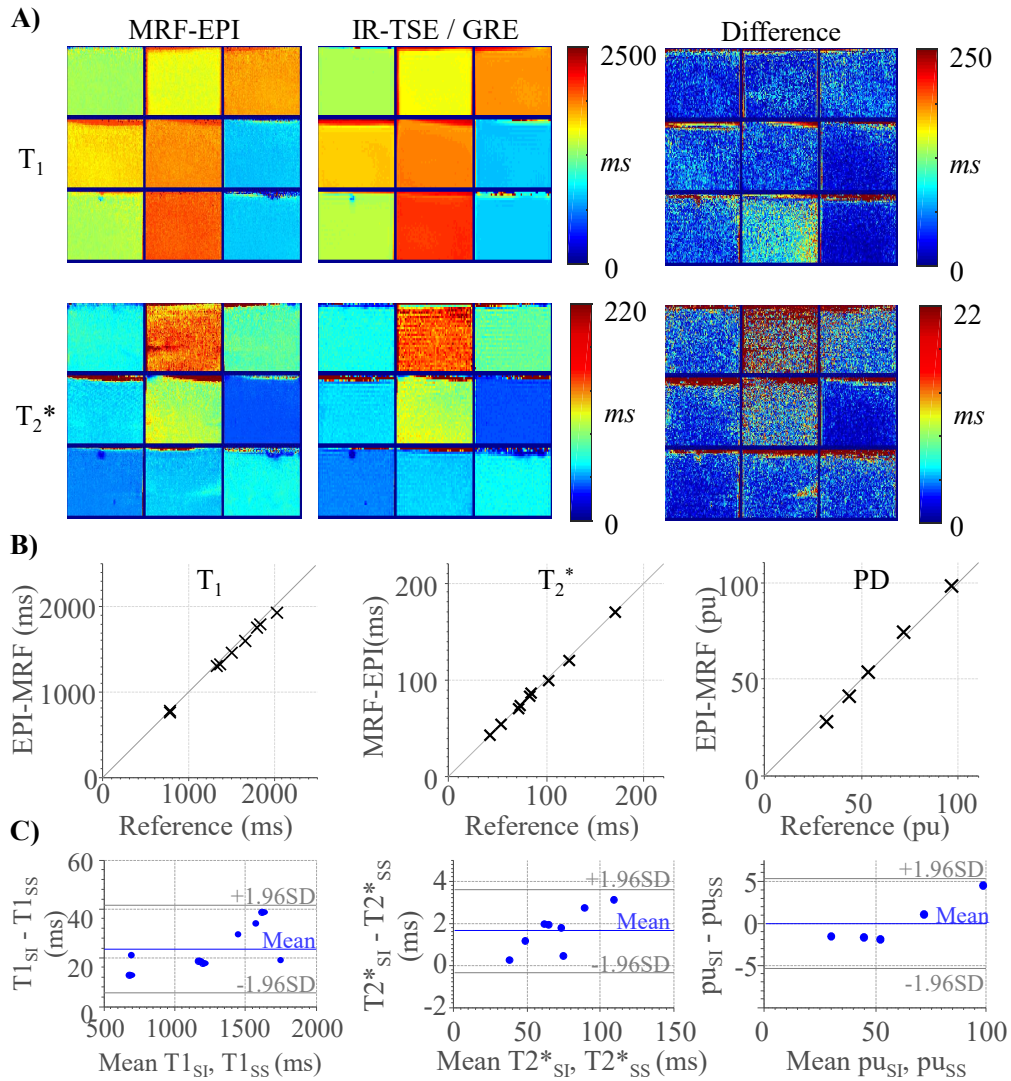


Figure 4.3: (A) T_1 and T_2^* maps obtained in phantom measurements using slice-interleaved MRF-EPI and the respective reference method IR-TSE and GRE. (B) Comparison of T_1 , T_2^* and proton density (PD) values of slice-interleaved MRF-EPI with the reference methods showing nearly identical average quantification in all phantoms. (C) Bland-Altman plot showing good agreement between the slice-interleaved MRF-EPI (T_{1SI} , T_{2SI}) and the single-slice MRF-EPI (T_{1SS} , T_{2SS}).

are higher compared to surrounding tissue (1285 ± 200 ms/ 95 ± 17 ms/ 62 ± 0 pu, 1528 ± 11 ms/ 121 ± 21 ms/ 62 ± 0 pu, 1270 ± 66 ms/ 81 ± 12 ms/ 60 ± 0 pu), allowing clear quantitative discrimination especially in the T_2^* maps. Sample fingerprints of the MS patient retrieved from manually placed ROIs in grey matter, white matter and a lesion display clearly differentiable signal paths (Figure 4.6 b). The same trend and good differentiability is observed across all subjects, despite minor subject specific variations.

4.4 Discussion

In this work, we integrated slice-interleaved scanning in the MRF-EPI method to increase scan-time efficiency, enabling quantification with increased volumetric

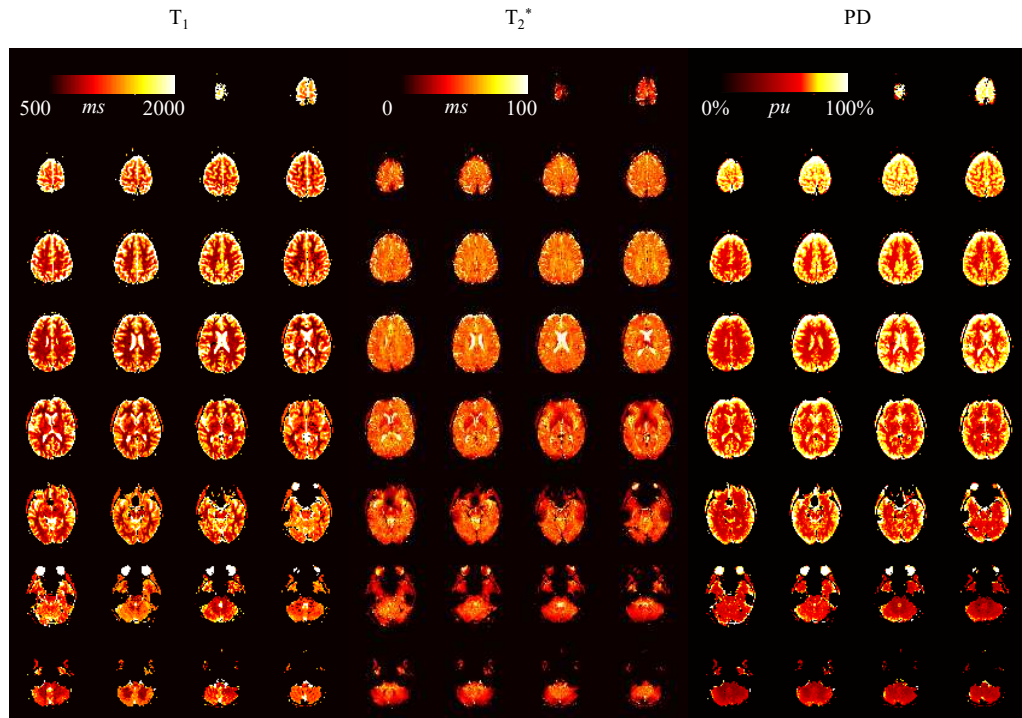


Figure 4.4: T_1 , T_2^* and proton density maps acquired with slice-interleaved MRF-EPI, 32 slices with a resolution of $1 \times 1 \times 3$ mm were measured within a total measurement time of 3:36 minutes.

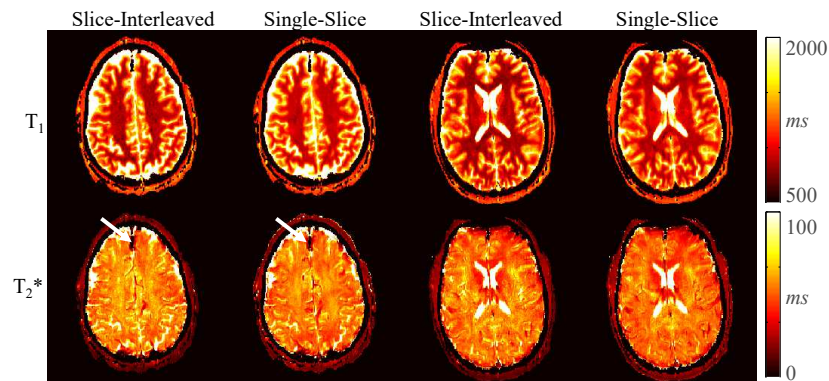


Figure 4.5: Exemplary *in vivo* T_1 and T_2^* maps acquired in one subject with slice-interleaved and single-slice MRF-EPI. Both techniques achieve visually comparable image quality, with good white/grey matter delineation in the T_1 maps and susceptibility contrast weighting in the T_2^* maps. Intracranial calcification is clearly depicted by signal dropout in the T_2^* map of both sequences (white arrow).

coverage with an acceleration factor of 4 compared to single-slice MRF. Acquisition of slice groups with four slices provided high quantification accuracy in phantom experiments, comparable to the single-slice implementation and in agreement with reference measurements. Whole-brain *in vivo* scans with 32 slices were acquired within 3:36 minutes in multiple volunteers, resulting in robust and artefact-free T_1 , T_2^* and PD parameter maps.

In comparison to the original MRF-EPI with 160 baseline images, a reduced number of 40 baseline images were acquired per slice. Our numerical simulations of noise amplification and phantom experiments showed that a reduced

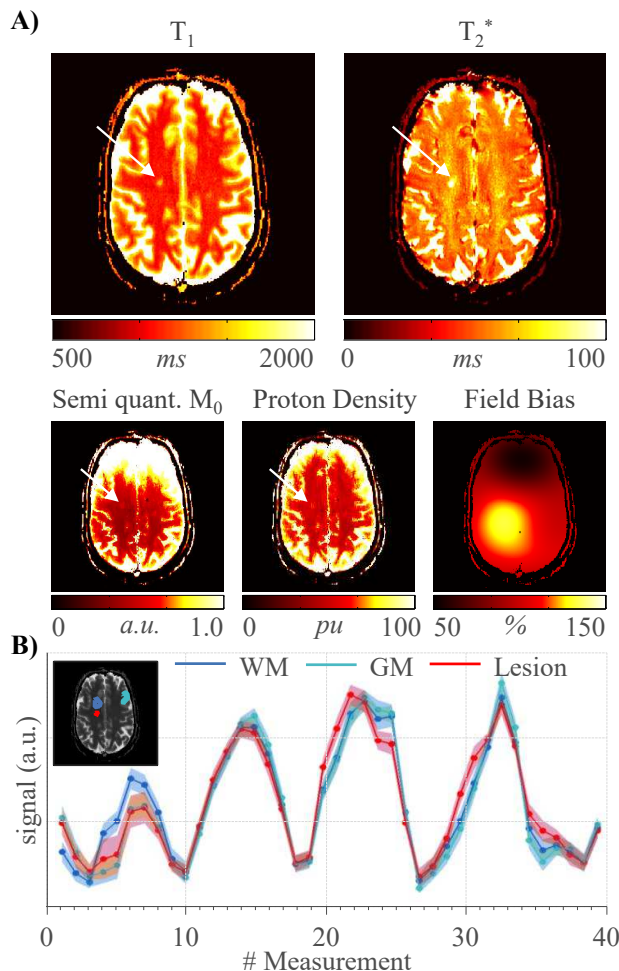


Figure 4.6: (A) T_1 , T_2^* , semi quantitative M_0 , corrected proton density and field bias map of an MS patient with clearly visible lesions (white arrow), (B) Exemplary fingerprints from manually drawn ROIs in grey matter (GM), white matter (WM) and a lesion.

number of baseline images with longer TR and therefore higher SNR can lead to comparable quantification precision compared with a high number of low SNR baseline images. The results indicate that by reducing the number of baseline images while increasing TR, T_2^* accuracy is enhanced due to the higher SNR images. T_1 accuracy declines slightly, as less data is acquired during the inversion recovery period at the start of the measurement. Our simulations indicate that acquiring four interleaved slices sharing a global inversion pulse leads to the highest scan-time efficiency gain for values in the *in vivo* range, without compromising accuracy. The T_1 precision could possibly be improved by including further inversion pulses during the acquisition of the slices, facilitating even higher acceleration. Alternative sequence designs incorporating this idea warrant investigation in future studies.

Simultaneous multi-slice imaging has recently received increasing interest, including quantitative applications (Setsompop et al., 2012; Weingärtner et al., 2017), as it provides means for scan-time acceleration where the only loss in SNR is due to coil geometries. SMS has recently been applied to trueFISP-based MRF in two studies (Ye et al., 2017, 2015). While gaining a 3-fold acceleration, higher factors are currently limited by noise amplification and signal leaking. Further, the sequence needs to acquire additional training data per slice and the computationally intensive regridding algorithms pose a challenge, while the quantification precision is compromised. Combining SMS with EPI by applying a cyclic phase-shift among the k-space lines allows for an intuitive interpretation

of the CAIPIRINHA approach as FOV shifts induced in separate bands. SMS-EPI is commercially available from a major vendor and is successfully integrated into several clinical and large scale cohort studies with previously reported acceleration rate of up to 16 (Moeller et al., 2010). Therefore, the combination of SMS with the proposed slice-interleaved scheme bears great promise for ultra-rapid whole-brain quantification of multiple parameters.

Several methods have been recently proposed to shorten reconstruction times by altering the process of dictionary matching (Cauley et al., 2015; McGivney et al., 2014; Yang et al., 2018). These can be readily incorporated in the quantification step of the proposed method, replacing conventional dictionary matching, in order to speed up post-processing. However, due to a lower number of baseline images, reconstruction times are typically less of a concern, as compared with other MRF methods. In the proposed scheme, as well as in other MRF techniques, spatial resolution is limited by the readout duration per image. Advanced undersampling and reconstruction or denoising techniques have been recently proposed in the context of MRF (Assländer et al., 2018; Doneva et al., 2017; Liao et al., 2016; Pierre et al., 2016; Wang et al., 2016; Yang et al., 2018; Zhao et al., 2018, 2016) to facilitate increased undersampling rates or to improve noise performance, by exploiting structure or inter-dependencies mainly along the temporal dimension. As these approaches are applicable to a variety of sampling schemes or have specifically been demonstrated for EPI (Davies et al., 2014), they are fully compatible with the proposed slice-interleaved MRF method. Due to the increased baseline SNR in the proposed approach, these reconstruction methods promise large gains in the feasible undersampling factor at minor loss in quantification quality. This may ultimately facilitate high-resolution quantification without scan-time penalty and warrants investigation in future studies.

Volumetric MRF sequences based on highly undersampled stack of spirals trajectories have demonstrated the feasibility of whole-brain quantitative T_1 and T_2 imaging. (Liao et al., 2017) minimized scan time by including Cartesian GRAPPA with a factor of 3 in kz direction and simultaneously reducing the baseline images to 420 per slice, compared to 1000 in the original MRF-FISP sequence. However, to allow for sufficient k-space data to reconstruct a 3D volume per imaging contrast, repeated acquisitions of the signal train are performed from a steady-state. This enabled whole-brain quantification with 1 mm isotropic resolution within 7.5 min, although with extensive reconstruction complexity amounting to 20 h computation time. (Ma et al., 2018) used an interleaved sampling pattern, acquiring 4 interleaved slices per group and sequentially measuring multiple groups, while also reducing the number of baseline images per slice to 480 to decrease scan time. Further, the relaxation time between the slice groups was set to 3 seconds to reduce scan time, therefore preventing full relaxation before the acquisition of the next slice group, as previously proposed (Amthor et al., 2017). Within 5 min T_1 and T_2 maps of 48 slices with a resolution of $1.2 \times 1.2 \times 3.0 \text{ mm}^3$ were acquired, though an additional B_1 measurement was needed to correct for B_1 inhomogeneity effects and improve the accuracy of T_1 and T_2 estimates. To achieve reconstruction of an imaging volume without the need for repeated acquisitions per contrast, image regularization was integrated with a sliding window reconstruction across multiple images. Several recent works have enabled 3D EPI or echo volumar imaging (EVI), based on highly, accelerated imaging Cartesian readouts (Afacan et al., 2012; Posse et al., 2013).

Readout-times could be further shortened by exploiting dependencies between the acquisition of multiple images (Afacan et al., 2012), or by employing image regularization (Jung et al., 2009). These methods offer interesting potential to enable the acquisition of multiple interleaved 3D volumes in the proposed sequence scheme, similar to the method of Ma et al. The combination of slice-interleaving and volumetric coverage allows to synergistically benefit of the SNR gain of both methods and will be subject of future studies.

Slice-interleaved 2D and 3D acquisitions are complimentary techniques for volumetric coverage, each offering a distinct profile of advantages. The SNR gain is reported to be very similar in many practical applications (Johnson et al., 1999). Comparing the proposed slice-interleaved MRF-EPI to a hypothetical 3D acquisition with varying coverage but constant scan time, the 3D acquisition would achieve constant SNR, due to $\text{SNR} \sim d_x d_y d_z \sqrt{T_{acq}}$ (Glover, 2005). For 1 to 4 slices, no drawback in terms of SNR is observed for the slice-interleaved implementation as shown by the simulations (Figure 4.2). Hence, in this regime the slice-interleaved MRF-EPI provides comparable to SNR to an idealized 3D implementation. While 3D sequences commonly allow for lower minimal slice thickness and improved slice profiles, they often result in higher undersampling of the k-space and might require more elaborate reconstructions schemes, while conventional reconstructions are applicable to the proposed scheme. Further, 3D sequences are limited to the acquisition of a continuous volume. Multislice 2D allow for arbitrary slice spacing, enabling time efficient coverage of larger volumes without compromising resolution, by using slice gaps. Thus slice-interleaved acquisitions are often preferred in clinical applications, including scout and overview scans, which have the highest demand in terms of volumetric coverage.

In the present sequence, relaxation periods are required between different slice-groups due to the application of a non-selective adiabatic inversion-pulse. This can be circumvented by the application of slice-selective inversion. However, this requires a multi-band inversion pulse covering all spatially separated slices within the slice group and introduces substantial contrast weighting on the B_1^+ profile of the inversion-pulse. B_1^+ correction of the inversion similar to the one in proposed by (Buonincontri and Sawiak, 2015) can be integrated, and warrants further studies. Recently, it was shown that the relaxation periods can be significantly shortened between MRF pulse train repetitions by starting the repetition using a non-relaxed initial spin state (Buonincontri and Sawiak, 2015). While quantification accuracy is maintained, increased computational complexity is needed as the shortened relaxation times must be accounted for within the Bloch simulations. This approach might be used in combination with slice-interleaved MRF in future studies to minimize wait times and reduce acquisition time, at the cost of reduced precision due to lower baseline SNR.

Integrating B_1^+ compensation in MRF has been shown to improve quantification precision. This has been done by either using a Bloch-Siegert reference scan prior to the MRF measurement (Ma et al., 2017) or by integration a scaling factor to the flip-angle excitation pulse in the dictionary simulation. As previously evaluated in MRF-EPI, the latter method was chosen as to increase quantification accuracy in the presence of imperfect excitation slice profiles and inhomogeneities in the transmit field without the need for additional scan time. However, this scheme assumes a single flip-angle representative of the slice-

profile. This has been shown to be a valid approximation for small flip-angles in steady-state conditions (Weingärtner et al., 2015). To further overcome residual inaccuracies which might be observed with high flip-angles or pseudo-random acquisitions, actual slice-profile simulations can also be integrated in the dictionary, albeit at increased computational complexity.

The present slice-interleaved implementation has a similar computational complexity for the dictionary matching process to the single-slice MRF-EPI. On the one hand, four dictionaries need to be calculated, as each slice in a slice group has a unique TR pattern, while on the other hand the dictionary size per slice is reduced. Including slice-interleaved acquisitions in MRF favors a non-balanced spoiled sequence design, as the acquisition of interleaved slices hereby does not affect the signal paths of the other slices. MRF methods based on a balanced sequence design require coherent signal-paths limiting the effective TR, prohibiting the application in slice-interleaving without major adaptation.

PD mapping has a number of clinical applications, including multiple sclerosis (Laule et al., 2004) and brain tumors (Neeb et al., 2006). However, PD mapping is challenging, as traditionally a number of separate measurements need to be performed to compensate for contrast induced intensity variation. These variations include relaxation processes, inhomogeneous transmit and receive fields, as well as potentially other contrast mechanisms (Tofts, 2005). MRF has been proposed as a promising method for fast, joint quantification of a number of parameters. Previous studies have included a first-step towards MRF PD mapping by providing semi-quantitative M_0 maps (Ma et al., 2013). However, to achieve PD quantification additional bias correction for B_1^+ and coil sensitivity maps is required. Furthermore, in a balanced sequence design as previously proposed the M_0 measurement is confounded by residual contrast sensitivity towards molecular diffusion (Buxton, 1993) and magnetization-transfer (Gloor et al., 2008), potentially necessitating further corrections to obtain reliable PD maps. Due to the spoiled gradient echo contrast in MRF-EPI all necessary bias corrections can be performed in a two-step process without the need of additional measurements. A B_1^+ correction scheme was suggested by (Buonincontri and Sawiak, 2015), including flip angle correction in the dictionary matching process, which has been integrated in MRF-EPI (Rieger et al., 2017b). Coil sensitivity correction can be performed by calculating the field bias maps (Volz et al., 2012) based on a probabilistic per-image framework (Ashburner and Friston, 2005). The bias field maps have been shown to have a high *in vivo* accuracy compared to separately measured coil sensitivity maps (Weiskopf et al., 2011). As spoiled gradient-echo imaging is commonly not associated to other contrast sensitivities, the proposed approach compensates for the portfolio of confounders commonly considered in previous PD mapping studies (Volz et al., 2012). However, residual inaccuracies can be induced by deviations from the assumed signal model, including non-monoexponential transverse signal decay, as previously reported for complex tissue structures such as lung alveolus (Zapp et al., 2017).

Patient motion is one of the main causes of artefacts in clinical MRI. While MRF has been shown to be partially resilient to certain kinds of patient movement, initial results demonstrate that generic motion can induce significant intra-image variance to the MRF signal trace, resulting in motion artefacts in parameter maps (Cruz et al., 2017; Mehta et al., 2017; Rieger et al., 2017a). This effect can be exacerbated if increased scan time is necessary for volumetric coverage. In the

proposed scheme, the total duration between first and last data acquisition for any given slice, is comparable to previously proposed single slice sequences. Hence, the sensitivity to patient motion can be expected to be comparable to other MRF techniques. Furthermore, MRF seems well suited for correction of residual in-plane motion using co-registration of the baseline data, due to the rapid image acquisition. Motion correction schemes that are insensitive to contrast variation among the baseline images have been previously proposed (Roujol et al., 2015; Xue et al., 2012). Hence, further mitigation of in-plane motion effects using contrast invariant motion correction of the baseline images prior to dictionary matching warrants future investigation.

While the proposed method is used for joint T_1 and T_2^* quantification, it could be extended for T_1 and T_2 quantification by incorporating refocusing pulses prior to the readout. This is commonly performed in multiple applications of EPI (Tyler et al., 2004), benefiting from increased SNR at the expense of increased minimal TE and longer scan times. However, this would also allow for an integrated assessment of diffusion biomarkers by including randomized diffusion gradients. Extending the portfolio of simultaneous quantification of biomarkers with the proposed method is subject of further research, and may facilitate the usage of these methods for a wider range of diseases

The study and the proposed method have limitations regarding comparability with other methods and the number of patients. The proposed method uses the same TE and flip angle scheme as the single-slice MRF-EPI method, subsampled by a factor of four. To further increase accuracy or accelerate the sequence, optimization of sequence parameters may be necessary, which will be subject of further research. Due to the lack of the original MRF sequence at our center, no direct comparison could be performed regarding accuracy and precision. Further, in this study only a small number of subjects were scanned to prove the *in vivo* feasibility. Larger cohorts with specific diseases remain to be evaluated.

4.5 Conclusion

In the study, we have demonstrated the feasibility to accelerate the MRF-EPI for volumetric coverage by a factor of four while maintaining quantification accuracy using a slice-interleaved acquisition scheme. Within 17 seconds four slices with a resolution of $1 \times 1 \times 3 \text{ mm}^3$ are acquired, resulting in artefact free T_1 , T_2^* and PD maps.

4.6 Supplementary Information

4.6.1 Materials and Methods

The quantification precision of the randomized slice acquisition scheme was compared against a sequential acquisition scheme. For this purpose, a variety of noisy fingerprints ($T_1 = 100\text{-}6000 \text{ ms}$, $T_2^* = 10\text{-}100 \text{ ms}$) were simulated based on the Bloch-equations on a per-slice basis with $\text{SNR} = 90$ (compared to thermal equilibrium). T_1 and T_2^* were quantified from the noisy fingerprints using dictionary matching. Monte-Carlo simulation ($n = 1000$ iterations) were used to

measure quantification precision, defined as the standard deviation of the quantified value across the different iterations for each slice separately. The fingerprints were simulated with following parameters: TE = 17-78 ms, TR = 80-755 ms, flip angle = 4-58°. While for the sequential scheme the TR was constant within each slice-group, the randomized sequence scheme yields TR variation as shown in Figure 4.1 b. The mean and standard-deviation across the four slices was compared between the two slice schemes.

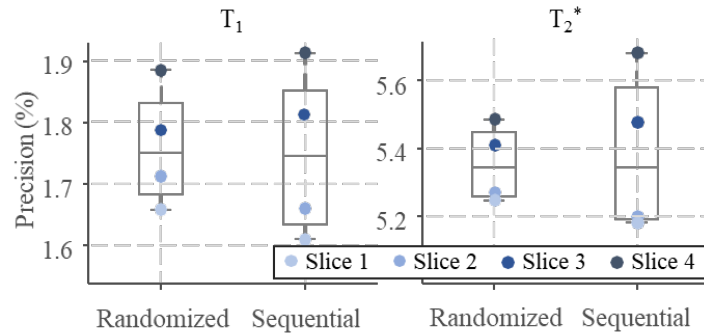


Figure 4.7: Quantification precision of a Monte-Carlo simulation for a range of fingerprints of the randomized and sequential slice shift scheme. Improved homogeneity of the precision across the slices, as represented by smaller standard deviation, is achieved with the randomized scheme.

4.6.2 Results

The quantification accuracy of the randomized and sequential acquisition schemes were virtually identical (Randomization / Sequential: T_1 0.07 ± 1.77 %/ 0.07 ± 1.76 % T_2^* : 1.37 ± 5.35 %/ 1.37 ± 5.39 % mean \pm std across slices). However, quantification precision was more homogenous across slices with the randomized acquisition scheme resulting in lower standard-deviation across the slices compared with the sequential acquisition scheme (Randomization / Sequential: T_1 1.77 ± 0.09 %/ 1.76 ± 0.14 % T_2^* : 5.35 ± 0.13 %/ 5.39 ± 0.23 % mean \pm std across slices) This indicates, that randomizing the slice order during acquisition leads to improved consistency of the quantification precision within a slice group.

Statement of Contribution

In this study I was responsible for the sequence programming, simulations, partially for the data acquisition and all data analysis. Further, I did the literature research and wrote the manuscript.

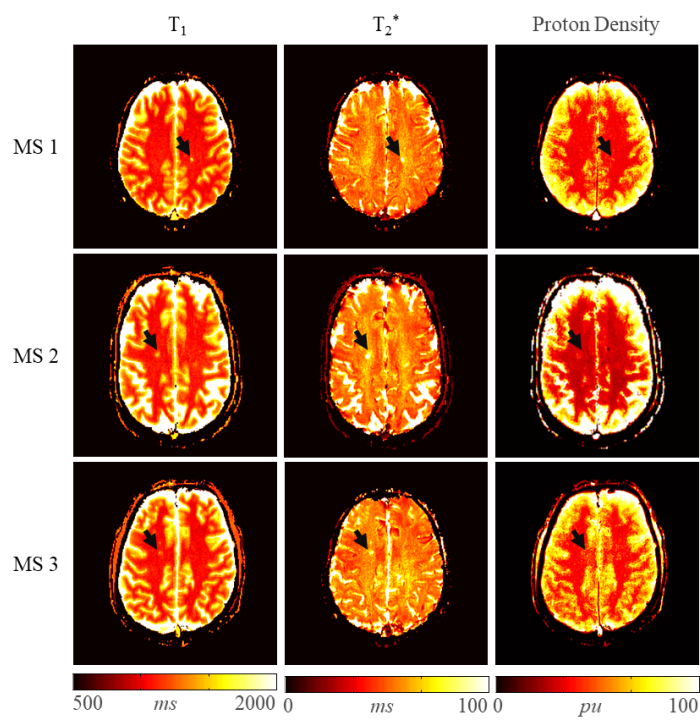


Figure 4.8: T_1 , T_2^* and corrected proton density map of three MS patients with clearly visible lesions (black arrows).

“Improved motion robustness for
EPI-based MR Fingerprinting using
intensity based image registration” *Sci.*
Rep., submitted

5

5.1 Introduction

Quantification of physical tissue properties such as the relaxation times T_1 , T_2 and T_2^* has been a long-standing goal in MRI research (Bottomley et al., 1987; Deoni, 2010; Radenkovic et al., 2017). While fast quantification methods have been proposed (Cohen and Polimeni, 2018; Heule et al., 2018; Sumpf et al., 2014), the scan times of these sequences is nonetheless far beyond qualitative imaging methods, prohibiting the wide spread use of quantification in clinical routine. Magnetic resonance fingerprinting (MRF) has recently reinforced the interest in quantitative MRI due the premise of fast multiparameter quantification (Assländer et al., 2017; Jiang et al., 2015; Ma et al., 2013; Rieger et al., 2017b). The underlying idea of MRF is to obtain a series of rapidly acquired baseline images, while inducing contrast variation by using pseudo randomized sequence parameters such as flip angles and echo times (TE). This generates a characteristic signal trace dependent on underlying physical parameters of the tissue and allows for parameter mapping by matching this signal evolution to a precomputed dictionary.

Patient motion is one of the most dominant confounders in clinical MRI, frequently leading to non-diagnostic image quality and increased measurement time due to the necessity of scan repetition. A recent study has shown that 20% of all clinical acquisitions needed to be repeated due to patient motion in one randomly selected full calendar week of MRI examinations (Andre et al., 2015). Particularly quantitative MRI sequences are prone to be corrupted by patient motion due to the long scan times. The intrinsic design of MRF, having a high number of rapidly acquired baseline images per measurements, offers a beneficial position to correct for patient motion. While the short readout times in the order of 10 ms per baseline images limits intra-image motion, patient movement can induce significant inter-image motion-related variance to the MRF signal trace and disrupts the spin excitation history of the acquisition (Friston et al., 1996; ?), leading to motion artefacts in parameter maps (Cruz et al., 2017; Mehta et al., 2017; Xu et al., 2017). Offline image registration was previously shown to mitigate most motion artefacts in other time-series data (Cox and Jesmanowicz,

1999; Friston et al., 1995), potentially facilitating retrospective motion correction on the individual baseline images in MRF.

Hence, in this study, we aim to evaluate the motion sensitivity of two MRF methods; 1) a balanced steady-state free precession with spiral readout (MRF-bSSFP) (Ma et al., 2013) and 2) spoiled gradient echo imaging with Cartesian echo-planar readout (MRF-EPI) (Rieger et al., 2017b). Further, we alleviate the issue of motion sensitivity in MRF-EPI by intensity based motion correction of the baseline images. Simulations and phantom experiments are performed to evaluate the accuracy of parameter mapping in the presence of various motion patterns. Motion corrupted phantom measurements and *in vivo* scans in healthy subjects with and without deliberate motion are obtained in order to study the feasibility, correctness and accuracy of the correction algorithm.

5.2 Methods

5.2.1 Numerical Simulations

In order to evaluate translational and rotational motion sensitivity of MRF-bSSFP and MRF-EPI, MRF measurements were simulated for T_1 and $T_2^{(*)}$ (T_2 for MRF-bSSFP and T_2^* for MRF-EPI) maps from *in vivo* head images. For each pixel the fingerprint was simulated based on the Bloch-equations for the corresponding T_1 and $T_2^{(*)}$ values. The simulations for the MRF-bSSFP were based on the code provided in the supplementary information by Ma et al. (Ma et al., 2013), the fingerprints of the MRF-EPI were simulated based on the equations described in (Rieger et al., 2017b). Following sequence parameters were chosen for the fingerprint simulations of the MRF-bSSFP: TR=10.5-14 ms, flip angle=0-65°, number of baseline images=1000, scan-time=12.2s, TR and flip angle pattern were chosen as described by Ma et al. (Ma et al., 2013). MRF-EPI: TR=48-109 ms, TE=14-74 ms, flip angle=0-58°, number of baseline images=160, scan-time=10 s, TR, TE and flip angle pattern were used as previously described (Rieger et al., 2017b). To account for the highly undersampled spiral readout in the case of the MRF-bSSFP, a variable-density spiral trajectory was used, which was rotated by 7.5° in each TR. In the case of the MRF-EPI subsampling of the k-space was not needed, as the baseline images are based on fully sampled k-space.

Two sets of experiments were performed to study 1) the motion sensitivity depending on the time of onset of motion and 2) to assess the effect of rotational and translational motion and parameter quantification.

Motion sensitivity depending on the time of motion onset was evaluated by corrupting one second worth of images, resembling sneezing or swallowing, with a fixed rotation of 14° around the image center and translation of 5 pixels in each direction, corresponding to 100 and 16 images for the MRF-bSSFP and MRF-EPI, respectively. The time of onset was varied from the beginning to the end of the simulated measurement in steps of 250 ms. The resulting T_1 and $T_2^{(*)}$ maps from the motion corrupted fingerprints were calculated and the deviation from the ground truth was assessed using the normalized root-mean-square error (NRMSE).

To assess the effect of rotational and translational motion, the first second worth of images was corrupted by rotating or translating the images by 1-20° in steps of 1° and 1-20 pixel in steps of 1 pixel, and the NRMSE of the T_1 and $T_2^{(*)}$ maps from the ground truth was calculated.

5.2.2 Motion Correction

Retrospective motion correction was performed by co-registering each baseline image to the first image, which was chosen as reference, due to the highest baseline SNR. As previously proposed for co-registration of images with different contrasts, putative image similarity was assessed as mutual information between two baseline images, by examining the joint probability distribution of a subset of pixel intensities from both images (Maes et al., 1997). To speed up registration, a random voxel subset was used, as previously shown to result in negligible difference compared to full image analysis (Klein et al., 2005). The registration was performed by maximizing the mutual information, thereby minimizing the entropy between the relative probability distributions of the images, using an evolutionary optimization algorithm. The algorithm was based on a (1+1)-Evolution Strategy (Schwefel, 1993), by which in each optimization step the current value (parent) was randomly mutated to select a new position (child) in the parameter space. If the child's fitness was as least as good as the parents, it became the new parent, otherwise it was discarded, such that the fittest individual survived. The mutation was performed by adding a multi-dimensional random variable to the parent (Styner et al., 2000). The covariance matrix of the multi-dimensional normal distribution was updated each step by increasing or decreasing the covariance matrix by a growth factor=1.05, depending if the child (increasing) or adult (decreasing) was fitter. The parameters for the evolutionary algorithm were chosen as follows: maximum iteration=1000, initial size of search radius= 15.6×10^{-3} , minimum size of search radius= 1.5×10^{-8} . To reduce computational cost, image similarity was calculated based on 500 randomly chosen pixels, as commonly employed in image registration. This set of pixels was kept constant for the duration of the maximization. Prior to the co-registration, all images were low-pass filtered with a 2D Gaussian smoothing kernel with standard deviation of 2 to reduce the influence of noise.

5.2.3 Measurement parameters

To test the effect of motion on the parameter maps of MRF-EPI, phantom and *in vivo* data were acquired on a 3 T whole-body scanner (Magnetom Trio; Siemens Healthineers, Erlangen, Germany) using a 32-channel head array coil for *in vivo* measurements and 30-channels of a body and spine array for phantom scans. This study was approved by the local institutional review board (IRB) and all subjects provided written informed consent prior to examination. MRF-EPI was performed with the following parameters: TE/TR=14-75 ms/48-109 ms, flip angle=0-58°, FOV= $220 \times 220 \times 5 \text{ mm}^3$, voxel size= $1.7 \times 1.7 \times 5.0 \text{ mm}^3$, band-width=1395 Hz/pixel, partial-Fourier=6/8, parallel imaging factor 3 with GRAPPA reconstruction, reference lines=24 acquired in-place for each baseline image, acquisition time / slice=10s, total number of baseline images=160.

5.2.4 Phantom experiments

The effect of translational motion on the parameter estimation of MRF-EPI was evaluated in phantom scans. For this purpose, the phantom was acquired twice in the coronal plane with MRF-EPI and then successively moved with the automatic table movement from the original position by following distances: 2, 4, 6, 8, 12, 16, 24 mm. At each position the phantom was acquired twice. The phantom consisted of three tubes with a diameter of 30 mm, each containing a single gadoterate-meglumine (Dotarem; Guerbet, Villepinte, France, concentration: 0.39-1.5625 $\mu\text{mol/ml}$) doped water compartment. The first 17 baseline images of each of the moved phantom measurements were combined with the unmoved phantom measurements to mimic a movement after the first second of the scan. T_1 and $T_2^{(*)}$ maps were calculated from the hybrid motion corrupted fingerprints and the NRMSE and standard deviation from the ground truth uncorrupted data was calculated.

5.2.5 *In vivo* experiments

In vivo data of 8 healthy volunteers (5 male, 27 ± 3 years) was acquired with MRF-EPI to evaluate the application of the motion correction method for *in vivo* measurements. The same slice position was acquired twice in each volunteer: 1) without subject motion 2) with motion artefacts induced by instructing all volunteers to move their head by approximately 20° after 2 seconds of the acquisition. T_1 and T_2^* maps with and without motion correction were qualitatively compared. To evaluate the quality of the motion correction of the baseline images, the Dice index (Dice, 1945) was computed before and after motion correction. For two segmented regions A and B, the Dice index is defined as $Dice(A, B) = 2 \times area(A \cap B) / (area(A) + area(B))$. The regions A and B were calculated by segmenting the baseline images by means of the unified segmentation described by (Ashburner and Friston, 2005) (included in SPM12 software package <http://www.fil.ion.ucl.ac.uk/spm>). The area enclosed by the brain masks was used for evaluation. Image segmentation was manually curated to avoid masking artefacts arising from residual ghosting signal or low SNR in some baseline images. The DICE coefficient with reference to the first image was calculated for two selected images for evaluation across the population: the 10th image which was prior to motion onset in all subjects and the 99th image which was displaced in all subjects. These Dice coefficients of all volunteers were statistically compared among the three-measurement series (reference, corrupted and corrected) independently for both images using two-way analysis of variance with balanced design (ANOVA) after using log-transformation to restore normality in the value distribution. In case of significant differences on the group level Student's t-test was used for paired comparisons between methods. P values less than 0.05 were considered to be significant. For one exemplary volunteer, the Dice coefficient of each baseline image compared to the first image was calculated to show the evolution of the index throughout the measurement. This was done for the reference measurement without any movement, a motion corrupted and corrected measurement. Baseline images with very low SNR (flip angle $< 5^\circ$) were discarded from the time series analysis, as image segmentation was heavily impaired for these images.

5.3 Results

5.3.1 Numerical Simulations

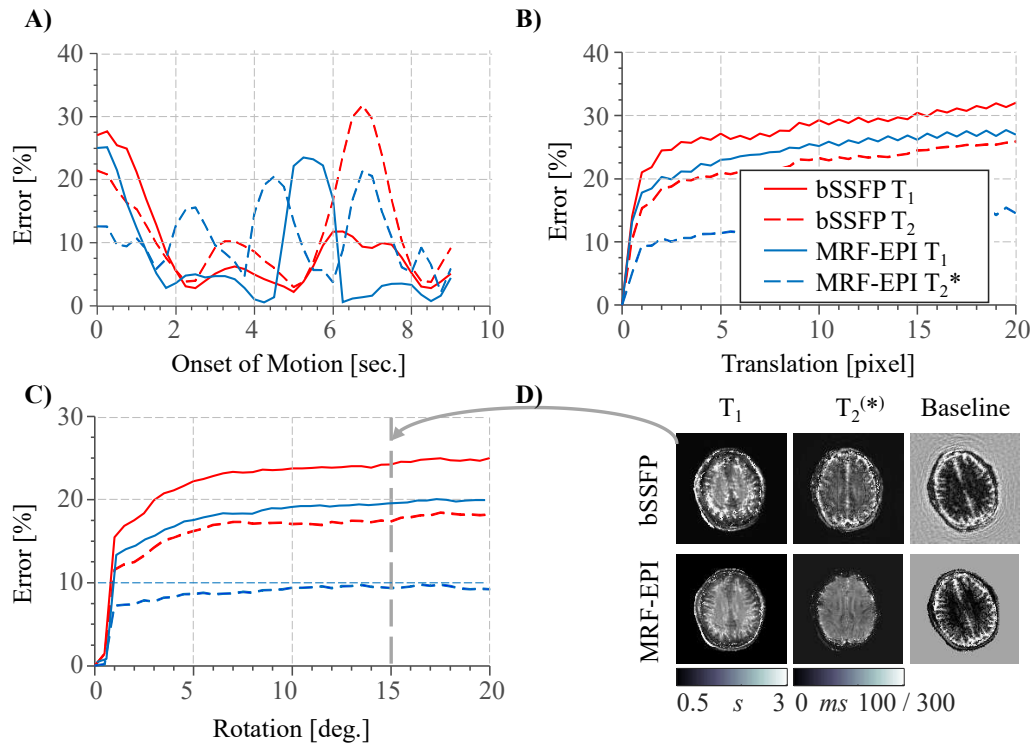


Figure 5.1: (A) Quantification error due to 1 second of motion with variable onset of motion during the scan. Quantification error as a function of the translation (B) and rotation (C). (D) Exemplary T_1 and $T_2^{(*)}$ maps and baseline images of motion corrupted numerical phantom with a rotation of 15° within the first second of the scan. Motion artefacts, such as blurring, are visible in all T_1 and $T_2^{(*)}$ maps

Figure 5.1 a shows the average NRMSE quantification error of the T_1 and $T_2^{(*)}$ maps in the presence stepwise motion occurring during one second of the acquisition depending on the time of motion onset. T_1 quantification is highly sensitive to motion in the first 1-2 seconds of the scan for both MRF methods (NRMSE up to 28%). $T_2^{(*)}$ is sensitive to motion throughout the measurement for both methods. The quantification error of both MRF methods correlates strongly with the amount of rotation and translation for both T_1 and $T_2^{(*)}$ (Figure 5.1 b-c NRMSE up to 32%). A steep slope indicates high susceptibility even to small motion. Motion artefacts are visible in exemplary parameter maps of both bSSFP and MRF-EPI (Figure 5.1 d).

5.3.2 Phantom experiments

Figure 5.2 shows the average T_1 and T_2^* quantification error of phantom measurements depending on translational motion for phantom motion one second after the start of the measurement. Phantom results largely mimic the trend in numerical simulations (compare Figure 1b). Both T_1 and T_2^* error increase characteristically with larger translation, while T_1 has higher average error as the

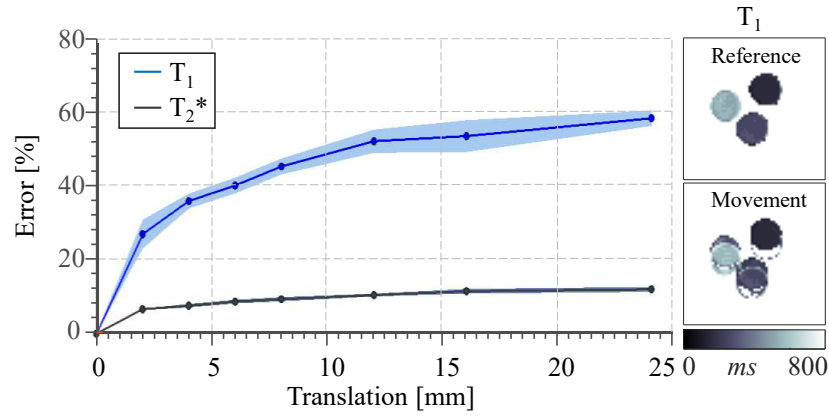


Figure 5.2: Quantification error in phantom measurements with MRF-EPI depending on translation motion. Displacement induces clear ghosting artefacts and leads to progressively increasing quantification errors

motion occurs in the early stage of the measurement. Blurring and artefacts are clearly visible in the T_1 map of the measurements effected by motion.

5.3.3 *In vivo* experiments

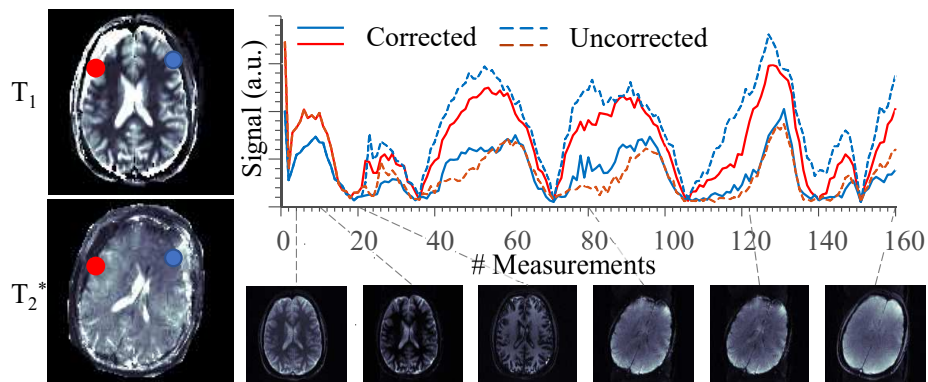


Figure 5.3: T_1 and $T_2^{(*)}$ maps of a measurement with patient movement and exemplary uncorrected and corrected fingerprints from two brain regions (red and blue circle). Baseline images are shown as reference. Substantially corrupted signal paths are observed in the presence of motion.

Example motion corrupted and corrected fingerprints of two representative voxels (Figure 5.3) depict distinctly different signal paths. Motion-corrupted MRF maps show major quality deterioration in both T_1 and T_2^* maps, with visual blurring and edge artefacts (Figure 5.4). Improved image quality with visually ameliorated artefacts and increased co-registration of the quantitative maps are observed after image registration.

Figure 5.5 a shows the Dice index throughout the acquisition of a representative volunteer, comparing the reference measurement without any movement, a motion corrupted and motion corrected measurement. For the motion corrupted measurement, a step drop is observed at baseline image 20, which corresponds to the time point of motion onset. No such stepwise decrease is observed in the motion corrected data. The average Dice indices of the reference / motion corrupted / motion corrected measurement are $98.0 \pm 1.3\%$, $85.6 \pm 2.3\%$ and

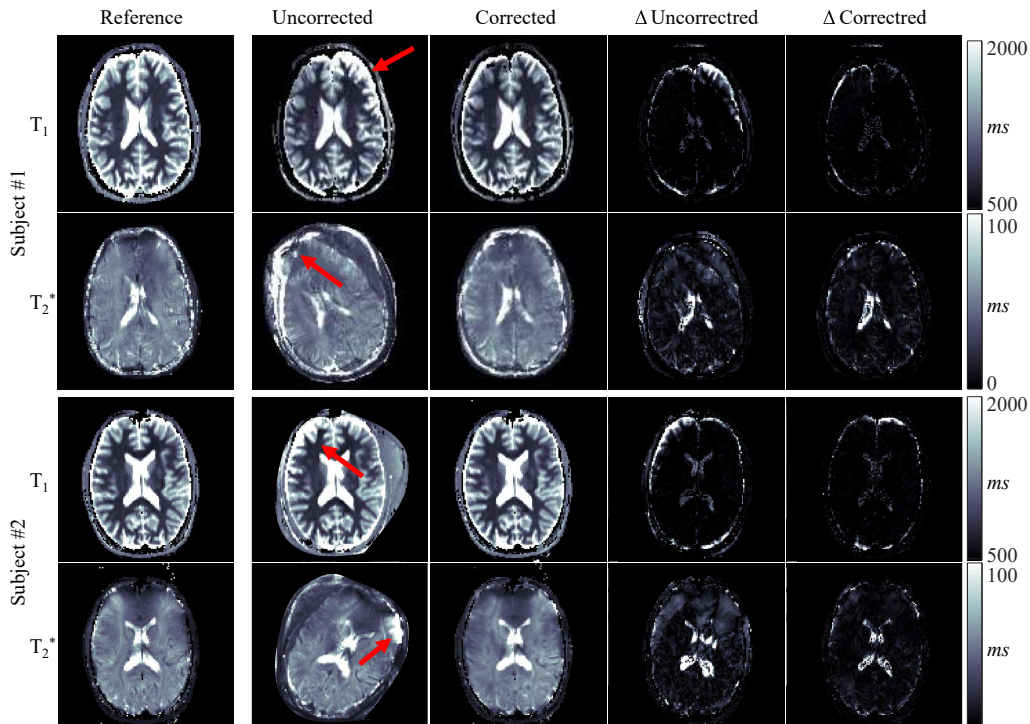


Figure 5.4: Example T_1 and T_2^* maps acquired in two healthy subjects. The first column depicts a motion free reference scan, the second and third column are generated from a motion corrupted measurement without and with using the proposed motion correction scheme, respectively. The last two columns shows the differences between reference and corrected / uncorrected images. artefacts are clearly visible in the motion corrupted data set, especially at tissue interfaces as indicated by the red arrow and in the difference maps. Motion corrected maps depict visually comparable image quality to the motion free reference scan

97.0±1.4%, respectively. Here, Dice values of 100% are rarely achieved even in the motion free reference, due to imperfect segmentation. The sum of the baseline image segmentation masks of the reference scan and the motion corrected data are visually comparable (Figure 5.5 b), depicting sharp edges of the head. Motion can be clearly seen in the uncorrected baseline images, showing major displacement in addition to blurry edges, which indicate poor co-registration. Figure 5.5 c shows the average Dice index of all volunteers at the beginning of the measurement without motion (baseline image 10) and towards the end of the measurement after motion (baseline image 99). No significant difference in the Dice index of the three series (reference, corrupted and corrected) was observed for the 10th image (ANOVA: $p = 0.56$). However, group analysis and pair wise comparison show significantly decreased DICE coefficients at image 99 in the corrupted series (ANOVA: $p < 0.0004$, corrupted vs reference: $p < 0.05$). Image registration as proposed successfully restores the DICE coefficient, providing comparable image quality to the reference data (corrected vs reference: $p = 0.26$), while being significantly improved compared to the motion corrupted data (corrected vs corrupted: $p < 0.002$).

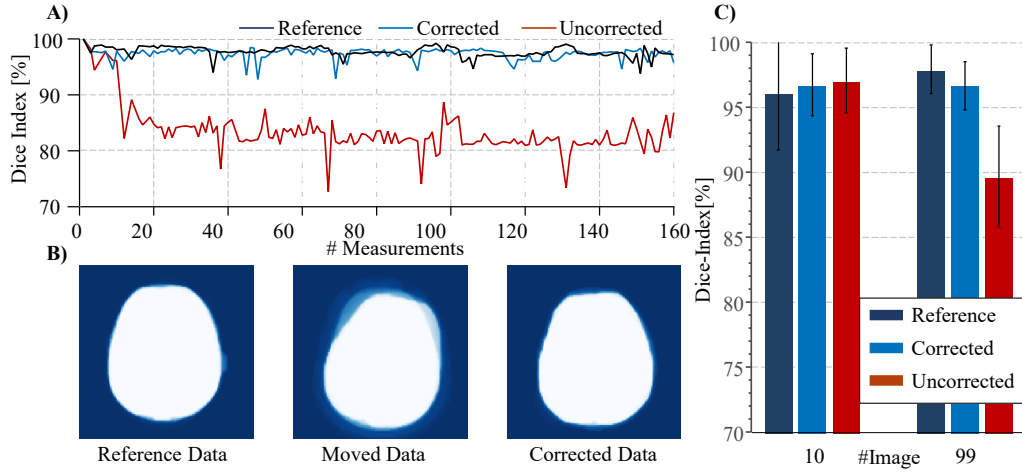


Figure 5.5: (A) Dice index between the first image and the other baseline images, of a motion free reference, a motion corrupted but uncorrected and a corrected *in vivo* measurement. The motion induced drop in the dice index, as observed in the motion corrupted data, is successfully alleviated using the proposed image registration. (B) Sums of baseline images from different data sets visualize the different level of overlap, of the motion free, motion corrupted and motion corrected data in the same subject as (A). Uncorrected motion leads to blurry edges and poor alignment of the baseline images, while the proposed correction scheme results in sharp delineation of the skull comparable to the motion free reference. (C) Average Dice index across all volunteers for a baseline image without movement (#10) and with movement (#99), showing significantly higher Dice values using the proposed image registration, as compared to the uncorrected data in the presence of motion.

5.4 Discussion

In this study, we have demonstrated that MRF exhibits residual motion-sensitivity. Simulation data shows parameter map quality deterioration for both spiral and Cartesian-EPI readout. Phantom and *in vivo* parameter maps acquired with MRF-EPI suffer from severe edge artefacts in the presence of motion corruption. The motion sensitivity, however, can be successfully mitigated with intensity based image co-registration. Motion insensitivity of MRF has been observed in several studies for specific motion types. This include motion that occurs very late within the measurement (Ma et al., 2013) or if only few non-consecutive baseline images are corrupted by motion, such as induced by the rapid respiratory motion of small animals (Anderson et al., 2018; Gao et al., 2015). The simulations and experiments in this study show that MRF is generally sensitive to motion, though the sensitivity varies depending on the onset and severity of motion. Due to the strong contrast variation of the baseline images throughout the measurement, the intensity of the artefacts in the T_1 and $T_2^{(*)}$ parameter maps exert different sensitivity profiles to the time point of motion within the acquisition. T_1 is highly sensitive during the beginning of a measurement, likely caused by dominant longitudinal magnetization recovery following the inversion pulse. Simulations demonstrate that already small translations at the beginning of the measurements results in considerable T_1 quantification errors, showing strong artefacts including ghosting and blurring in the parameter maps for both MRF methods. $T_2^{(*)}$ is considerably less sensitive to motion than T_1 in the initial stages of the acquisition,

possibly due to the predominant $T_2^{(*)}$ weighting in the majority of baseline images and the more homogeneous spread of this contrast information throughout the measurement. The high number of baseline images acquired in MRF offers a unique position to correct for patient motion. Short readout times of the baseline images limit artefacts that are induced by motion during the readout, as patient motion is slow compared to the readout time. This facilitates retrospective motion correction by compensating for inter-image motion on the individual baseline images, as it is routinely performed for fMRI (Power et al., 2014) and diffusion (Kober et al., 2012). However, the vast differences in contrast weighting among the baseline images throughout the measurement and the low SNR compared with traditional MRI images pose a challenge to image registration algorithms (Roujol et al., 2015; Xue et al., 2012). Intensity based image co-registrations based on mutual information is well suited for correcting images with different contrast (Woo et al., 2015). The first baseline image was chosen as the reference image, as this image has the highest SNR within the measurement, though choosing other or multiple reference images could lead to improved results. The intensity based image registration failed in few images with very low SNR. However, due to the inner product matching of the fingerprint with the dictionary, these very low SNR images carry little weight for the parameter mapping. Accordingly, no detriment in the *in vivo* image quality was visually observed in these cases. While intensity based image registration is the most commonly used similarity measure (Oliveira and Tavares, 2014), other registration methods such as feature based similarity measures (Faber and Stokely, 1988; Oliveira et al., 2009) or prospective motion correction via an optical tracking systems (Callaghan et al., 2015) could improve correction quality. Performing intensity based motion correction on the baseline images of the MRF-EPI leads to artefact-free parameter maps of high quality, except some susceptibility artefacts in the T_2^* maps due to air-tissue interface, which are also visible in the reference maps. Dice index of corrected baseline images show good agreement with reference measurement without motion. As the algorithm is independent of the slice location and the patient, the parameters of the algorithm do not require patient specific adjustment. Hence, a single set of registration parameters was successfully used throughout the study. Due to the higher SNR of the MRF-EPI compared to MRF based on spiral readout, MRF-EPI is particularly well-suited for image registration of baseline images. Undersampling artefacts might cause image registration to fail in MRF based on spiral readout. However, averaging-window reconstructions, as previously proposed (Cao et al., 2017), may be employed to overcome this limitation and foster motion robustness in spiral MRF. This study has several limitations. Due to the lack of a spiral MRF sequence at our center, no direct comparison could be performed regarding phantom and *in vivo* motion sensitivity, as well as suitability for motion-correction. Furthermore, in this study only a small number of healthy subjects were scanned as proof of concept. The subjects were asked to execute a single displacement during the scan, which might not be representative to all motion patterns observed in clinical patient scans. Larger cohorts with specific diseases and characteristic motion remain to be evaluated. Additional, only in-plane motion was evaluated and corrected for, due to the single-slice implementation of MRF-EPI. To correct for through-plane motion, volumetric implementations of MRF, such as recently proposed (Liao et al., 2017;

Ma et al., 2018) are to be evaluated, and will be subject of future studies. In this study the MRF-bSSFP was chosen as an example of a MRF sequence with spiral readout, though other method have been proposed and their motion sensitivity should be subject to further research to gain a wider understanding of motion sensitivity of MRF.

5.5 Conclusion

Numerical simulations show that MRF exhibits residual motion-sensitivity, for spiral and Cartesian-EPI based MRF. Phantom and *in vivo* measurements using MRF-EPI confirmed this trend. The proposed intensity-based correction method can be used for MRF-EPI to foster motion-robustness and successfully obtain artefact-free T_1 and T_2^* maps in the presence of subject motion.

Statement of Contribution

In this study I was responsible for the conceptual design and was partially involved in the data acquisition and analysis. Further, I did the literature research and wrote the manuscript.

Summary 6

In recent years, quantitative MRI has gained increasing attention due to the introduction of novel measurement methods, possibly offering the opportunity for quantitative imaging to be integrated into clinical routine. As quantitative MRI can be used for a range of biomarkers for tissue characterization, such as for cancer studies, to support therapy planning and patient management, clinical MRI diagnostics could benefit from quantitative imaging. While some quantitative methods have already been integrated into clinical routine, such as diffusion and perfusion, the quantification of relaxation times is generally not used due to the relative time-consuming methods needed. Magnetic resonance fingerprinting was introduced as a promising method for fast quantification of multiple physiological parameters including the relaxation times T_1 and T_2 . First clinical studies with MRF methods based on spiral readout have demonstrated the utility of MRF, mainly focusing on brain and prostate quantification of relaxation parameters.

In this work a novel MRF technique was developed for simultaneous quantification of T_1 and T_2^* relaxation times based on Cartesian readout, potentially fostering usability and robustness, while offering the possibility to quantify T_2^* with MRF. Using gradient-spoiled EPI images with rapid, parallel-imaging accelerated Cartesian readout, quantitative maps could be acquired within 10 s per slice. Tissue specific signal traces were generated using an initial inversion pulse for enhanced T_1 weighting and varying the flip-angles, echo-times and repetition-times throughout the sequence, leading to parameter maps of high visual quality. The method was shown to have high quantification accuracy and precision, both in phantom and *in vivo* measurements. However, the method initially required full magnetization relaxation after the measurement of each slice which extended the measurement times and limited the clinical applicability. Therefore, the technique was improved regarding acquisition efficiency and volumetric coverage by developing a slice interleaved implementation of the MRF-EPI. Slice interleaving increased the effective repetition time of the spoiled gradient echo readout acquisition in each slice, hence increasing the SNR of the baseline images. Numerical simulations suggested that the acquisition of four slices as an optimal trade-off between quantification precision and scan-time, resulting in a 4-fold scan-time reduction with comparable performance to the single-slice MRF-EPI.

Having developed robust and rapid MRF methods for T_1 and T_2^* quantification, the third scientific study in chapter 5 focused on analysing the motion sensitivity of MRF and developed a correction scheme for the MRF-EPI methods. In the first step, the motion sensitivity was evaluated in simulations for the original

MRF implementation by (Ma et al., 2013) and our MRF-EPI, showing that both methods are sensitive to motion, causing blurring and ghosting artefacts. These motion artefacts could be mitigated both in simulations and in *in vivo* measurements by using an intensity-based co-registration of the baseline images.

A more detailed summary is provided in the following subsections.

Magnetic Resonance Fingerprinting using Echo-Planar Imaging: Joint Quantification of T_1 and T_2^* Relaxation Times

Magn Reson Med, doi: 10.1002/mrm.26561

In the third chapter, a novel MRF method was introduced based on spoiled echo-planar imaging readout for simultaneous assessment of T_1 and T_2^* . The method was based on the acquisition of 160 spoiled gradient EPI images. To shorten measurement times, the EPI readout was accelerated by using partial Fourier, acquiring only 5/8 of the k-space. Further, parallel imaging with an acceleration factor of 3 was used to shorten the readout time. An inversion pulse was included in the sequence to enhance T_1 sensitivity. Additional contrast variations were induced among the baseline images by varying the flip angles and echo times thorough the measurement, increasing the dissimilarity of the fingerprints depending on the underlying tissue. The dictionary simulations were based on the Bloch equations, accounting for imperfect slice excitation by including B_1^+ correction in the magnetization simulations. Pattern matching of the acquired fingerprints with the dictionary elements was performed with the magnitude data, choosing the dictionary element with the highest inner product as the best match. While other MRF implementations use complex matching of the data to derive additional off-resonance maps, the quantification precision of the proposed method decreases using complex data due to the increased number of fit parameters while increasing computational complexity. The proposed sequence was implemented on a 3 T magnet using a 32-channel head coil.

MRF-EPI was evaluated in phantom scans and the quantification precision and accuracy of the MRF method was compared to the reference sequences: an IR-SE for T_1 mapping and GRE for T_2^* quantification. MRF-EPI showed good agreement with the reference T_1 and T_2^* measurements with average deviations of $-2\pm 3\%$ and $2\pm 3\%$ for T_1 and T_2^* , respectively. *In vivo* maps acquired with the proposed sequence in 6 healthy subjects were of high visual quality and free of artefacts, comparable to the maps of the reference measurements. T_1 maps were homogeneous throughout grey and white matter and detailed structures were clearly visible on the T_2^* maps. *In vivo* relaxation times compared well to the reference acquisitions despite the substantially shortened scan time of only 10 s per slice.

MRF-EPI showed promising results for combining the MRF paradigm with Cartesian readout, simultaneously acquiring T_1 and T_2^* maps. With similar acquisition time as other single slice MRF methods, the Cartesian readout potentially increased usability and robustness.

Time efficient whole-brain coverage with MR Fingerprinting using slice-interleaved echo-planar-imaging

Sci. Rep., doi: 10.1038/s41598-018-24920-z

The fourth chapter described a slice-interleaved implementation of the MRF-EPI from the third chapter, increasing volumetric coverage while decreasing the average acquisition time per slice. The MRF-EPI was modified to acquire several slices in a randomized interleaved manner. Increasing the number of interleaved slices lead to an effective increase of the slice repetition time, resulting in higher SNR baseline images. Simulations demonstrated that four slices were the optimal number to acquire in an interleaved manner, given a target measurement time of 17 seconds. Acquiring less than four slices increased the overall measurement time, however acquiring more than four slices resulted in a loss of quantification precision, both for T_1 and T_2^* . This was attributed to insufficient sampling rate of the signal variations.

In addition to the T_1 and T_2^* quantification, PD maps were created with the proposed method. The PD maps were calculated in a two-step process without the need for additional measurements: First, the semi-quantitative M_0 maps were calculated from the fingerprints and the corresponding matched dictionary element. The M_0 maps were subsequently compensated for B_1^+ and the coil sensitivity profile, the latter calculated from the M_0 maps by means of the bias field. Finally, the corrected M_0 maps were normalized to the cerebrospinal fluid, which allowed for quantitative proton density mapping for the first time with an MRF sequence.

Due to the higher resolution of the slice interleaved sequence with $1.0 \times 1.0 \times 3.0 \text{ mm}^3$ compared to the single slice MRF-EPI with $1.7 \times 1.7 \times 5.0 \text{ mm}^3$, the readout times of each baseline image increased. This prolonged the overall measurement time from 10 to 17 seconds for one slice for the MRF-EPI and four slices for the slice interleaved implementation. Nevertheless, phantom scans demonstrated that the proposed sequence had comparable precision and accuracy to the single slice MRF-EPI and gold standard sequences, despite using higher resolution. *In vivo* whole-brain coverage of T_1 , T_2^* and PD with 32 slices was acquired in 6 healthy volunteers and 4 multiple sclerosis patients, within 3:36 minutes. The lesions of the MS patients were clearly visible, with higher T_1 , T_2^* and PD values than the surrounding tissue, allowing quantitative discrimination.

The slice-interleaved MRF-EPI allowed for volumetric analysis of quantitative T_1 , T_2^* and PD values, offering the possibility of quantitative tissue characterization, as it was shown exemplary with the lesions of multiple sclerosis patients. The sequence demonstrated an acceleration factor of four compared to the MRF-EPI, while maintaining quantification accuracy, despite offering higher resolution of $1.0 \times 1.0 \times 3.0 \text{ mm}^3$.

Improved motion robustness for EPI-based MR Fingerprinting using intensity based image registration

Sci. Rep., submitted

The fifth chapter of this thesis explored the motion sensitivity of MRF methods and a correction scheme for the MRF-EPI was developed. The motion

sensitivity of the original bSSFP-MRF based on spiral readout and the MRF-EPI from the third chapter were evaluated through simulations, determining the quantification accuracy in presence of rotational and translational motion and the time of motion onset. In simulations, a subset of the baseline images were corrupted by motion and the motion corrupted fingerprints were matched with the dictionary. While both MRF methods exhibited residual motion sensitivity, resulting in imaging artefacts and quality deterioration of the parameter maps, sensitivity varied depending on the onset and severity of motion. While T_1 was highly sensitive during the beginning of a measurement, T_2 and T_2^* were sensitive throughout the measurement.

A motion correction scheme based on a retrospective intensity-based co-registration of the individual baseline images was implemented for the MRF-EPI and validated in phantom and *in vivo* measurements on 8 healthy volunteers. All images were co-registered to the first baseline image, as this image had the highest SNR within the measurement. The correction algorithm was based on maximizing the mutual information, using an evolutionary optimization algorithm to align the images. The Dice index was used to evaluate the quality of the motion correction. The corrected parameter maps were compared to the reference measurements without motion and the motion corrupted maps. Applying the intensity-based motion correction method on the baseline images led to artefact-free parameter maps of high quality, visually comparable to the reference maps, both in phantom and *in vivo* measurements. Dice indices of corrected baseline images showed good agreement with reference measurements without motion.

As both MRF methods were found to exhibit residual motion-sensitivity, leading to quantification errors and artefacts in the parameter maps, motion correction schemes should prove useful in the clinical application of MRF to limit the need for scan repetition due to motion corrupted images. The proposed intensity-based correction method for MRF-EPI should foster motion-robustness, making the sequence more applicable in clinical routine.

Outlook **7**

MRI is one of the major imaging modalities, still gaining significance in the clinical practice, as it provides medical *in vivo* images without the need for ionizing radiation. In the field of MRI, a large number of technological developments and improvements are proposed every year, ranging from better hardware, increasingly faster acquisition techniques, to new reconstruction algorithms. Incorporating some of these ideas into the proposed MR fingerprinting technique, such as simultaneous multislice imaging or faster dictionary matching algorithms, will increase the acquisition speed and improve robustness of the parameter estimation, facilitating the usage of MRF for clinical routine.

While the MRF-EPI was developed for neurological applications, optimizing the sequence parameters and motion correction algorithms for this purpose, the method is not limited to the quantification of brain tissue. The quantitative diagnosis of other organs is of high clinical interest, such as the prostate or the liver. However, most body parts are subject to respiratory motion, leading to deformation and movement in all spatial directions. The developed MRF sequence is well suited to be used for many other body parts, only minor changes to the sequence design and parameter choice would be needed. To compensate for motion, elaborate retrospective motion correction algorithms can be used to mitigate the respiratory motion, to ensure artefact free parameter maps.

For widespread clinical usage of the proposed method, short acquisition times and direct and fast reconstruction on the MRI is useful, such that the clinicians can directly evaluate the quantified maps. The slice interleaved MRF-EPI sequence already has clinically acceptable acquisition times, taking less than four minutes for whole-brain coverage. The measurement efficiency could be further improved by including new technical developments in MRI, such as simultaneous multislice imaging, enabling the simultaneous acquisition of multiple slices. Our initial experiments show that the acquisition time could be reduced by a factor of four without loss of precision. Pattern matching was implemented on the MRI hardware, such that the maps can be directly viewed and processed on the MRI consoles. While the dictionary matching took multiple minutes, faster matching algorithms and improved hardware will shorten the matching process, resulting in nearly instantaneous reconstruction of the parameter maps.

The proposed methods offer the possibility for model free quantification. While currently the fingerprints are matched to a precomputed dictionary for the quantification of the tissue parameters, the fingerprints could be matched to a reference tissue instead of simulations. By acquiring MRF data from multiple

volunteers and determining a reference signal for each tissue type, e.g. gray and white matter, direct tissue matching could be performed with the acquired fingerprints. This could prove as a fast and robust method for tissue segmentation and anomaly detection, e.g. for tumors or lesions.

One of the shortcomings of MRI compared to other imaging modalities is the lack of quantification, relying mainly on weighted images for diagnostic purposes. With the development of new quantification methods for MRI, such as the methods presented in this work, the likelihood increases that quantitative diagnosis will become the standard clinical practice. The proposed slice-interleaved MRF-EPI sequence offers multi-parametric quantification in clinically acceptable scan time. Further, the motion correction increases the robustness of the parameter maps in real-world setting. For these reasons, the sequence is currently being used in two clinical trials on multiple sclerosis patients to gain insights on the relaxation times in lesions, with the aim to function as biomarkers for staging of the disease. With the insights from these first clinical studies, the sequence can be further optimized with regard to usability and accuracy. This will offer the opportunity to use the method for other diseases and body parts, promoting the usage of full quantitative diagnosis in clinical routine by means of MRF-EPI.

Bibliography

- Afacan, O., Hoge, W. S., Janoos, F., Brooks, D. H. and Morocz, I. A. (2012). Rapid full-brain fMRI with an accelerated multi shot 3D EPI sequence using both UNFOLD and GRAPPA. *Magn Reson Med* 67, 1266–1274.
- Alley, M. T., Glover, G. H. and Pelc, N. J. (1998). Gradient characterization using a Fourier-transform technique. *Magn Reson Med* 39, 581–587.
- Amthor, T., Doneva, M., Koken, P., Sommer, K., Meineke, J. and Börnert, P. (2017). Magnetic Resonance Fingerprinting with short relaxation intervals. *Magn Reson Imaging* 41, 22–28.
- Anderson, C. E., Wang, C. Y., Gu, Y., Darrah, R., Griswold, M. A., Yu, X. and Flask, C. A. (2018). Regularly incremented phase encoding - MR fingerprinting (RIPE-MRF) for enhanced motion artifact suppression in preclinical cartesian MR fingerprinting. *Magn Reson Med* 79, 2176–2182.
- Anderson, L. J., Holden, S., Davis, B., Prescott, E., Charrier, C. C., Bunce, N. H., Firmin, D. N., Wonke, B., Porter, J., Walker, J. M. and Pennell, D. J. (2001). Cardiovascular T2-star (T2*) magnetic resonance for the early diagnosis of myocardial iron overload. *Eur Heart J* 22, 2171–2179.
- Andre, J. B., Bresnahan, B. W., Mossa-Basha, M., Hoff, M. N., Smith, C. P., Anzai, Y. and Cohen, W. A. (2015). Toward Quantifying the Prevalence, Severity, and Cost Associated With Patient Motion During Clinical MR Examinations. *J Am Coll Radiol* 12, 689–695.
- Ashburner, J. and Friston, K. J. (2005). Unified segmentation. *NeuroImage* 26, 839–851.
- Assländer, J., Cloos, M. A., Knoll, F., Sodickson, D. K., Hennig, J. and Lattanzi, R. (2018). Low rank alternating direction method of multipliers reconstruction for MR fingerprinting. *Magn Reson Med* 79, 83–96.
- Assländer, J., Glaser, S. J. and Hennig, J. (2017). Pseudo Steady-State Free Precession for MR-Fingerprinting. *Magn Reson Med* 77, 1151–1161.
- Badve, C., Yu, A., Dastmalchian, S., Rogers, M., Ma, D., Jiang, Y., Margevicius, S., Pahwa, S., Lu, Z., Schluchter, M., Sunshine, J., Griswold, M., Sloan, A. and Gulani, V. (2017). MR Fingerprinting of Adult Brain Tumors: Initial Experience. *AJNR Am J Neuroradiol* 38, 492–499.

- Badve, C., Yu, A., Rogers, M., Ma, D., Liu, Y., Schluchter, M., Sunshine, J., Griswold, M. and Gulani, V. (2015). Simultaneous T1 and T2 Brain Relaxometry in Asymptomatic Volunteers using Magnetic Resonance Fingerprinting. *Tomography* *1*, 136–144.
- Baksi, A. J. and Pennell, D. J. (2013). T1 Mapping in Heart Failure. *Circ Cardiovasc Imaging* *6*, 861–863.
- Barnet, C., Zanche, N. D. and Pruessmann, K. P. (2008). Spatiotemporal magnetic field monitoring for MR. *Magn Reson Med* *60*, 187–197.
- Barth, M., Breuer, F., Koopmans, P. J., Norris, D. G. and Poser, B. A. (2016). Simultaneous multislice (SMS) imaging techniques. *Magn Reson Med* *75*, 63–81.
- Bloch, F. (1946). Nuclear Induction. *Phys Rev* *70*, 460–474.
- Block, K. T. and Frahm, J. (2005). Spiral imaging: A critical appraisal. *J Magn Reson Imaging* *21*, 657–668.
- Bottomley, P. A., Hardy, C. J., Argersinger, R. E. and Allen-Moore, G. (1987). A review of ¹H nuclear magnetic resonance relaxation in pathology: are T1 and T2 diagnostic? *Med Phys* *14*, 1–37.
- Bulluck, H., Maestrini, V., Rosmini, S., Abdel-Gadir, A., Treibel, T. A., Castelletti, S., Bucciarelli-Ducci, C., Manisty, C. and Moon, J. C. (2015). Myocardial T1 Mapping. *Circ J* *79*, 487–94.
- Buonincontri, G. and Sawiak, S. J. (2015). MR fingerprinting with simultaneous B1 estimation. *Magn Reson Med* *76*, 1127–1135.
- Buonincontri, G., Schulte, R. F., Cosottini, M. and Tosetti, M. (2017). Spiral MR fingerprinting at 7T with simultaneous B1 estimation. *Magn Reson Imaging* *41*, 1–6.
- Buxton, R. B. (1993). The diffusion sensitivity of fast steady-state free precession imaging. *Magn Reson Med* *29*, 235–243.
- Callaghan, M. F., Josephs, O., Herbst, M., Zaitsev, M., Todd, N. and Weiskopf, N. (2015). An evaluation of prospective motion correction (PMC) for high resolution quantitative MRI. *Front Neurosci* *9*.
- Cao, X., Liao, C., Wang, Z., Chen, Y., Ye, H., He, H. and Zhong, J. (2017). Robust sliding-window reconstruction for Accelerating the acquisition of MR fingerprinting. *Magn Reson Med* *78*, 1579–1588.
- Carr, H. Y. and Purcell, E. M. (1954). Effects of Diffusion on Free Precession in Nuclear Magnetic Resonance Experiments. *Phys Rev* *94*, 630–638.
- Cauley, S. F., Setsompop, K., Ma, D., Jiang, Y., Ye, H., Adalsteinsson, E., Griswold, M. A. and Wald, L. L. (2015). Fast group matching for MR fingerprinting reconstruction. *Magn Reson Med* *74*, 523–528.

- Chen, N.-k. and Wyrwicz, A. M. (1999). Correction for EPI distortions using multi-echo gradient-echo imaging. *Magn Reson Med* 41, 1206–1213.
- Chen, Y., Jiang, Y., Pahwa, S., Ma, D., Lu, L., Twieg, M. D., Wright, K. L., Seiberlich, N., Griswold, M. A. and Gulani, V. (2016). MR Fingerprinting for Rapid Quantitative Abdominal Imaging. *Radiology* 279, 278–286.
- Cheng, H.-L. M. and Wright, G. A. (2006). Rapid high-resolution T(1) mapping by variable flip angles: accurate and precise measurements in the presence of radiofrequency field inhomogeneity. *Magn Reson Med* 55, 566–574.
- Chilla, G. S., Tan, C. H., Xu, C. and Poh, C. L. (2015). Diffusion weighted magnetic resonance imaging and its recent trend—a survey. *Quant Imaging Med Surg* 5, 407–422.
- Christen, T., Pannetier, N. A., Ni, W. W., Qiu, D., Moseley, M. E., Schuff, N. and Zaharchuk, G. (2014). MR vascular fingerprinting: A new approach to compute cerebral blood volume, mean vessel radius, and oxygenation maps in the human brain. *NeuroImage* 89, 262–270.
- Cohen, O. and Polimeni, J. R. (2018). Optimized inversion-time schedules for quantitative T1 measurements based on high-resolution multi-inversion EPI. *Magn Reson Med* 79, 2101–2112.
- Cox, R. W. and Jesmanowicz, A. (1999). Real-time 3D image registration for functional MRI. *Magn Reson Med* 42, 1014–1018.
- Cruz, G., Botnar, R. and Prieto, C. (2017). Motion corrected Magnetic Resonance Fingerprinting using Soft-weighted key-Hole (MRF-McSOHO). In Proceedings of the 25th Annual Meeting of the International Society for Magnetic Resonance in Medicine (ISMRM), Honolulu, Hawaii, USA, p. 0935,.
- Dahnke, H. and Schaeffter, T. (2005). Limits of detection of SPIO at 3.0 T using T2* relaxometry. *Magn Reson Med* 53, 1202–1206.
- Davies, M., Puy, G., Vandergheynst, P. and Wiaux, Y. (2014). A Compressed Sensing Framework for Magnetic Resonance Fingerprinting. *SIAM J Imaging Sci* 7, 2623–2656.
- Deichmann, R., Adolf, H., Nöth, U., Morrissey, S., Schwarzbauer, C. and Haase, A. (1995). Fast T2-mapping with SNAPSHOT FLASH imaging. *Magn Reson Imaging* 13, 633–639.
- Deoni, S. C. (2010). Quantitative Relaxometry of the Brain. *Top Magn Reson Imaging* 21, 101–113.
- Dice, L. R. (1945). Measures of the Amount of Ecologic Association Between Species. *Ecology* 26, 297–302.
- Dietrich, O., Raya, J. G., Reeder, S. B., Reiser, M. F. and Schoenberg, S. O. (2007). Measurement of signal-to-noise ratios in MR images: Influence of multichannel coils, parallel imaging, and reconstruction filters. *J Magn Reson Imaging* 26, 375–385.

- Doneva, M., Amthor, T., Koken, P., Sommer, K. and Börnert, P. (2017). Matrix completion-based reconstruction for undersampled magnetic resonance fingerprinting data. *Magn Reson Imaging* 41, 41–52.
- Edelman, R. R., Wielopolski, P. and Schmitt, F. (1994). Echo-planar MR imaging. *Radiology* 192, 600–612.
- Ellingson, A. M., Mehta, H., Polly, D. W., Ellermann, J. and Nuckley, D. J. (2013). Disc Degeneration Assessed by Quantitative T2* (T2 star) Correlated with Functional Lumbar Mechanics. *Spine* 38.
- Faber, T. L. and Stokely, E. M. (1988). Orientation of 3-D structures in medical images. *IEEE Trans Pattern Anal Mach Intell* 10, 626–633.
- Fautz, H.-P., Paul, D., Scheffler, K. and Hennig, J. (2004). TRIM: TR independent multislice imaging. *Magn Reson Med* 51, 1239–1246.
- Feng, X., Deistung, A. and Reichenbach, J. R. (2018). Quantitative susceptibility mapping (QSM) and R2* in the human brain at 3T: Evaluation of intra-scanner repeatability. *Z Med Phys* 28, 36–48.
- Friston, K. J., Ashburner, J., Frith, C. D., Poline, J.-B., Heather, J. D. and Frackowiak, R. S. J. (1995). Spatial registration and normalization of images. *Hum Brain Mapp* 3, 165–189.
- Friston, K. J., Williams, S., Howard, R., Frackowiak, R. S. J. and Turner, R. (1996). Movement-Related effects in fMRI time-series. *Magn Reson Med* 35, 346–355.
- Gao, Y., Chen, Y., Ma, D., Jiang, Y., Herrmann, K. A., Vincent, J. A., Dell, K. M., Drumm, M. L., Brady-Kalnay, S. M., Griswold, M. A., Flask, C. A. and Lu, L. (2015). Preclinical MR fingerprinting (MRF) at 7 T: effective quantitative imaging for rodent disease models. *NMR Biomed* 28, 384–394.
- Gloor, M., Scheffler, K. and Bieri, O. (2008). Quantitative magnetization transfer imaging using balanced SSFP. *Magn Reson Med* 60, 691–700.
- Glover, G. H. (2005). Handbook of MRI pulse sequences, M. A. Bernstein, K. F. King and X. J. Zhou. Elsevier Academic Press, 2004, ISBN: 0-12-092861-2. *NMR Biomed* 18, 202–203.
- Glover, G. H. (2012). Spiral Imaging in fMRI. *Neuroimage* 62, 706–712.
- Griswold, M. A., Jakob, P. M., Heidemann, R. M., Nittka, M., Jellus, V., Wang, J., Kiefer, B. and Haase, A. (2002). Generalized autocalibrating partially parallel acquisitions (GRAPPA). *Magn Reson Med* 47, 1202–1210.
- Gudbjartsson, H. and Patz, S. (1995). The Rician Distribution of Noisy MRI Data. *Magn Reson Med* 34, 910–914.
- Haacke, E. M. (1999). *Magnetic Resonance Imaging: Physical Principles and Sequence Design*. 2 edition, Wiley.

- Haase, A., Frahm, J., Hanicke, W. and Matthaei, D. (1985). 1 H NMR chemical shift selective (CHESS) imaging. *Phys Med Biol* 30, 341.
- Hennig, J., Speck, O., Koch, M. A. and Weiller, C. (2003). Functional magnetic resonance imaging: A review of methodological aspects and clinical applications. *J Magn Reson Imaging* 18, 1–15.
- Heule, R., Pfeuffer, J. and Bieri, O. (2018). Snapshot whole-brain T1 relaxometry using steady-state prepared spiral multislice variable flip angle imaging. *Magn Reson Med* 79, 856–866.
- Holdsworth, S. J., Skare, S., Newbould, R. D., Guzman, R., Blevins, N. H. and Bammer, R. (2008). Readout-segmented EPI for rapid high resolution diffusion imaging at 3T. *Eur J Radiol* 65, 36–46.
- Hong, T., Kim, M.-O., Han, D. and Kim, D.-H. (2016). Analysis of estimation error from system imperfection in MRF. In *Proc. Intl. Soc. Mag. Reson. Med.* 24 (2016).
- Huang, Y., Sadowski, E. A., Artz, N. S., Seo, S., Djamali, A., Grist, T. M. and Fain, S. B. (2011). Measurement and comparison of T1 relaxation times in native and transplanted kidney cortex and medulla. *J Magn Reson Imaging* 33, 1241–1247.
- Jeong, H.-K., Gore, J. C. and Anderson, A. W. (2013). High-resolution human diffusion tensor imaging using 2-D navigated multishot SENSE EPI at 7 T. *Magn Reson Med* 69, 793–802.
- Jiang, Y., Ma, D., Bhat, H., Ye, H., Cauley, S. F., Wald, L. L., Setsompop, K. and Griswold, M. A. (2017a). Use of pattern recognition for unaliasing simultaneously acquired slices in simultaneous multislice MR fingerprinting. *Magn Reson Med* 78, 1870–1876.
- Jiang, Y., Ma, D., Jerecic, R., Duerk, J., Seiberlich, N., Gulani, V. and Griswold, M. A. (2017b). MR fingerprinting using the quick echo splitting NMR imaging technique. *Magn Reson Med* 77, 979–988.
- Jiang, Y., Ma, D., Seiberlich, N., Gulani, V. and Griswold, M. A. (2015). MR fingerprinting using fast imaging with steady state precession (FISP) with spiral readout. *Magn Reson Med* 74, 1621–1631.
- Johnson, G., Wadghiri, Y. Z. and Turnbull, D. H. (1999). 2D multislice and 3D MRI sequences are often equally sensitive. *Magn Reson Med* 41, 824–828.
- Jung, H., Sung, K., Nayak, K. S., Kim, E. Y. and Ye, J. C. (2009). k-t FOCUSS: A general compressed sensing framework for high resolution dynamic MRI. *Magn Reson Med* 61, 103–116.
- Kellman, P., Epstein, F. H. and McVeigh, E. R. (2001). Adaptive sensitivity encoding incorporating temporal filtering (TSENSE)[†]. *Magn Reson Med* 45, 846–852.

- Kim, D.-H., Adalsteinsson, E. and Spielman, D. M. (2004). Spiral readout gradients for the reduction of motion artifacts in chemical shift imaging. *Magn Reson Med* 51, 458–463.
- Kim, K. A., Park, M.-S., Kim, I.-S., Kiefer, B., Chung, W.-S., Kim, M.-J. and Kim, K. W. (2012). Quantitative evaluation of liver cirrhosis using T1 relaxation time with 3 tesla MRI before and after oxygen inhalation. *J Magn Reson Imaging* 36, 405–410.
- Klein, S., Staring, M. and Pluim, J. P. W. (2005). Comparison of gradient approximation techniques for optimisation of mutual information in nonrigid registration. vol. 5747, pp. 192–204, International Society for Optics and Photonics.
- Kober, T., Gruetter, R. and Krueger, G. (2012). Prospective and retrospective motion correction in diffusion magnetic resonance imaging of the human brain. *NeuroImage* 59, 389–398.
- Laule, C., Vavasour, I. M., Moore, G. R. W., Oger, J., Li, D. K. B., Paty, D. W. and MacKay, A. L. (2004). Water content and myelin water fraction in multiple sclerosis. *J Neurol* 251, 284–293.
- Lauterbur, P. C. (1973). Image Formation by Induced Local Interactions: Examples Employing Nuclear Magnetic Resonance. *Nature* 242, 190–191.
- Levitt, M. (2008). *Spin Dynamics: Basics of Nuclear Magnetic Resonance*. 2 edition, Wiley.
- Liao, C., Bilgic, B., Manhard, M. K., Zhao, B., Cao, X., Zhong, J., Wald, L. L. and Setsompop, K. (2017). 3D MR fingerprinting with accelerated stack-of-spirals and hybrid sliding-window and GRAPPA reconstruction. *NeuroImage* 162, 13–22.
- Liao, C., Cao, X., Ye, H., Chen, Y., He, H., Chen, S., Ding, Q., Liu, H. and Zhong, J. (2016). Acceleration of MR Fingerprinting with Low Rank and Sparsity Constraint. In *Proceedings of the 24th Annual Meeting ISMRM 2016* p. p. 4227,, Singapore.
- Logothetis, N. K. (2008). What we can do and what we cannot do with fMRI. *Nature* 453, 869–878.
- Ma, D., Coppo, S., Chen, Y., McGivney, D. F., Jiang, Y., Pahwa, S., Gulani, V. and Griswold, M. A. (2017). Slice profile and B1 corrections in 2D magnetic resonance fingerprinting. *Magn Reson Med* 78, 1781–1789.
- Ma, D., Gulani, V., Seiberlich, N., Liu, K., Sunshine, J. L., Duerk, J. L. and Griswold, M. A. (2013). Magnetic resonance fingerprinting. *Nature* 495, 187–192.
- Ma, D., Jiang, Y., Chen, Y., McGivney, D., Mehta, B., Gulani, V. and Griswold, M. (2018). Fast 3D magnetic resonance fingerprinting for a whole-brain coverage. *Magn Reson Med* 79, 2190–2197.

- Madore, B., Glover, G. H. and Pelc, N. J. (1999). Unaliasing by Fourier-encoding the overlaps using the temporal dimension (UNFOLD), applied to cardiac imaging and fMRI. *Magn Reson Med* *42*, 813–828.
- Maes, F., Collignon, A., Vandermeulen, D., Marchal, G. and Suetens, P. (1997). Multimodality image registration by maximization of mutual information. *IEEE Trans Med Imaging* *16*, 187–198.
- Mamisch, T. C., Hughes, T., Mosher, T. J., Mueller, C., Trattinig, S., Boesch, C. and Welsch, G. H. (2011). T2 star relaxation times for assessment of articular cartilage at 3 T: a feasibility study. *Skeletal Radiol* *41*, 287–292.
- Mansfield, P. (1977). Multi-planar image formation using NMR spin echoes. *Journal of Physics C: Solid State Physics* *10*, L55.
- Mansfield, P. and Grannell, P. K. (1975). "Diffraction" and microscopy in solids and liquids by NMR. *Phys Rev B* *12*, 3618–3634.
- McGivney, D., Pierre, E., Ma, D., Jiang, Y., Saybasili, H., Gulani, V. and Griswold, M. (2014). SVD Compression for Magnetic Resonance Fingerprinting in the Time Domain. *IEEE Trans Med Imaging* *33*, 2311–2322.
- Mehta, B. B., Ma, D., Coppo, S. and Griswold, M. A. (2017). Image Reconstruction Algorithm for Motion Insensitive Magnetic Resonance Fingerprinting (MRF). In Proceedings of the 25th Annual Meeting of the International Society for Magnetic Resonance in Medicine (ISMRM), Honolulu, Hawaii, USA, p. 0302,.
- Moeller, S., Yacoub, E., Olman, C. A., Auerbach, E., Strupp, J., Harel, N. and Uğurbil, K. (2010). Multiband multislice GE-EPI at 7 tesla, with 16-fold acceleration using partial parallel imaging with application to high spatial and temporal whole-brain fMRI. *Magn Reson Med* *63*, 1144–1153.
- Neeb, H., Zilles, K. and Shah, N. J. (2006). A new method for fast quantitative mapping of absolute water content in vivo. *NeuroImage* *31*, 1156–1168.
- Nielsen, J.-F. and Nayak, K. S. (2009). Interleaved balanced SSFP imaging: artifact reduction using gradient waveform grouping. *J Magn Reson Imaging* *29*, 745–750.
- Ojemann, J. G., Akbudak, E., Snyder, A. Z., McKinstry, R. C., Raichle, M. E. and Conturo, T. E. (1997). Anatomic Localization and Quantitative Analysis of Gradient Refocused Echo-Planar fMRI Susceptibility Artifacts. *NeuroImage* *6*, 156–167.
- Oliveira, F. P. M. and Tavares, J. M. R. S. (2014). Medical image registration: a review. *Comput Methods Biomech Biomed Engin* *17*, 73–93.
- Oliveira, F. P. M., Tavares, J. M. R. S. and Pataky, T. C. (2009). Rapid pedobarographic image registration based on contour curvature and optimization. *J Biomech* *42*, 2620–2623.

- Ordidge, R. J., Gorell, J. M., Deniau, J. C., Knight, R. A. and Helpert, J. A. (1994). Assessment of relative brain iron concentrations using T2-weighted and T2*-weighted MRI at 3 Tesla. *Magn Reson Med* 32, 335–341.
- Pierre, E. Y., Ma, D., Chen, Y., Badve, C. and Griswold, M. A. (2016). Multiscale reconstruction for MR fingerprinting. *Magn Reson Med* 75, 2481–2492.
- Posse, S., Ackley, E., Mutihac, R., Zhang, T., Hummatov, R., Akhtari, M., Chohan, M., Fisch, B. and Yonas, H. (2013). High-Speed Real-Time Resting-State fMRI Using Multi-Slab Echo-Volumar Imaging. *Frontiers in Human Neuroscience* 7.
- Poustchi-Amin, M., Mirowitz, S. A., Brown, J. J., McKinstry, R. C. and Li, T. (2001). Principles and Applications of Echo-planar Imaging: A Review for the General Radiologist. *RadioGraphics* 21, 767–779.
- Power, J. D., Mitra, A., Laumann, T. O., Snyder, A. Z., Schlaggar, B. L. and Petersen, S. E. (2014). Methods to detect, characterize, and remove motion artifact in resting state fMRI. *NeuroImage* 84.
- Preibisch, C. and Deichmann, R. (2009). Influence of RF spoiling on the stability and accuracy of T1 mapping based on spoiled FLASH with varying flip angles. *Magn Reson Med* 61, 125–135.
- Purcell, E. M., Torrey, H. C. and Pound, R. V. (1946). Resonance Absorption by Nuclear Magnetic Moments in a Solid. *Phys Rev* 69, 37–38.
- Radenkovic, D., Weingärtner, S., Ricketts, L., Moon, J. C. and Captur, G. (2017). T1 mapping in cardiac MRI. *Heart Failure Reviews* 22, 415–430.
- Rieger, B., Wenning, M., Akçakaya, M., Schad, L. R. and Weingärtner, S. (2017a). Improved motion robustness in Magnetic Resonance Fingerprinting using Intensity based Motion Correction. Cape Town, South Africa.
- Rieger, B., Zimmer, F., Zapp, J., Weingärtner, S. and Schad, L. R. (2017b). Magnetic resonance fingerprinting using echo-planar imaging: Joint quantification of T1 and T2* relaxation times. *Magn Reson Med* 78, 1724–1733.
- Ross, K. A., Williams, R. M., Schnabel, L. V., Mohammed, H. O., Potter, H. G., Bradica, G., Castiglione, E., Pownder, S. L., Satchell, P. W., Saska, R. A. and Fortier, L. A. (2013). Comparison of Three Methods to Quantify Repair Cartilage Collagen Orientation. *Cartilage* 4, 111–120.
- Roujol, S., Foppa, M., Weingärtner, S., Manning, W. J. and Nezafat, R. (2015). Adaptive registration of varying contrast-weighted images for improved tissue characterization (ARCTIC): application to T1 mapping. *Magn Reson Med* 73, 1469–1482.
- Sadowski, E. A., Djamali, A., Wentland, A. L., Muehrer, R., Becker, B. N., Grist, T. M. and Fain, S. B. (2010). BOLD and Perfusion MRI: Detecting Differences in Oxygen Bioavailability and Blood Flow in Transplanted Kidneys. *Magn Reson Imaging* 28, 56–64.

- Sarracanie, M., Cohen, O. and Rosen, M. S. (2015). 3D Balanced-EPI Magnetic Resonance Fingerprinting at 6.5 mT. In ISMRM 23rd Annual Meeting, Toronto, Canada.
- Schmithorst, V. J., Dardzinski, B. J. and Holland, S. K. (2001). Simultaneous correction of ghost and geometric distortion artifacts in EPI using a multi-echo reference scan. *IEEE Trans Med Imaging* 20, 535–539.
- Schwefel, H.-P. P. (1993). *Evolution and Optimum Seeking: The Sixth Generation*. John Wiley & Sons, Inc., New York, NY, USA.
- Setsompop, K., Cohen-Adad, J., Gagoski, B. A., Raji, T., Yendiki, A., Keil, B., Wedeen, V. J. and Wald, L. L. (2012). Improving diffusion MRI using simultaneous multi-slice echo planar imaging. *NeuroImage* 63, 569–580.
- Styner, M., Brechbuhler, C., Szckely, G. and Gerig, G. (2000). Parametric estimate of intensity inhomogeneities applied to MRI. *IEEE Trans Med Imaging* 19, 153–165.
- Sumpf, T. J., Petrovic, A., Uecker, M., Knoll, F. and Frahm, J. (2014). Fast T2 Mapping With Improved Accuracy Using Undersampled Spin-Echo MRI and Model-Based Reconstructions With a Generating Function. *IEEE Trans Med Imaging* 33, 2213–2222.
- Tofts, P. (2005). *Quantitative MRI of the Brain: Measuring Changes Caused by Disease*. John Wiley & Sons.
- Tsao, J. (2010). Ultrafast imaging: Principles, pitfalls, solutions, and applications. *J Magn Reson Imaging* 32, 252–266.
- Tyler, D. J., Moore, R. J., Marciani, L. and Gowland, P. A. (2004). Rapid and accurate measurement of transverse relaxation times using a single shot multi-echo echo-planar imaging sequence. *Magn Reson Imaging* 22, 1031–1037.
- Volz, S., Nöth, U. and Deichmann, R. (2012). Correction of systematic errors in quantitative proton density mapping. *Magn Reson Med* 68, 74–85.
- Vymazal, J., Righini, A., Brooks, R. A., Canesi, M., Mariani, C., Leonardi, M. and Pezzoli, G. (1999). T1 and T2 in the Brain of Healthy Subjects, Patients with Parkinson Disease, and Patients with Multiple System Atrophy: Relation to Iron Content. *Radiology* 211, 489–495.
- Walsh, D. O., Gmitro, A. F. and Marcellin, M. W. (2000). Adaptive reconstruction of phased array MR imagery. *Magn Reson Med* 43, 682–690.
- Wang, D., Strugnell, W., Cowin, G., Doddrell, D. M. and Slaughter, R. (2004). Geometric distortion in clinical MRI systems: Part I: evaluation using a 3D phantom. *Magn Reson Imaging* 22, 1211–1221.
- Wang, Z., Li, H., Zhang, Q., Yuan, J. and Wang, X. (2016). Magnetic Resonance Fingerprinting with compressed sensing and distance metric learning. *Neurocomputing* 174, Part B, 560–570.

- Wansapura, J. P., Holland, S. K., Dunn, R. S. and Ball, W. S. (1999). NMR relaxation times in the human brain at 3.0 tesla. *J Magn Reson Imaging* 9, 531–538.
- Wartjes, J., Dahlqvist, O. and Lundberg, P. (2007a). Novel method for rapid, simultaneous T1, T*2, and proton density quantification. *Magn Reson Med* 57, 528–537.
- Wartjes, J., Dahlqvist, O. and Lundberg, P. (2007b). Novel method for rapid, simultaneous T1, T*2, and proton density quantification. *Magn Reson Med* 57, 528–537.
- Wartjes, J., Leinhard, O. D., West, J. and Lundberg, P. (2008). Rapid magnetic resonance quantification on the brain: Optimization for clinical usage. *Magn Reson Med* 60, 320–329.
- Weingärtner, S., Moeller, S., Schmitter, S., Auerbach, E., Kellman, P., Shenoy, C. and Akçakaya, M. (2017). Simultaneous multislice imaging for native myocardial T1 mapping: Improved spatial coverage in a single breath-hold. *Magn Reson Med* 78, 462–471.
- Weingärtner, S., Roujol, S., Akçakaya, M., Basha, T. A. and Nezafat, R. (2015). Free-breathing multislice native myocardial T1 mapping using the slice-interleaved T1 (STONE) sequence. *Magn Reson Med* 74, 115–124.
- Weiskopf, N., Lutti, A., Helms, G., Novak, M., Ashburner, J. and Hutton, C. (2011). Unified segmentation based correction of R1 brain maps for RF transmit field inhomogeneities (UNICORT). *NeuroImage* 54, 2116–2124.
- Woo, J., Stone, M. and Prince, J. L. (2015). Multimodal Registration via Mutual Information Incorporating Geometric and Spatial Context. *IEEE Trans Image Process* 24, 757–769.
- Wright, K. L., Jiang, Y., Ma, D., Noll, D. C., Griswold, M. A., Gulani, V. and Hernandez-Garcia, L. (2018). Estimation of perfusion properties with MR Fingerprinting Arterial Spin Labeling. *Magn Reson Imaging* 50, 68–77.
- Xu, Z., Lyu, M., Hui, S. K., Mei, Y., Chen, Z., Chen, W., Wu, E. X. and Feng, Y. (2017). Motion correction for Magnetic Resonance Fingerprinting by using Sliding-Window Reconstruction and Image Registration. In Proceedings of the 25th Annual Meeting of the International Society for Magnetic Resonance in Medicine (ISMRM), Honolulu, Hawaii, USA, p. 1273,.
- Xue, H., Shah, S., Greiser, A., Guetter, C., Littmann, A., Jolly, M.-P., Arai, A. E., Zuehlsdorff, S., Guehring, J. and Kellman, P. (2012). Motion correction for myocardial T1 mapping using image registration with synthetic image estimation. *Magn Reson Med* 67, 1644–1655.
- Yablonskiy, D. A. and Haacke, E. M. (1994). Theory of NMR signal behavior in magnetically inhomogeneous tissues: The static dephasing regime. *Magn Reson Med* 32, 749–763.

- Yang, M., Ma, D., Jiang, Y., Hamilton, J., Seiberlich, N., Griswold, M. A. and McGivney, D. (2018). Low rank approximation methods for MR fingerprinting with large scale dictionaries. *Magn Reson Med* 79, 2392–2400.
- Ye, H., Cauley, S. F., Gagoski, B., Bilgic, B., Ma, D., Jiang, Y., Du, Y. P., Griswold, M. A., Wald, L. L. and Setsompop, K. (2017). Simultaneous multislice magnetic resonance fingerprinting (SMS-MRF) with direct-spiral slice-GRAPPA (ds-SG) reconstruction. *Magn Reson Med* 77, 1966–1974.
- Ye, H., Ma, D., Jiang, Y., Cauley, S. F., Du, Y., Wald, L. L., Griswold, M. A. and Setsompop, K. (2015). Accelerating magnetic resonance fingerprinting (MRF) using t-blipped simultaneous multislice (SMS) acquisition. *Magn Reson Med* 75, 2078–85.
- Zapp, J., Domsch, S., Weingärtner, S. and Schad, L. R. (2017). Gaussian signal relaxation around spin echoes: Implications for precise reversible transverse relaxation quantification of pulmonary tissue at 1.5 and 3 Tesla. *Magn Reson Med* 77, 1938–1945.
- Zhao, B., Setsompop, K., Adalsteinsson, E., Gagoski, B., Ye, H., Ma, D., Jiang, Y., Ellen Grant, P., Griswold, M. A. and Wald, L. L. (2018). Improved magnetic resonance fingerprinting reconstruction with low-rank and subspace modeling. *Magn Reson Med* 79, 933–942.
- Zhao, B., Setsompop, K., Ye, H., Cauley, S. F. and Wald, L. L. (2016). Maximum Likelihood Reconstruction for Magnetic Resonance Fingerprinting. *IEEE Trans Med Imaging* 35, 1812–1823.
- Zhu, D. C. and Penn, R. D. (2005). Full-brain T1 mapping through inversion recovery fast spin echo imaging with time-efficient slice ordering. *Magn Reson Med* 54, 725–731.

Curriculum Vitae

Benedikt Rieger

Address Kleinfeldstr. 19
68165 Mannheim
Date of Birth 29.12.1987
Place of birth Heppenheim, Germany

Education

- Since 2015 **Ruprecht-Karls-Universität Heidelberg**, Germany
Doktorand Computer Assisted Clinical Medicine
Topic: Tissue quantification based on Magnetic Resonance
Fingerprinting
Supervisor: Prof. Dr. rer. nat. Lothar R. Schad
- 2010 - 2012 **Technical University of Munich**, Germany
MSc electrical engineering, GPA: 1.6 (1=best, 6=lowest)
Masters Thesis: Design and test of a tumor implant for
in-vivo experiments
- 2007 - 2010 **DHBW Mannheim**, Germany
B.Eng in electrical engineering GPA: 1.5 (1=best, 6=lowest)
- 2009 - 2010 **University of Tennessee**, Knoxville, USA
Term abroad, GPA: 4.0 (4.0 = highest)
- 2005 - 2007 **Friedrich-Dessauer-Gymnasium**, Aschaffenburg, Germany
A-Levels, GPA: 2.2 (1 = best, 6 = lowest)

Additional work experience

- 2013 - 2015 **EY-Parthenon**, Hamburg, Germany
Management consultant

- 2012 **A. T. Kearney**, Munich, Germany
Summer intern management consultant
- 2007 - 2010 **Siemens Healthineers**, Mannheim, Germany
Customer Service Engineer

Scholarships and awards

- 2011 Siemens Masters scholarship
Awarded each year to 40 students in Germany
- 2010 Prize for the best bachelor thesis of the DHBW Mannheim
awarded to 1 person out of 1500 graduates from the university
- 2008 Studienstiftung des deutschen Volkes scholarship
granted to 0.5 % of all German students

Acknowledgements

I'd like to thank all my colleges, friends and family, who have supported me throughout the last three years of my PhD and who have accompanied me in this exciting phase of my life. My special thanks goes to:

Prof. Dr. Lothar Schad, who gave me the opportunity to do my doctorate at his chair and always fully supported me in every aspect.

Dr. Sebastian Weingärtner for his amazing support, constant ideas and teaching me how to become a researcher in a fun and entertaining manner. Additionally to being a great supervisor, I want to thank him for all the memorable evenings at various locations, including in Mannheim, Paris or Hawaii.

Dr. Jascha Zapp for supporting me whenever I was lost and needed help, whether it was writing a paper, pulse programming, or motivating me when things didn't work out the way they should.

Prof. Dr. Mehmet Akçakaya for inviting me to his chair in Minnesota, giving me the possibility to try out new ideas in a great surrounding while enjoying the freezing weather in Minneapolis during winter.

Dr. Jorge Chacon-Caldera for entertaining discussions, fun evening and always welcoming a Feierabendbier, no matter what time it was.

The whole CKM team for a great work atmosphere and all the fun activities and sport events we had together. Especially I want to thank Prof. Dr. Frank Zöllner and all the PhD students for the countless hours of tabletop football.

The complete IDIBAPS team from Barcelona for welcoming me for 6 months at their institute and integrating me in the Catalan society.

Last but not least, my biggest thanks go to my family and fiancée, who supported and helped me throughout my complete course of study!